

**Dimensional Metrology and Thermo-Fluid Studies on Additively Manufactured
Transpiration Cooling Structures**

by

Zheng Min

Bachelor of Engineering, Central South University, China, 2011

Master of Science in Mechanical Engineering, University of Pittsburgh, US, 2015

Submitted to the Graduate Faculty of the
Swanson School of Engineering in partial fulfillment
of the requirements for the degree of
Doctor of Philosophy

University of Pittsburgh

2021

UNIVERSITY OF PITTSBURGH

SWANSON SCHOOL OF ENGINEERING

This dissertation was presented

by

Zheng Min

It was defended on

March 29, 2021

and approved by

Dr. Qing-Ming Wang, PhD, Professor, Department of Mechanical Engineering and Materials Science

Dr. Albert To, PhD, Professor, Department of Mechanical Engineering and Materials Science

Dr. Bruce Kang, PhD, Professor, Department of Mechanical and Aerospace Engineering, West Virginia University

Dissertation Director: Dr. Minking K Chyu, PhD, Professor, Department of Mechanical Engineering and Materials Science

Copyright © by Zheng Min

2021

Dimensional Metrology and Thermo-Fluid Investigation on Additively Manufactured Transpiration Cooling Structures

Zheng Min, PhD

University of Pittsburgh, 2021

The rapid advancement in metallic additive manufacturing (AM) has provided us with new opportunities and challenges to apply more sophisticated cooling designs to protect high-temperature components in gas turbines. With the benefits of high design freedom and structural complexity, the direct metal laser sintering (DMLS) AM technique can fabricate cooling passages into microscale in a highly compact fashion, making transpiration cooling feasible in turbine airfoil to protect hot surfaces. In this research, an accurate dimensional characterization technique of microscale cooling passages was developed, and the related thermo-fluid performance was studied.

The DMLS process produces microchannels with deformations and surface roughness, which significantly impact thermo-fluid performance. The state-of-the-art micro-CT scanners hardly work for intricate AM transpiration cooling structures due mainly to limitations in penetration rate and detection precision on heavy metals. In this research, a high-precision scanning electron microscope (SEM) characterization combined with a multi-level image segmentation method was employed to statistically analyze the geometric dimensions of microchannels made by AM. Based on the characterization results, surface improvement techniques were used to generate expected channel sizes, preparing for the cooling effectiveness studies with various geometric parameters.

Most previous experimental studies on transpiration cooling focused only on cooling effectiveness, leaving a significant vacancy in the literature on the heat transfer coefficient (HTC)

at the target surfaces. Two classic methods to investigate HTC, the steady-state foil heater method and the transient thermography technique, both fail for transpiration cooling. That is because the foil heater would block numerous coolant outlets, and the transient semi-infinite solid medium theory no longer holds for porous plates. In this study, a micro-lithography technique was employed to precisely coat a patterned surface heater directly on top of the low thermally conductive test plate to determine the HTC distributions.

The dimensional variations created by AM fabrication generate inhomogeneity of cooling performance at the target surface. Moreover, the various hole size would cause clogging issues of the smallest channels during operation, which would, in turn, affect the cooling performance as well. A machine learning model was developed in this work to predict cooling effectiveness distributions from these contributing factors.

Table of Contents

Acknowledgements	xvi
1.0 Introduction.....	1
1.1 Background and Research Objectives.....	1
1.1.1 Introduction to Turbine Blade Cooling	1
1.1.2 Manufacturing and Metrology Challenges.....	3
1.1.3 Heat Transfer in Transpiration Cooling.....	9
1.1.4 Thermal Performance Predictions from Geometric Dimensions	13
1.2 Literature Review	15
1.2.1 AM Capabilities for Metallic Porous Media Fabrication.....	15
1.2.2 Dimensional Metrology for AM Parts.....	17
1.2.3 Cooling Effectiveness Studies on Transpiration Cooling	20
1.2.4 Heat Transfer Coefficient Studies on Film Cooling.....	22
1.2.5 Theoretical Modeling to Predict Cooling Performance.....	25
1.3 Present Work Statement.....	31
1.3.1 Dimensional Characterization and Surface Improvement of Straight-Hole Test Samples	31
1.3.2 Transpiration Cooling Effectiveness Investigations	32
1.3.3 Heat Transfer Coefficient Investigations	33
1.3.4 Machine Learning Modeling to Predict Cooling Performance.....	34
2.0 Dimensional Characterization of AM Microchannels.....	35
2.1 Methodology.....	35

2.1.1 Specimen Designs and Fabrication.....	35
2.1.2 SEM Characterization	38
2.1.3 Image Segmentation and Data Analysis.....	39
2.1.4 Uncertainty Analysis.....	45
2.2 Results and Discussions.....	47
3.0 Surface Improvement of AM Microchannels.....	53
3.1 CAD-Based Compensation for Sample Redesign	53
3.1.1 Methodology	53
3.1.2 CAD-Based Compensation Results	55
3.2 Electrochemical Polishing Process	58
3.2.1 Methodology	58
3.2.2 Surface Improvement Results.....	61
4.0 Transpiration Cooling Effectiveness Investigations	65
4.1 Cooling Performance of AM-Made Transpiration and Film Cooling.....	65
4.1.1 Methodology	65
4.1.2 Experimental Facilities	70
4.1.3 IR Camera Calibration.....	71
4.1.4 Uncertainty Analysis.....	73
4.1.5 Results and Discussions	74
4.2 Effect of Geometric Parameters on the Cooling Performance for Straight-Hole Transpiration Cooling Configurations	80
4.2.1 Methodology	80
4.2.2 Results and Discussions	84

5.0 Heat Transfer Coefficient Investigations.....	89
5.1 Micro-Lithography Method for Surface Heater Fabrication	90
5.1.1 SLA Printing of Transpiration Cooling Samples.....	90
5.1.2 Surface Heater Design	91
5.1.3 Surface Heater Fabrication.....	95
5.2 Heat Transfer Test	99
5.2.1 Methodology, Test Facility, and Procedure.....	99
5.2.2 FEM Post-Processing Method.....	102
5.2.3 Results and Discussion.....	107
6.0 Machine Learning Modeling for Cooling Effectiveness Prediction	117
6.1 Modeling Development	118
6.1.1 Geometry Design	118
6.1.2 CFD Simulation Setup	121
6.1.3 Modeling Architecture Design	126
6.1.4 Model Training.....	128
6.2 Modeling Validation and Discussion	130
7.0 Conclusions and Future Work.....	137
7.1 Major Accomplishments	137
7.2 Future Work	140
Bibliography	142

List of Tables

Table 2.1. Inconel 718 parts build parameters.....	36
Table 3.1 Redesigned channel sizes.....	54
Table 4.1 Comparison of objective channel sizes and as-produced channel sizes	83
Table 4.2 Porosity and compactness comparison of various hole configurations.....	88
Table 5.1 Wire width designs of the surface heaters with different hole configurations	95
Table 5.2 Electrical resistance of the surface heaters	99

List of Figures

Figure 1.1 Schematic of film cooling and transpiration cooling.....	3
Figure 1.2 Hatch overlaps and particle attachments.....	5
Figure 1.3 Morphology differences between microchannels with different hole pitches, (a) Hole spacing of 2D with more particle attachments on the edges; (b) Hole spacing of 3D with smoother hole profiles	7
Figure 1.4 Brightened edge effect of SEM photograph.....	8
Figure 1.5 Comparison between a flat surface heat transfer and a surface covered by coolant film.....	10
Figure 1.6 Schematic of the transient heat transfer test.....	11
Figure 1.7 Schematic of the steady-state heat transfer test for film-covered surface.....	13
Figure 1.8 Overview of the task of the dimensional characterization and surface improvement.....	32
Figure 1.9 Geometric designs for transpiration cooling and film cooling structures.....	33
Figure 1.10 The impact of the channel size variations on the cooling performance: (a) SEM photo of various channel sizes; (b) Possible blockage caused by the AM fabrication; (c) Cooling efficiency reduction by the clogging issues	34
Figure 2.1 Sample dimensional designs and specimen printing, (a) Dimensional design of specimens; (b) Inconel 718 powder for additive manufacturing; (c) Three channel spacing designs; (d) Schematic of DMLS process; (e) As-printed test specimens with radius of 200μm and different hole pitches.	37

Figure 2.2 Sample slicing for SEM characterizations. (a) cutting positions of the specimen, (b) micrographs of the four cutting surfaces	38
Figure 2.3 Representative SEM graphs for cross-sectional views of microchannels.....	39
Figure 2.4 Image segmentation process, (a) SEM micrograph for microchannels; (b) Image grayscale histogram and two dividing threshold values T_1 and T_2; (c) Identified hole areas using white dots.....	42
Figure 2.5 Two examples of the profile extraction for two channels with identical designed sizes.....	43
Figure 2.6 Combined profiles of 280 hole profiles	44
Figure 2.7 Circularity tolerance definitions: (a) the common definition of circularity tolerance, (b) an extreme example of the solid part approaching the centroid, (c) circularity tolerance definition in this study.	45
Figure 2.8 Uncertain area (red area) analysis of the image segmentation technique.....	47
Figure 2.9 Comparison of the mean radius of different hole configurations	48
Figure 2.10 Comparison of arithmetical mean deviations of different hole configurations	50
Figure 2.11 Combined profiles of the specimens from the originally designed group	51
Figure 2.12 Quantitive results of dimensional metrology: (a) the ratio of the as-printed radius and the objective radius R_p/R_o, (b) arithmetical mean deviation of all data points Ra, (c) the circularity tolerance C.	52
Figure 3.1 CAD-based compensation: (a) correlation between as-produced channel size and designed values and (b) comparison of originally designed sample and redesigned sample.....	54

Figure 3.2 Micrograph comparison between (a) the originally designed group, (b) the redesigned group.....	56
Figure 3.3 Combined profiles comparison.....	57
Figure 3.4 Quantitative results of dimensional metrology of both two groups. (a) the ratio of the as-printed radius and the objective radius R_p/R_o , (b) the arithmetical mean deviation of all data points Ra , (c) the circularity tolerance C	58
Figure 3.5 ECP test setup and the sample before and after ECP process	61
Figure 3.6 SEM photos of two surfaces before and after ECP process	62
Figure 3.7 Comparison of the originally designed sample, redesigned sample and the sample after ECP. (a) comparison of combined profiles, (b) comparison of three geometric parameters.	64
Figure 4.1 Schematics of five transpiration structures and one film cooling design	66
Figure 4.2 Dimensions and SEM micrographs of the transpiration cooling structures: (a) Round Holes with Pitch of 3D; (b) Round Holes with Pitch of 2D; (c) Spheres Packing Design; (d) Wire Mesh Design; (e) Blood Vessel Design	67
Figure 4.3 Effective coolant covered area.....	68
Figure 4.4 Transpiration Cooling Effectiveness Curve Fitting	69
Figure 4.5 The schematic and photograph of the test rig and the test conditions	71
Figure 4.6 IR calibration: (a) Calibration test setup; (b) The calibration curve of one sample	73
Figure 4.7 Transpiration cooling effectiveness comparison.....	75
Figure 4.8 The area-averaged transpiration cooling effectiveness comparison.....	76

Figure 4.9 Effect of porosity and internal surface area on the transpiration cooling effectiveness	77
Figure 4.10 Spanwise averaged, streamwise distributed transpiration cooling effectiveness	79
Figure 4.11 The illustrative drawing of a cross-sectional unit cell.....	82
Figure 4.12 SEM photos at the outlet surfaces of the as-printed samples after CAD compensation.....	83
Figure 4.13 Black painted test specimens for the heat transfer test.....	84
Figure 4.14 Transpiration cooling effectiveness distributions of various hole configurations	85
Figure 4.15 Area-averaged transpiration cooling effectiveness comparison.....	87
Figure 4.16 Plot of the transpiration cooling effectiveness vs. compactness	88
Figure 5.1 SLA printed transpiration cooling samples	91
Figure 5.2 Surface heater design: (a) A schematic view; (b) The top view photo of the surface heater.....	92
Figure 5.3 An example of the commercial heater design [135].....	93
Figure 5.4 The tentative surface heater design: (a) circuit pattern design; (b) the equivalent circuit diagram; (c) Top view photo of the heater; (d) the non-uniform temperature distribution during heating	93
Figure 5.5 The circuit design in a unit cell: (a) Four evenly divided solid zones in a unit cell; (b) Silver wiring pattern design in a unit cell; (c) The equivalent circuit diagram ..	94

Figure 5.6 Illustrative figures of surface heater fabrication: (a) a schematic view and the photo of one coated example; (b) photo of two shadow mask; (c) SEM photos of the mask pattern and the combined effect of the designed pattern.....	96
Figure 5.7 Circuit designs and the as-produced surface heaters.....	98
Figure 5.8 The static hating test setup and two example specimens after black painting ...	98
Figure 5.9 Test setup for HTC investigations.....	101
Figure 5.10 Steady-state heat transfer test: (a) Adiabatic cooling effectiveness test; (b) HTC test with coolant injection; (c) HTC test without coolant injection.....	101
Figure 5.11 Meshing for FEA model and boundary conditions	104
Figure 5.12 Flowchart of the post-processing to correct h_f and η	104
Figure 5.13 Comparison between experimental results with and without heat loss correction: (a) h_f map and spanwise averaged values; (b) η map and spanwise averaged values	105
Figure 5.14 Adiabatic cooling effectiveness distributions	107
Figure 5.15 Cooling holes distribution in the same interested area	109
Figure 5.16 Spanwise averaged adiabatic cooling effectiveness comparison of different channel size	110
Figure 5.17 Spanwise averaged adiabatic cooling effectiveness comparison of different channel spacing	111
Figure 5.18 Spanwise averaged heat transfer coefficient of different channel size	112
Figure 5.19 Spanwise averaged heat transfer coefficient of different channel spacing.....	113
Figure 5.20 Heat transfer coefficient comparison with literature data	115
Figure 5.21 Adiabatic cooling effectiveness comparison with literature data	116

Figure 6.1	The overlapped hole profiles and corresponding radius distribution: (a) the combined hole profiles with a designed channel diameter of 0.3mm and a pitch-to-diameter value of 3; (b) the Weibull distribution curve fitting of the channel size	119
Figure 6.2	Geometric design for different hole size distributions (cases)	120
Figure 6.3	Geometric design for different blockage ratios in one case	120
Figure 6.4	Mesh and boundary conditions: (a) Mesh overview; (b) Local views of mesh	122
Figure 6.5	Overall cooling effectiveness comparison between experimental result and CFD simulation	124
Figure 6.6	Seven sub-cases with different blockage ratios in one case	125
Figure 6.7	The architecture of the overall cooling effectiveness prediction model	128
Figure 6.8	Model performance in the training set	131
Figure 6.9	Model predictions trained from different quantities of the training cases	132
Figure 6.10	Lateral averaged cooling effectiveness comparison	134
Figure 6.11	Averaged prediction accuracy for subcases with different blockage ratios	135
Figure 6.12	Pixel-wised predictions in the validation group of the two machine learning models: (a) Yang’s model; (b) The model developed in this study	136

Acknowledgements

First and foremost, I would like to express my deep and sincere gratitude to my advisor, Dr. Minking Chyu, for his invaluable encouragement, continuous support, and patient guidance during this dissertation work. Our conversations have been, and always will be, of great value to me.

I also thank Dr. Qing-Ming Wang, Dr. Albert To, and Dr. Bruce Kang for being my committee members. Thank you all for bringing a depth of knowledge to this work. Without your advice, encouragement, and help, I would not accomplish this dissertation work.

I am extremely grateful to my previous colleague, Dr. Li Yang, for his help and inspiration. I have learned a lot from our friendly discussions, chats, and meetings.

Many thanks to my colleagues in our heat transfer group, Sarwesh Parbat, Gan Huang, Jin Xu, and Yi Ye, for their support and help in all aspects.

Special thanks to all the professors who have taught courses for me. The knowledge I have learned laid the solid foundation for this work.

Last, I would like to thank my wife for her unconditional support and love. I am grateful for her courage to marry me and her patience for not divorcing me.

1.0 Introduction

1.1 Background and Research Objectives

1.1.1 Introduction to Turbine Blade Cooling

The last 70 years have witnessed significant advancement in cooling technologies for gas turbine airfoils. The more advanced cooling schemes allow the blades to pursue higher working temperatures far above the material temperature limits, achieving higher overall turbine efficiency. In a turbine blade, the coolant (bleed air drawn from the compressor) is directed into designated cooling passages, cooling the internal wall convectively before being ejected through discrete holes or slots. Such coolant ejection results in a layer of coolant film to protect the outer surface from hot combustion gases. Based on the cooling/protection locations, the cooling designs in turbine blades are classified into two categories: internal cooling and external cooling. The internal cooling design has evolved from simple serpentine passages to channels with complex geometries (double-wall structure, pin-fin bank, turbulators, lattices, etc.) over the years [1]. The more sophisticated internal cooling design aims to increase coolant turbulence intensity as well as the extended surface area to promote heat removal from the wall [2, 3]. With the development of the materials and manufacturing, the cooling channels can be fabricated closely adjacent to the outer surface to achieve the concept of “skin-cooled” airfoil [2, 4, 5]. The small distance to hot gas makes the heat spread into coolant more effectively.

In addition to internal cooling, external cooling is also an important component of the overall cooling to the turbine airfoils, especially for the leading edge's high thermal load area. As the major external cooling technique, film cooling discharges the coolant into the boundary layer along the external surface subjected to hot mainstream via small holes or slots. The ejected coolant mixes with the hot gas flow, establishing a new boundary layer downstream of the ejection position. Since the coolant temperature is lower than the hot gas, the mixture temperature in the new boundary layer is reduced. With this cooler mixture “blanket” covering the hot surface, the heat flux to the wall can be reduced by the lower driving temperature potential between the boundary layer and wall temperature [6]. Extensive efforts have been put into film cooling studies to enhance the cooling efficiency. The most significant design change has been the hole shape transition from round channel to shaped film hole, which is made of round throat section and symmetric expanded ejection region [7]. To date, the state-of-the-art film cooling utilizes fan-shaped holes with diameters larger than 1mm, providing an averaged adiabatic cooling efficiency of 0.3 to 0.5 [8, 9]. Although substantial improvements have been made in these studies on film cooling efficiency, the inherent nature of the discrete hole positions causes non-uniform surface temperatures that may reduce the service lifespan of a turbine blade. Also, both film lift-off near the ejection hole and the film decay downstream may weaken film cooling protections.

As an external cooling alternative to film cooling, transpiration cooling utilizes much denser microscale cooling passages instead of discrete film cooling holes for coolant injection as shown in Fig. 1.1. Because of these large number of cooling passages, which are closely adjacent, the solid-fluid contacting surfaces in a given metal substrate volume are much larger than film cooling holes. This could render profound effects on the heat transfer characteristics in the metal substrate beneath its outer surface that is exposed directly to the hot gas stream. One plausible

phenomenon is that heat may transfer among adjacent transpiration coolant passages through the solid walls. These through-wall channels would offer an additional conduit to dispose the heat to the internal cooling sink eventually, hence the substrate temperature may be reduced. Also, the coolant coming out from the porous media continuously renews or resupplies to the thin film, covering the hot surface more uniformly than film cooling. Therefore, the transpiration cooling scheme, acting as a combination of “skin-cooled” internal cooling and more uniform external film cooling, theoretically can render a better cooling performance than conventional cooling technologies.

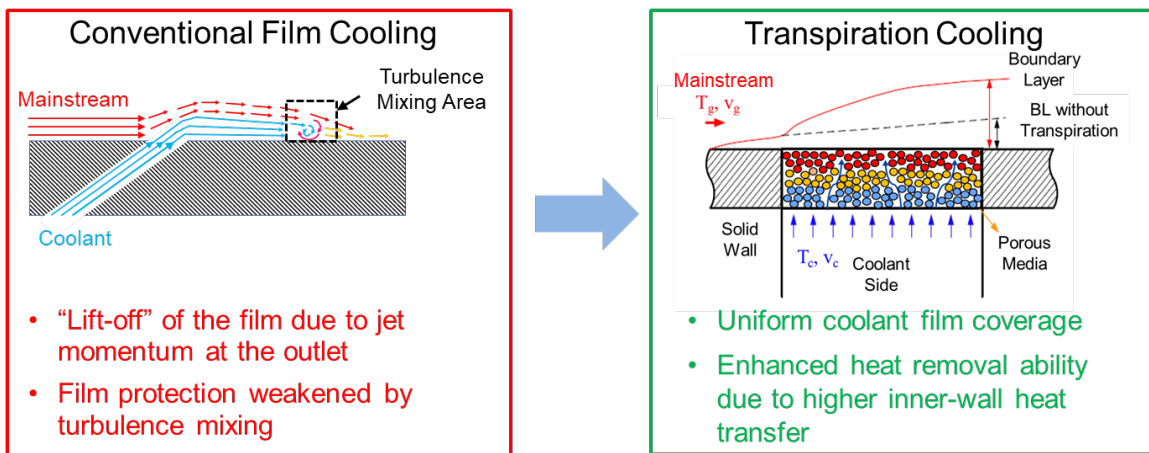


Figure 1.1 Schematic of film cooling and transpiration cooling

1.1.2 Manufacturing and Metrology Challenges

Although transpiration cooling has been proven successful in many applications, such as rocket nozzles and combustor liners, its application to gas turbines has been very limited, due mainly to manufacturing difficulties of micro-scale structures and concerns on mechanical strength. The most commonly used manufacturing technique for transpiration cooling structures, the sintered powder pack, hardly produces a porous metallic wall with satisfactory mechanical

strength, passage design flexibility, and cost efficiency for airfoil simultaneously. Therefore, searching for an innovative way to fabricate such transpiration cooling structures for turbine airfoil remains as both an opportunity and a challenge at the same time. In recent years, the rapid development of metallic additive manufacturing has provided a new perspective to fabricate such intricate structures. With the advancement of powder-bed-based direct metal laser sintering (DMLS) additive manufacturing, the complex geometries in small scale such as microchannels and cellular lattice could be precisely fabricated with comparable mechanical strength as their casting counterparts, providing a new path beyond traditional subtractive manufacturing to fabricate transpiration cooling structures. In this study, the advanced DMLS technique was employed to fabricate transpiration cooling structures using IN 718 superalloy powder.

As a laser sintering process, the DMLS method generates parts with rough surfaces due to laser hatch overlaps and particle attachments, leading to dimensional deformations and surface roughness over the final product. For microchannels made by AM, the hatch overlaps and the particle attachments (Fig. 1.2) are affected not only by the nature of DMLS but also possibly by channel configurations, such as the designed channel size and the hole pitch (i.e., the distance between adjacent channels). As a result, the microchannels made by DMLS method is not as smooth as those made by laser cut or drilling. In the transpiration cooling passages, the rough surface characteristics of the inner walls have a significant impact on thermo-fluid performance. Not only does the rough inner surface augment the convective heat transfer inside the channel, but the surface also generates stronger vortices that would interact with the external film at the channel outlet. Hence the cooling efficiency is significantly influenced by the inner surface qualities of microchannels.

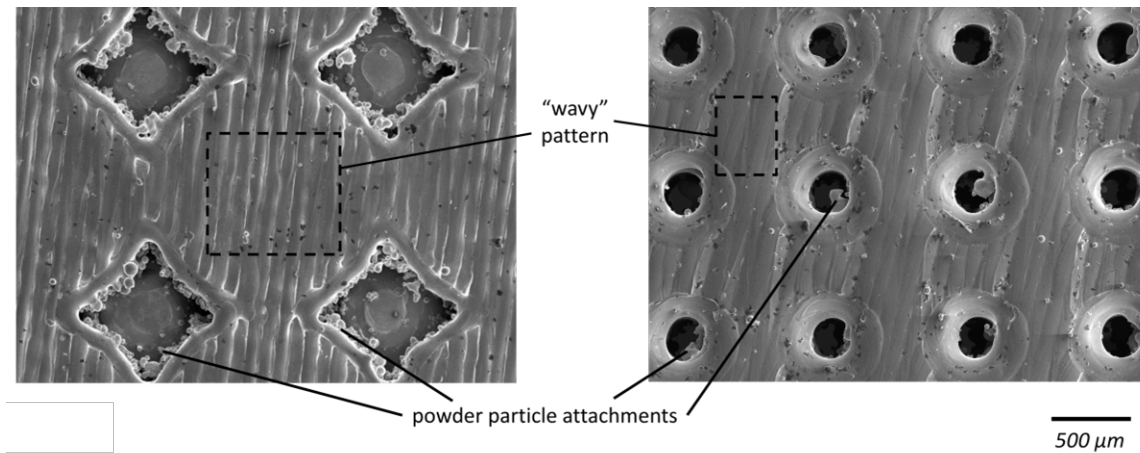


Figure 1.2 Hatch overlaps and particle attachments

Because the surface characteristics of the microchannels made by AM play such an important role in transpiration cooling, one of the main goals of this research is to characterize the printing qualities of the channels accurately. To implement an accurate and precise dimensional metrology of the complex geometries made by AM is challenging. In microchannels, the small channel size and irregular particle attachments make the surface profile measurements difficult for conventional characterization methods, such as contact stylus profilometry, scanning probe microscopy, and interferometric microscopy. In recent years, microfocus X-ray computed tomography (micro CT) has emerged as one of the most popular techniques to tackle this challenge. Using a large number of 2D images, the micro-CT scan could reconstruct the continuous 3D model of the workpiece. Nevertheless, several inherent limitations of this technique, such as wall thickness restrictions, elemental diffractions of X-ray, and reconstruction inaccuracies, impede the applications of CT scans for multi-row microchannel characterizations.

Compared to CT scan, another surface characterization tool, scanning electron microscope, show advantages in three aspects. First, the resolution is much higher than the micro-CT technique at a much lower cost. With the accelerating energy of prime electron beam higher than 10keV,

theoretically, features less than 0.1 nm can be captured in SEM micrographs [10], which is sufficient for most of the surface feature/roughness measurements. Second, the characterization accuracy of surface features for SEM image is not limited by the attenuation coefficient of the material; thus, there are no size/thickness limits or composition restrictions for any metallic coupons. For AM microchannel parts, the dimensional metrology by micro-CT scan is restricted to coupons with a single or single row of microchannels inside a thin wall. However, the inner surface characteristics of the packed multi-microchannels are different. As shown in Fig. 1.3, smaller pitch values (i.e., the distance between adjacent channels) lead to rougher surface characteristics, which significantly affects the thermo-fluid performance for AM products. Therefore, pitch values should be taken into account, and using SEM characterization as an alternative becomes one of the motivations of this work. The third advantage of SEM technique is the well-known “edge effect”, which is caused by a large number of secondary electrons escaping from both the top and the vertical surfaces at the edge and hence increasing the edge brightness [10, 11]. The increased contrast between the hole area and the solid part enhances the capability to visualize the presence of the edge in further image segmentation analysis. Fig. 1.4 shows an SEM image for the cross-sectional view of microchannels, demonstrating such edge effect on the channel profiles. While the CT-scan 2D images generate blurry profiles at the feature edges, the SEM picture provides a better edge identification, allowing computationally “cheaper” algorithms in the image segmentation process. Although SEM demonstrates a lot of advantages above, two main drawbacks of SEM characterization also need to be taken into consideration for geometric metrology. As a surface characterization technique, it is difficult to get a large number of 2D images for continuous 3D model reconstructions compared to CT scan. Thus, this method can only provide information for a finite number of cross-sections at several critical surfaces. The second

issue associated with the SEM technique is that it is a destructive method for the sample when characterizing internal surfaces since the sample has to be sliced into different parts for internal feature characterization. The printing qualities of a real part has to be verified by the “witness” AM part, which is the duplication of the interested component made by the identical printing parameters. Fortunately, both technical difficulties and costs of reproduction of such “witness” complex metal parts are significantly alleviated by the continuing advancement of AM technology. Therefore, the SEM geometric characterization can be served as either a supplement/verification method for CT scan or independent metrology for additively manufactured metallic parts. In this work, the SEM characterization combined with the image segmentation technique was utilized for dimensional metrology and analysis of the microchannels made by AM.

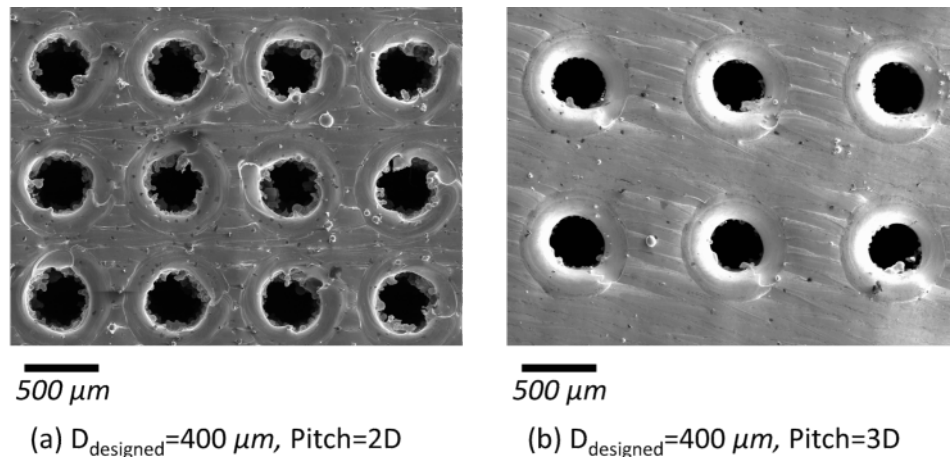


Figure 1.3 Morphology differences between microchannels with different hole pitches, (a) Hole spacing of 2D with more particle attachments on the edges; (b) Hole spacing of 3D with smoother hole profiles

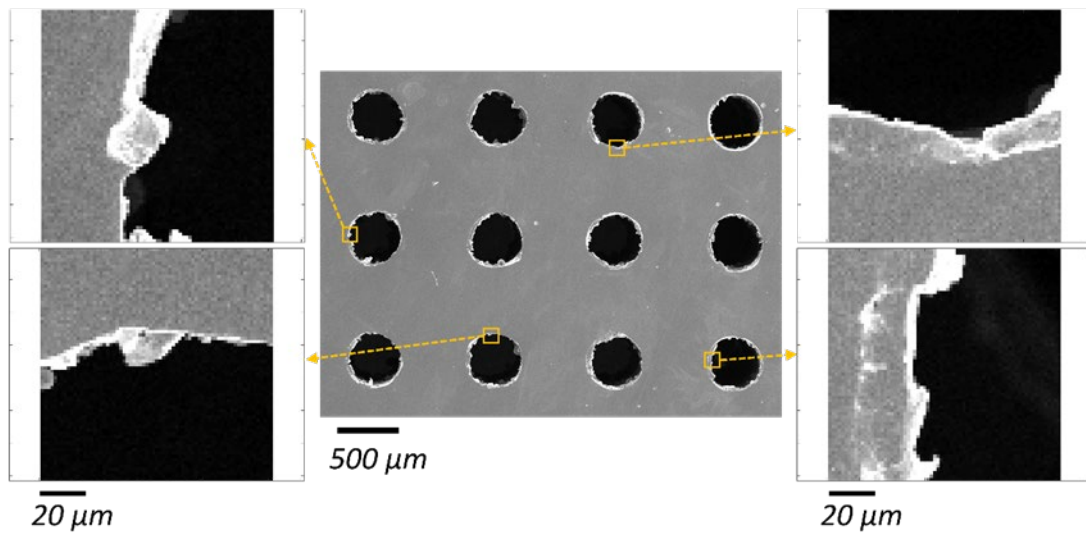


Figure 1.4 Brightened edge effect of SEM photograph

The second purpose of this work is to improve the channel surface qualities of the printed specimens. As mentioned above, deformations due to hatch overlaps and particle attachments have a significantly negative impact on the dimensional accuracies of the printed microchannels. Therefore, an offset of the channel size from the designed value to the as-produced value is expected. To address this deformational offset issue, a CAD redesign compensation method for the samples was employed based on the correlations between the designed channel size and the as-produced value, which were obtained in the SEM characterization task. A follow-up electrochemical polishing (ECP) method was selected as a post-printing process to further mitigate surface roughness. ECP process is a surface treatment process based on the localized anodic dissolution of conductive samples immersed in acid solutions. Due to higher electric density in the protruding part of a surface profile, the dissolution rate is higher at corners and burrs, leading to a leveling effect of the surface to reduce roughness. Thus, the ECP method can improve the surface

finish regardless of the complex geometries of the treated sample, which is suitable to post-process the microchannels made by DMLS.

1.1.3 Heat Transfer in Transpiration Cooling

After AM fabrication, dimensional characterization, and surface quality improvement of the test specimens, the next goal is to investigate the thermal performance of transpiration cooling structures. As one of the external cooling techniques, the effect of transpiration cooling depends on the formation of coolant film coverage and the flow interaction in the mixing zone at the target surface. The schematic diagram in Fig. 1.5 shows a comparison between a flat surface heat transfer and a surface covered by coolant film. In the flat surface case, heat flux q_0 , which represents the thermal energy absorbed by the component, is governed by Newton's law of cooling in Eq. (1.1).

$$q_0 = h_0(T_r - T_w) = h_0(T_g - T_w) \quad (1.1)$$

$$q = h_f(T_r - T_w) = h_f(T_{aw} - T_w) \quad (1.2)$$

$$\frac{q}{q_0} = \frac{h_f(T_{aw} - T_w)}{h_0(T_g - T_w)} = \frac{h_f}{h_0}(1 - \eta/\varphi) \quad (1.3)$$

$$\eta = \frac{T_g - T_{aw}}{T_g - T_c}, \varphi = \frac{T_g - T_w}{T_g - T_c} \quad (1.4)$$

When coolant is injected into the mainstream to form a new boundary layer, the coolant and hot gas's mixture temperature near the wall declines. The driving temperature potential of the heat flux to the wall between the reference temperature T_r and the wall temperature T_w is lower than that in the case of no coolant injection, because the adiabatic wall temperature T_{aw} with

coolant film is lower than the freestream gas temperature T_g . Eq. (1.2) describes the heat flux into the component driven by such temperature potential with film coverage. In order to take advantage of the coolant film, the heat flux ratio q/q_0 needs to be smaller than 1. Based on the derivation of Eq. (1.3), three parameters, adiabatic cooling effectiveness η , overall cooling effectiveness ϕ , and heat transfer coefficient ratio h_f/h_0 , are needed to evaluate the heat load reduction to the target surface. In most experimental studies on transpiration cooling, only overall cooling effectiveness ϕ and adiabatic cooling effectiveness have been investigated to evaluate cooling performance. On the contrary, few studies have looked into the heat transfer coefficient of transpiration cooling, due mainly to the limitations of the traditional HTC investigation methods for film cooling.

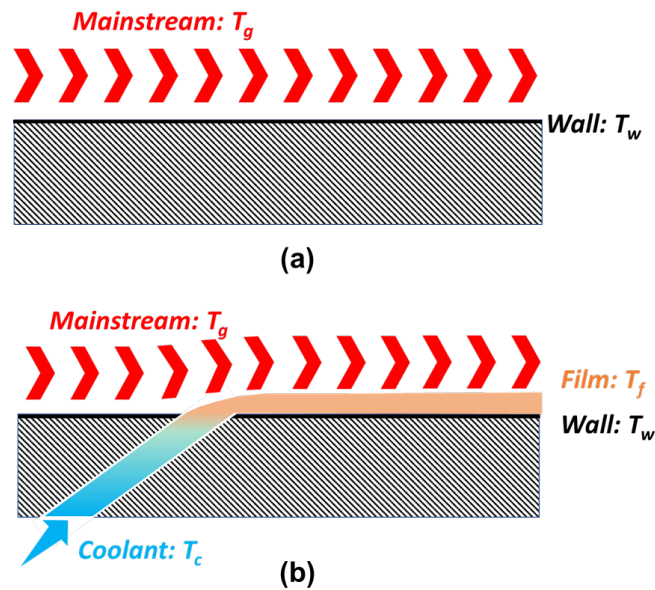


Figure 1.5 Comparison between a flat surface heat transfer and a surface covered by coolant film

In the open literature, two major measurement methods, the transient heat transfer tests and the foil-heater steady-state tests, have been frequently employed to obtain the heat transfer coefficients for film cooling studies. In the transient heat transfer test (Fig. 1.6), the test surface

made by low thermally conductive material is initially exposed to a uniform environment before a sudden change of the convection wall boundary condition. During the temperature transient, the target surface temperature at different times or in two different sets of experiments is recorded by either TLC recorder or IR camera. With the assumption of a semi-infinite solid medium of the test plate, the second-order PDE of transient conduction function (Eq. (1.5)) is given as:

$$\left\{ \begin{array}{l} k \frac{\partial^2 T}{\partial^2 y} = \rho C_p \frac{\partial T}{\partial t} \\ -k \frac{\partial T}{\partial y} \Big|_{y=0} = h(T_{aw} - T_w) \\ T|_{y=\infty} = T_i \\ T|_{t=0} = T_i \end{array} \right. \quad (1.5)$$

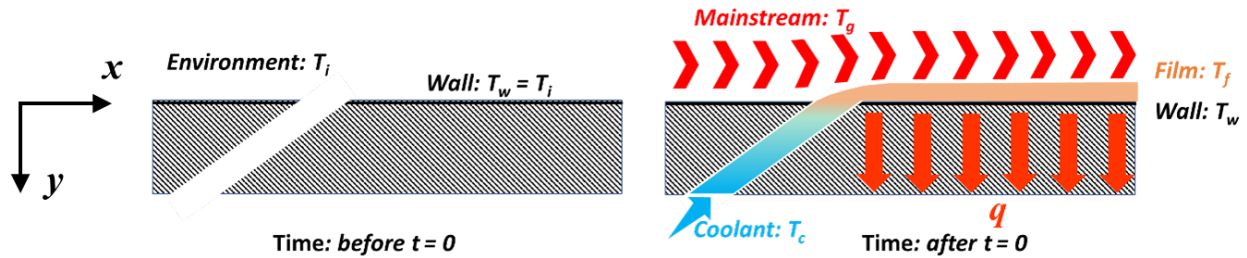


Figure 1.6 Schematic of the transient heat transfer test

By recording the transient surface temperature changing process, the surface heat transfer coefficient could be obtained. Vedula and Metzger [12] firstly presented a method from transient tests to obtain the h and T_{aw} value using the liquid crystal technique. The solutions to the governing equations (Eq. (1.6) - (1.7)) are given as:

$$\frac{T_{w1} - T_i}{T_{aw} - T_i} = 1 - \exp\left(-\frac{h_f^2 \alpha t_1}{k^2}\right) \operatorname{erfc}\left(\frac{h_f \sqrt{\alpha t_1}}{k}\right) \quad (1.6)$$

$$\frac{T_{w2} - T_i}{T_{aw} - T_i} = 1 - \exp\left(-\frac{h_f^2 \alpha t_2}{k^2}\right) \operatorname{erfc}\left(\frac{h_f \sqrt{\alpha t_2}}{k}\right) \quad (1.7)$$

Due to the inherent difficulties of recording two events far apart in a single test, this technique has been better applied to solve both the unknowns from two separate transient tests to enhance the test accuracy. As the turbulent convection is predominantly determined by flow dynamics rather than thermal conditions, the two equations above can be solved using two different but closely related tests under the same flow conditions.

However, in transpiration cooling, unlike the test plate in film cooling, the target plate is no longer a solid plate but a porous medium instead. With numerous cooling passages inside the plate, the semi-infinite solid medium theory no longer holds for transpiration cooling structures. Thus, the transient test fails to serve transpiration cooling for HTC evaluations.

Instead of imposing a sudden change of boundary conditions at the test surface during the transient test, the steady-state heat transfer test (Fig. 1.7) uses a foil heater attached to the test surface to provide constant heat flux into the film. Based on this known heat flux and surface temperatures measured under the two conditions: with the heater on or off, the heat transfer coefficient can be calculated from Eq. (1.8).

$$q = h(T_w - T_{aw}) \quad (1.8)$$

Where T_w is the wall temperature with the heater on and T_{aw} is the adiabatic wall temperature, which is measured when the surface heater is off under the same flow condition.

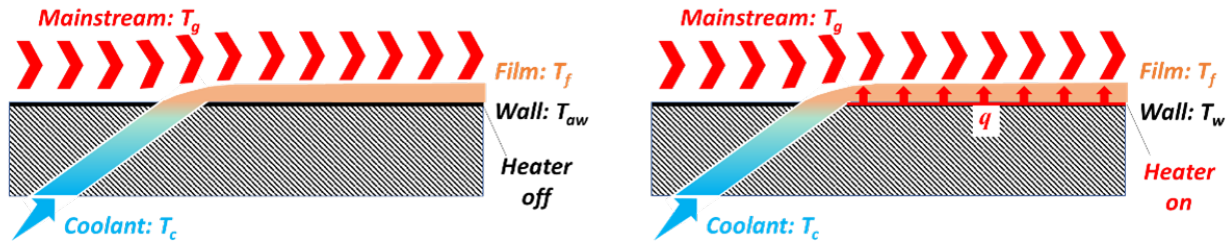


Figure 1.7 Schematic of the steady-state heat transfer test for film-covered surface

To apply this method to transpiration cooling is also very challenging. First, the foil heater has to be fabricated in complex shapes to avoid blocking the numerous outlets at the target surface. Second, when attaching such foil heater onto the transpiration cooling surface, precise alignment between the heater and the hole outlets is a -difficult task as well. To tackle these challenges, this study used a micro-lithography method to fabricate a silver coil pattern on top of the additively manufactured polymer porous media as the surface heater for heat transfer coefficient measurement. The coil patterns were designed based on the distributions of the cooling channel outlets to make sure no ejection blockage and to provide uniform heating covering the target surface. By adjusting the operation conditions, on/off status of the surface heater, the wall temperature and the adiabatic wall temperature could be obtained to calculate the heat transfer coefficient. This steady-state heat transfer test was conducted using an infrared (IR) camera for surface temperature measurement.

1.1.4 Thermal Performance Predictions from Geometric Dimensions

The last goal of this study is to establish a model to predict the overall cooling effectiveness from the geometric metrology results of the straight-channel transpiration cooling structures. With numerous outlets distributed at the target surface, the cooling effectiveness distribution is

determined by many factors, including coolant accumulation, vortex interaction, turbulence intensity, and thermal conductivity of the porous plate, all of which are impacted nonlinearly by a number of geometric parameters, such as microchannel size, channel pitch, injection orientations, etc. The massive number of channels would also lead to a parameter exploding for investigating transpiration cooling structures if each channel is treated separately. Although extensive efforts have been put into studies of the thermo-fluid mechanism of transpiration cooling, few analytical models have been established to translate the geometric information to thermo-fluid performance. The current film cooling superposition model developed from Seller [13] is not able to capture the nonlinear correlations accurately for multi-row film cooling/effusion cooling/transpiration cooling. The recent development of machine learning algorithms in the computer vision field could provide a new perspective of developing a prediction model to map geometrical features to the cooling performance. Based on the large amount of training data fed to the neural network, the nonlinear correlations between the input surface geometries and the surface temperature as the output could be learned by the neural network. In this work, the surface geometries based on dimensional metrology results were used as the model input, while the corresponding CFD simulation results as the ground truth data to train a prediction model. The trained parameter matrix can be used to directly acquire the cooling effectiveness distribution based on the hole size distribution and possible blockage ratio, which could be applied for future geometric design and optimizations.

In summary, the present dissertation work consists of two major parts: dimensional metrology of AM transpiration cooling channels and thermo-fluid investigation on the produced test specimens. In the first part, the SEM characterization, combined with the image segmentation method, was employed to analyze the geometric information of the microchannels. A follow-up CAD model compensation based on characterization results and an ECP process were applied to

improve the surface finish. In the second part, using an innovative micro-lithography technique to fabricate surface heater, a steady-state test on stereolithography (SLA)-printed specimens was established to investigate the HTC at the target surface of transpiration cooling. Moreover, a neural network model was developed to connect the two parts of this work, predicting the thermo-fluid performance based on the dimensional metrology results.

1.2 Literature Review

This section will review the past studies to illustrate the state of the art of techniques used in this study and the challenges that remained to be addressed. These studies were categorized into five aspects: 1) AM capabilities for metallic porous media fabrication; 2) Dimensional metrology for AM parts; 3) Cooling effectiveness studies on transpiration cooling; 4) HTC studies on film cooling; 5) Theoretical modeling to predict cooling performance.

1.2.1 AM Capabilities for Metallic Porous Media Fabrication

The most common fabrication methods of porous metal include metal foam, powder sintering porous media, and metal wire mesh. Metal foam is made of molten metal foamed by gas injection of chemical decomposition before the solidification process [14]. This type of metallic porous media could provide extremely high porosity up to 90%. However, the mechanical strength of metal foam could hardly meet the requirement of turbine blades. Also, with arbitrarily distributed voids inside the media, the metal foam hardly provides effective cooling passages for transpiration cooling despite the high porosity it has [15]. The packed metal powder sintering is

another method to fabricate metallic porous media [16, 17]. The metal powders are packed together and sintered under the melting point to desired shapes in the mold. This method could provide similar porosity of the metal part but higher strength compared to metal foam. However, this method can not design and control the porosity distribution precisely in the sintering process, generating some non-effective porosity for transpiration cooling, i.e. non-interconnected voids which would reduce the cooling performance. The third fabrication technique, metal wire mesh, is made by weaving several layers of wire meshes and sintering them to one piece [18]. It has advantages of relatively high porosity and high mechanical strength, but the lack of design flexibility and shape controllability restricts its potential for applications on the advanced cooling structure [19].

In recent years, the rapid development of DMLS additive manufacturing has offered a new avenue for the fabrication of complex metal parts. In order to fabricate transpiration cooling structures using DMLS, three concerns have to be addressed on the density of the printed alloy, the mechanical strength of the test coupon, and the capability of producing intricate microscale features. In the density studies of DMLS, extensive investigations on the printing parameters for different materials such as SS316 [20], Ti6Al4V [21], and IN718 [22] have shown that the density of DMLS parts could reach 99.5% or even higher. Such dense part with little porosity improves the ductility and reduces the chance of stress ruptures in final products [23]. Moreover, as the DMLS technique comes to maturity, the mechanical strength of the produced parts increases significantly as well. Amato et al. 's work [24] demonstrated the γ'' phase precipitates in the as-printed parts made the tensile strength comparable with wrought Inconel 718 alloy. The tensile test and micro-indentation test in Lu et al. 's work [25] indicated that both the ultimate tensile strength and the hardness of DMLS specimens were comparable to the precipitation-hardened Inconel 718

alloy. Rickenbacher et al. [26] showed that the tensile strength of IN 738 part made by DMLS could be higher than those of the cast. The fatigue performance of IN 718 made by DMLS was found in Emuakpor et al. [27]'s work to be comparable with the cold-rolled alloy. With significantly improved mechanical properties of AM parts in recent years, the design flexibility potentials of AM can be further exploited for more intricate geometries. In recent studies, a lot of metal parts with complex features, such as microscale channels [28-30], cellular lattice [31-33] and metal matrix composite [34, 35] have been intensively investigated for potential applications in compact heat exchangers, advanced turbine blade cooling structures and other aerospace/bioengineering/medical industries. Therefore, with the capabilities of making parts with high density, comparable strength, and increased complexity, the DMLS method was chosen to fabricate the transpiration cooling structures.

1.2.2 Dimensional Metrology for AM Parts

Microfocus X-ray computed tomography (micro CT) emerged as the most popular technique to tackle the challenge of surface roughness characterization for AM metallic parts in the last decade. This nondestructive evaluation technique has the capability to reconstruct the 3D model of the workpiece based on a large number of 2D sliced x-ray radiographs. Therefore, an increasing number of studies have applied micro CT technology into surface roughness characterization. Van Bael et al.[36], Kerckhofs et al.[37], and Kim et al.[38] performed micro-CT scans to conduct surface roughness and porosity analysis on additively manufactured strut networks made by Ti6Al4V and other titanium alloys. Karne et al.[39] investigated the printing quality of a straight tube with a wall thickness of 1mm made by stainless steel 316(SS316). Snyder et al. [40] fabricated a single row of microchannels along different printing directions in the DMLS

machine. The diameter of the channel was 0.51mm, and the wall thickness between adjacent channels was around 0.8mm. Their micro CT scan results showed that the vertical printing direction provided the highest quality.

Although considerable efforts have been put into surface roughness measurement using micro CT, several inherent limitations of this technique still exist to obtain accurate test results. Firstly, the basic principle of CT scan is to measure the remaining X-rays that travel through the interested object to calculate the presence of the material along the X-ray path. However, different materials with different attenuation coefficients, which represent the absorption abilities of X-rays, lead to different penetration rates. To measure the features made by metals with high attenuation coefficients, such as nickel, iron, or lead, requires either small thickness of metal parts along the X-ray path, or X-rays generated by much higher energy [41]. However, increasing the X-ray excitation energy will result in a larger focus spot, which reduces the accuracy of detecting small features of the workpiece. Focus spots of commercial CT scanners today can be controlled under 1 μm diameter when the applied voltage is less than 250keV, which can only penetrate a few millimeters for heavy metals. As the voltage goes from 250keV to 450keV, the spot diameter increases significantly to 30-1000 μm due to heat dissipation on the X-ray generation target, which limits the ability to detect small features [42]. Secondly, for alloy specimens with different elemental compositions, different attenuation coefficients cause X-ray to scatter inside the workpiece, which increases noise and uncertainties of X-ray detection [42, 43]. Such uncertainties would increase the unsharpness of CT images, raising difficulties on the spatial discretization based on voxel data [44, 45]. Considering the inhomogeneous nature and complex geometries of the alloy parts made by AM, such uncertainties caused by complex composition and surface features should deserve more attention and study. For instance, more prudent calibration work is

required to obtain higher accuracy of geometric analysis. Other factors impacting the dimensional metrology, including beam hardening, rotation axis errors and reconstruction errors in both the detection process and the data reduction process, were systematically discussed in Kruth et al. 's work [42]. As stated in their paper, although CT scans showed high potentials for nondestructive evaluation, it still required substantial developments to bring it to maturity.

Scanning electron microscope (SEM), a well-known tool for material characterization, is capable of providing high-quality micrographs using second electron mode with resolution smaller than 0.1 nanometers [10]. Along with higher resolution, SEM can provide better control of spot size and lens focus, smaller aberrations, and greater depth of field (under long working distance) compared to optical microscopy. With such advantages, SEM microphotograph is favorable to demonstrate detailed surface features for 2D morphology analysis. Image segmentation techniques can then be introduced to extract the interested features from the image and quantify the geometric information, including feature areas, perimeters, surface porosities, etc. [46, 47]. The thresholding method for image segmentation uses different gray levels to divide the image into different sections, each of which contains similar textures. This method was used by a lot of studies on porosity analysis for thermal spray coating [48], nanofibers mat [49] and claystone [50] from SEM photographs. The other image segmentation method, the edge detection method is to find the pixels with the largest discontinuities of the grayscale values in the image. By extracting those pixels, the feature edge profiles can be identified. This method has been applied to line-edge detection of photoresist for nanoscale lithography[51, 52] and segmentation of surface features such as clustered nuclei[53] and red blood cells[54]. The SEM characterization method, assisted with the two feature identification algorithms, was used for dimensional characterizations of additively manufactured metal parts in this work.

1.2.3 Cooling Effectiveness Studies on Transpiration Cooling

The first study on transpiration cooling can date back to the late 1940s. Rannie et al. [55] was among the earliest to investigate transpiration cooling, establishing a theoretical model to analyze the thermal boundary layer at the target surface. The model predicted high potential of transpiration cooling to cool down the wall temperature. The advantages of transpiration cooling were also investigated theoretically by Eckert and Livingood [56], who compared the effect of transpiration cooling with convectively cooled- and film cooled-walls. The derived ratio of the Stanton number in their research, $St_g/St_{g,0}$, was proven by Moffat et al. [57] and Simpson et al. [58]’s experimental studies in the 1960s. Later, Laganelli’s work [59] proved the higher cooling effectiveness of transpiration cooling than film cooling in high-speed flow conditions. With the proof of superiority in analytical models and the advancement of fabrication techniques for porous metal, a steadily growing amount of experimental studies, as shown below, have been put into evaluating and improving the efficiencies of transpiration cooling in the last few decades.

In experimental flat-surface film cooling studies, most test plates were made by low thermally conductive materials to reduce heat conduction into the plate, making the wall temperature approximate to the adiabatic wall temperature, T_{aw} . In such tests, the obtained wall temperature would be considered as T_{aw} to calculate the adiabatic cooling effectiveness, η . However, in experimental studies of transpiration cooling, most of the test specimens were metallic porous media, making it difficult to obtain the adiabatic wall temperature T_{aw} . Therefore, most transpiration cooling studies looked into overall cooling effectiveness φ (Eq. (1.4)) to evaluate the cooling performance. Brocq Et al. ’s work [60] on discrete-hole transpiration cooling structures showed a higher density of injection holes could improve cooling effectiveness. Liu et al. [61] and Langener et al. [62] compared the effect of various gaseous coolant on cooling effectiveness φ ,

both demonstrating that the coolant with higher specific heat could provide better protection for the hot surface. Zheng et al. [63] conducted transpiration cooling experiments for sintered porous struts in supersonic flow. Their findings showed that the increase of injection ratio from 3.8% to 5.4% provided an insignificant rise in the averaged cooling effectiveness, indicating increasing the coolant mass flow rate was not the most economical method to enhance cooling performance. Also, higher thermal conductivity of the porous media led to higher φ values. Zhao et al. 's liquid phase-change work [64] showed using reduced wall thickness in the nose cone tip was effective in increasing the cooling effectiveness in the stagnant region. Huang et al. 's work [65] showed that the φ in phase-change transpiration cooling increased by more than 30% at injection ratio of 0.2% as the bronze particle size forming the porous plate dropped from 600 μm to 200 μm .

When using metallic materials as the porous media for transpiration cooling tests, the thermal conduction through the wall impacts the cooling effectiveness significantly. In order to compare the cooling effects of different test coupons with various structural designs, the heat conduction effect should be eliminated for the evaluation. Langener et al. [66, 67] proposed a new non-dimensional temperature, Φ , as defined in Eq. (1.9), to mitigate the impact of heat conduction. Instead of using mainstream temperature in the overall cooling effectiveness φ , this non-dimensional temperature used the actual wall temperature measured with no coolant blowing. This definition was widely accepted in many transpiration cooling studies, some of which denoted this non-dimensional term as “adiabatic cooling effectiveness”. However, due to heat conduction, the metal wall temperature without coolant coverage is not an adiabatic wall. To distinct the term from the adiabatic cooling effectiveness in film cooling studies, the non-dimensional temperature Φ in Eq. (1.9) will be referred to as the transpiration cooling effectiveness in this work. Wang et al. [68] experimentally investigated the Φ distribution on an unequal thickness porous wall using liquid

water. An optimal injection ratio was found to minimize the driving force for the liquid transport through the porous media and keep the cooling efficiency at a high level. This optimal value increased with an increase of mainstream temperature and Reynolds number. Jiang et al. 's work [69] investigated the Φ of a strut with a combination of transpiration cooling and film cooling schemes. This combination could cool both the leading edge and other parts of the strut more effectively and uniformly. Wu et al. [70] reported the Φ for two types of schemes in nose cone-shaped metal wall: uniformly porous wall and wall with gradually changing porosity. The results showed that the gradual gradient layout provided significant improvement in transpiration cooling effectiveness. Xu et al. [19] and Ma et al. [71] studied the Φ distributions of woven wire mesh structures. Both of their studies showed that the transpiration cooling effectiveness could get higher than 0.5 with a porosity higher than 55%. In the present study, the transpiration cooling effectiveness was used as an indicator to evaluate the metallic AM test specimens.

$$\Phi = \frac{T_{w(M=0)} - T_w}{T_{w(M=0)} - T_c} \quad (1.9)$$

1.2.4 Heat Transfer Coefficient Studies on Film Cooling

While most of the studies on heat transfer coefficients of external cooling are directed to film cooling, few experimental studies have investigated the HTC for transpiration cooling. In film cooling, as mentioned in Section 1.1, two classic experimental methods, the steady-state surface heater technique and the transient thermography method, have been extensively used to obtain the heat transfer coefficients.

On the steady-state front, Goldstein and Eriksen et al. [72-77] had applied the foil heater technique to investigate the HTC of film cooling for various structures since the 1960s. In their

works, the thin-film heaters were taped or cemented to the low thermally conductive surface downstream of the coolant injection holes, generating certain heat flux during the test to calculate HTC as defined in Eq. (1.8) above. Similar surface heater techniques have been used to obtain HTC distributions in a large number of studies, including Mick and Mayle (1988) [78], Takeishi et al. (1990) [79], Mehendale and Han (1992) [80], Ou et al. (1994) [81]; Kelly and Bogard (2003) [82], Yang and Zhang (2012) [83], Yang et al. (2017) [84], Li et al. (2019) [85]. Although the surface heater technique has been proven to be successful in film cooling studies, applying this method to the transpiration cooling surface is a great technical challenge. In transpiration cooling, as the cooling passages go into microscale, hundreds of cooling channel outlets gather in a small area of only 1cm^2 , leaving the space between adjacent channels less than 1mm . In this case, it would be extremely difficult to attach the foil/tape heater onto the surface with perfect alignment making no blockages to the channel outlets. Additionally, because most of the porous media in traditional transpiration cooling studies are sintered metal powder plates or metal wire mesh, it is difficult to replicate the low thermally conductive plate with an identical cooling passage design.

In the 1990s, the development of the non-intrusive techniques of temperature measurement expanded the visions of the HTC studies in film cooling. Vedula and Metzger (1991) [12] firstly introduced a transient heat transfer technique to obtain HTC distributions downstream of one row of film cooling holes using thermochromic liquid crystals. In their study, the test plate was made of low thermally conductive acrylic plastic, which was coated with a thin layer of microencapsulated thermochromic liquid crystals (TLC). The test was initiated by simultaneously introducing mainstream flow and film injection into the target surface, which was at a uniform initial temperature before the test. The conduction model of the test plate, which was based on a 1-D semi-infinite solid assumption, is given in Eq. (1.5). The transient temperature response of the

target surface was displayed by the color change of the TLC during the test. In one single temperature transient, two different color-change times can be recorded to solve the governing equations (Eq. (1.5)) to obtain h and T_f . Although theoretically, recording temperatures at different instants during one single transient test could provide solutions to this conduction problem, most of the studies used two separate transient tests to reduce the uncertainties. Chyu and Hsing (1996) [86] firstly introduced a thermographic phosphor fluorescence technique to measure the heat transfer coefficient for film cooling. The measurement was based on the temperature-sensitive fluorescence of a thermographic phosphor, acquiring a series of transient, full-field surface temperature images during a heating process to solve the transient relations. Yu and Chyu (1998, 2002) [87, 88] performed two different, but closely related, heat transfer tests under the same flow conditions. One of the two tests used a film injection close to, but slightly lower than, the heated mainstream, while the other used an unheated or slightly heated injection. Careful selection of test temperatures was required to ensure the two relations (Eq. (1.6) - (1.7)) being well coupled for yielding a solution for the two unknowns. Ekkad et al. (2004) [89] firstly introduced the transient infrared thermography technique into the HTC studies in film cooling. In their study, two IR images at two different instants during the single test were recorded with the surface temperature distributions to solve the two relations (Eq. (1.6) - (1.7)) mention above. Using this method, the initial temperature distribution of the target surface could be obtained easily compared to using TLC technique. The transient heat transfer technique has been widely used in plenty of other studies on film cooling, such as Ekkad et al. (1997) [90], Chen and Chyu (2011) [91], Ligrani et al. (2013) [92], Rogers et al. (2017) [93], Li et al. (2019) [94]. However, the 1-D infinite solid plate assumption of the conduction model does not hold for the transpiration cooling media. This is because numerous transpiration cooling passages inside the solid plate generate much more

complex heat convection inside the wall, which is different from 1-D conduction from the hot side to the cool side in the solid plate downstream of the film cooling holes.

Most of these studies on the HTC from steady-state tests and transient tests showed that the ratio of HTC between the cases with and without injection (h_f/h_o) increased with the blowing ratio. However, when the blowing ratio was larger than 1 for single row film cooling and 0.5 for multi-row film cooling, the tendency of increasing HTC with a higher blowing ratio was no longer significant. At low blowing ratios lower than 0.5 for single row film cooling, the HTC with injection was lower than that without injection since the injection thickened the boundary layer. Also, the HTC for multi-row film cooling was increasing along the mainstream direction towards downstream due to higher turbulence mixing generated by subsequent rows of coolant injection.

In the present study, the stereolithography (SLA) AM was employed to fabricate the resin plates with transpiration cooling designs. A micro-lithography technique would be used to coat the microscale surface heater on top of the low thermally conductive test coupon. The coil pattern was designed based on each individual unit cell to produce uniform heat flux without blocking any coolant outlets. In this way, the classic steady-state heat transfer test mentioned above could be applied to the transpiration cooling to obtain the heat transfer coefficient.

1.2.5 Theoretical Modeling to Predict Cooling Performance

Many researchers have studied the thermal fluid aspects of external cooling, especially for film cooling. Due to a large number of contributing factors to the cooling effectiveness, the analytical model previously obtained has to be simplified with some specific limitations to capture the main characteristics of the complex flow field. The earliest efforts to investigate heat transfer on surfaces covered by coolant film were from Hatch and Papell (1959) [95] and Hartnett et al.

(1961) [96]. Their work established the theoretical model to capture the temperature profiles beneath the boundary layer generated by a single slot injection. Further studies on the effectiveness correlation with a single hole or a single row of film cooling were given by Sturgess (1971) [97], Pai and Whitelaw (1971) [98], Muckerjee (1976) [99], and Kruse (1985) [100]. Their studies provided substantial information to establish a model with two basic presumptions: 1) the cooling effectiveness was 1 at the ejection position; 2) an exponential decay function was used to present the temperature rise of the coolant film downstream the injection holes, in which the exponent was determined from experiments. The correlations yielded reasonable results for far positions downstream of the ejection position but gave too high values near the ejection holes. Baldauf et al. (2002) [101] improved the model and used a base curve to model the ejection core area to capture the cross-flow mixing and the adjacent jet interactions in the zone near the injection holes. For multi-row film cooling, Seller (1963) [13] proposed an additive model to simulate the superposed effects of the coolant film. The model could derive the overall cooling effectiveness of multi-row film cooling from the single-row film cooling effectiveness obtained from others' correlation or experimental data. In this model, the film temperature at the downstream of a row of holes could be calculated based on the Eq. (1.10) but substituting the free stream temperature with the upstream film temperature. For instance, the film temperature T_{f2} in the region between the second row and the third row was given as Eq. (1.11), assuming that the freestream temperature upstream the region between the second row and the third row was approximate to the film temperature of the area between the first row and the second row. Using this iterative substitution, a cumulative product was derived to predict the cooling effectiveness in the region between the N th row of holes and the $(N+1)$ th row as defined in Eq. (1.14). This additive model was also summarized and tested experimentally by Muska et al. (1976) [102]. Fuqua and Rutledge (2020) [103] modified the model

by introducing a new parameter ξ to evaluate various conditions with different coolant injection temperatures. However, Takeishi et al. (2016) [104] and Meng et al. (2018) [105] showed that the accuracy dropped dramatically for high blowing ratios when using this superposition model to reach a reasonable agreement with experimental data for low blowing ratios smaller than 1. In addition, the superposition model could hardly capture the effect from the nonuniformly distributed ejection holes and variation of hole sizes and shapes.

$$T_f = T_g - \eta(T_f - T_c) \quad (1.10)$$

$$T_{f2} = T_{f1} - \eta_2(T_{f1} - T_c) \quad (1.11)$$

where

$$\eta_1 = \frac{T_g - T_{f,1}}{T_g - T_c} \quad (1.12)$$

$$\eta_2 = \frac{T_g - T_{f,2}}{T_g - T_c} \quad (1.13)$$

$$\eta = \sum_{i=1}^N \eta_i \prod_{j=0}^{i-1} (1 - \eta_j) \quad (1.14)$$

Due to more complex cooling passages in transpiration cooling, the analysis of the turbulent boundary layer characteristics such as boundary layer profile, turbulence mixing, skin friction, and flow separation is more challenging than film cooling. In early studies, Rannie et al. (1947) [55] assumed that the low-speed secondary flow injected into the mainstream had very little influence on the mainstream outside the laminar sublayer. Based on the assumption, the laminar sublayer thickness δ and the velocity u_δ at $y = \delta$ can be derived from the flat surface case without injection. The overall cooling effectiveness can be found as

$$\varphi = \frac{T_g - T_w}{T_g - T_c} = 1 - \frac{e^{-36.9Pr_g Re_D^{0.1} F}}{1 + \frac{C_{p,c}}{C_{p,g}} (1.18 Re_D^{0.1} - 1)(1 - e^{-36.9 Re_D^{0.1} F})} \quad (1.15)$$

Eckert and Livingood [56] employed the same assumption in the theoretical analysis that the thickness of the laminar sublayer at the transpiration-cooled surface keeps unchanged from the convection-cooled surface. Another assumption made in their work is the coolant temperature is equal to the wall temperature at the target surface. According to this local thermal equilibrium assumption, the wall temperature can be calculated by the energy balance equation to give the overall cooling effectiveness:

$$\varphi = 1 - \frac{1}{1 + \frac{C_{p,c}}{C_{p,g}} \frac{Re_x^{0.1}}{2.11} (e^{57.03 F Re_x^{0.1} Pr^{0.667}} - 1)} \quad (1.16)$$

The local thermal equilibrium assumption has been used in many analytical and numerical studies on porous media heat transfer, as summarized in Rohsenow and Hartnett's book [106]. Using the local volume averaging method, the energy balance equations for the two phases (liquid and solid) are given as:

$$\text{Solid: } (1 - \varepsilon)(\rho c_p)_s \frac{\partial T_s}{\partial t} = \nabla \cdot (k_{eff,s} \nabla T_s) - h_{sf} a_{sf} (T_s - T_f) \quad (1.17)$$

$$\text{Fluid: } \varepsilon(\rho c_p)_f \frac{\partial T_f}{\partial t} + (\rho c_p)_f u \cdot \nabla T_f = \nabla \cdot (k_{eff,f} \nabla T_f) + h_{sf} a_{sf} (T_s - T_f) \quad (1.18)$$

where ε is the porosity of the porous media. $k_{eff,s}$ and $k_{eff,f}$ are the effective thermal conductivities of the solid phase and the liquid phase, respectively. The term $h_{sf} a_{sf} (T_s - T_f)$ represents the heat flux exchanged convectively between the two phases in the porous media.

In the local thermal equilibrium assumption, the solid phase and fluid phase is considered to reach the thermal equilibrium in the porous media, leading to $T_s = T_f$. Thus Eq. (1.17) – (1.18) can be simplified to one equation given as:

$$(\rho c_p)_{eff} \frac{\partial T}{\partial t} + (\rho c_p)_f u \cdot \nabla T = \nabla \cdot (k_{eff} \nabla T) \quad (1.19)$$

where

$$(\rho c_p)_{eff} = (1 - \varepsilon)(\rho c_p)_s + \varepsilon(\rho c_p)_f \quad (1.20)$$

When the fluid flows slowly through the porous media, the heat exchange between the two phases goes sufficiently to reach the thermal equilibrium state. However, the high coolant velocity accompanied by the significant heat flux from the target surface in most of the transpiration cooling cases results in thermal non-equilibrium between the two phases. Therefore, the non-equilibrium model (Eq. (1.17) – (1.18)) has gained noticeable interest for heat transfer analysis in porous media. Wang and Wang (2006) [107] theoretically analyzed the 1-D thermal non-equilibrium model in transpiration cooling. The results showed that the non-dimensional coolant injection rate M and the Bi number in the pores were the two decisive factors causing the thermal non-equilibrium. By analyzing the local thermal equilibrium model's error, they provided the criterion ($M \geq 0.223Bi^{0.507}$) that the non-equilibrium model must be used. To improve the thermal non-equilibrium model's accuracy, the two parameters, the effective thermal conductivity and the convective heat transfer coefficient in the porous media, need to be properly evaluated. Hsu and Cheng (1990) [108], Jiang et al. (1996) [109], Ichimiya (1999) [110], Nield (2002) [111], and Kuwahara et al. (2011) [112] investigated the effective thermal conductivities in both phases, $k_{eff,s}$ and $k_{eff,f}$, based on the material properties and geometry characteristics in various porous media. Wakao (1976) [113], Dixon and Cresswell (1979) [114], Achenbach (1995) [115], Muralidhar and Suzuki (2001) [116], and Pallares and Grau (2010) [117] provided a series of correlations of the heat transfer coefficient inside different types of porous media by experimental curve fitting, numerical simulation or theoretical analysis. All the studies laid a solid foundation

for the theoretical or numerical solutions of the porous wall's temperature field in transpiration cooling.

The acquisition of the temperature field in the porous media theoretically requires many assumptions to simplify the model, which may reduce the solutions' accuracy. Solving the conjugate heat transfer problem in such complex geometries is also a time-consuming process, even with advanced computing techniques. Moreover, the dimensional variations of the porous media made by AM in this work bring about more difficulties to the “translation” from geometric characteristics to temperature distributions. The success of machine learning algorithms in the computer vision field in the last decade may offer new opportunities to tackle the challenging tasks of modeling transpiration cooling. The machine learning models' strong capability to regress or classify the pixel-wise values from input to output image could benefit the “translation” work mentioned above. The data from the literature, numerical simulation, or experimental work could contribute to a machine learning model's training to improve both the accuracy and speed of the performance prediction task. Yang et al. [118, 119] firstly developed a three-layer convolution model to predict the overall cooling effectiveness of transpiration cooling with uniform channel sizes. The model could capture the effect of the various pore distributions on the averaged cooling effectiveness with root mean square error at 5.4%. However, the size of the receptive field of the model restricted the capability to predict the thermo-fluid impact from the holes far away to the interested location. Also, the use of the logic number “1” to present a single opened hole restricted the model to capture the effect of hole size variations in transpiration cooling.

1.3 Present Work Statement

To address the challenges mentioned above for dimensional metrology and thermo-fluid studies, four major tasks were performed as described below.

1.3.1 Dimensional Characterization and Surface Improvement of Straight-Hole Test

Samples

The research in this present dissertation utilized the SEM characterization combined with a multi-level image segmentation method to analyze the geometric information of AM-made Inconel 718 microchannels statistically. Three parameters, the averaged as-printed channel size, the arithmetical mean deviations of the channel profile, and circularity tolerance, were obtained to evaluate the printing qualities of the straight-hole transpiration cooling specimens. Once the correlations between the as-printed channel size and the designed values were acquired from the metrology results, a CAD-based compensation method was used to redesign the samples, making the as-produced channel sizes closer to the objective values. After the reproduction and characterization of those redesigned samples, the ECP process was employed on one selected redesigned specimen to further improve the surface qualities. Fig. 1.8 shows an overview of this task, which will be demonstrated in the following two chapters.

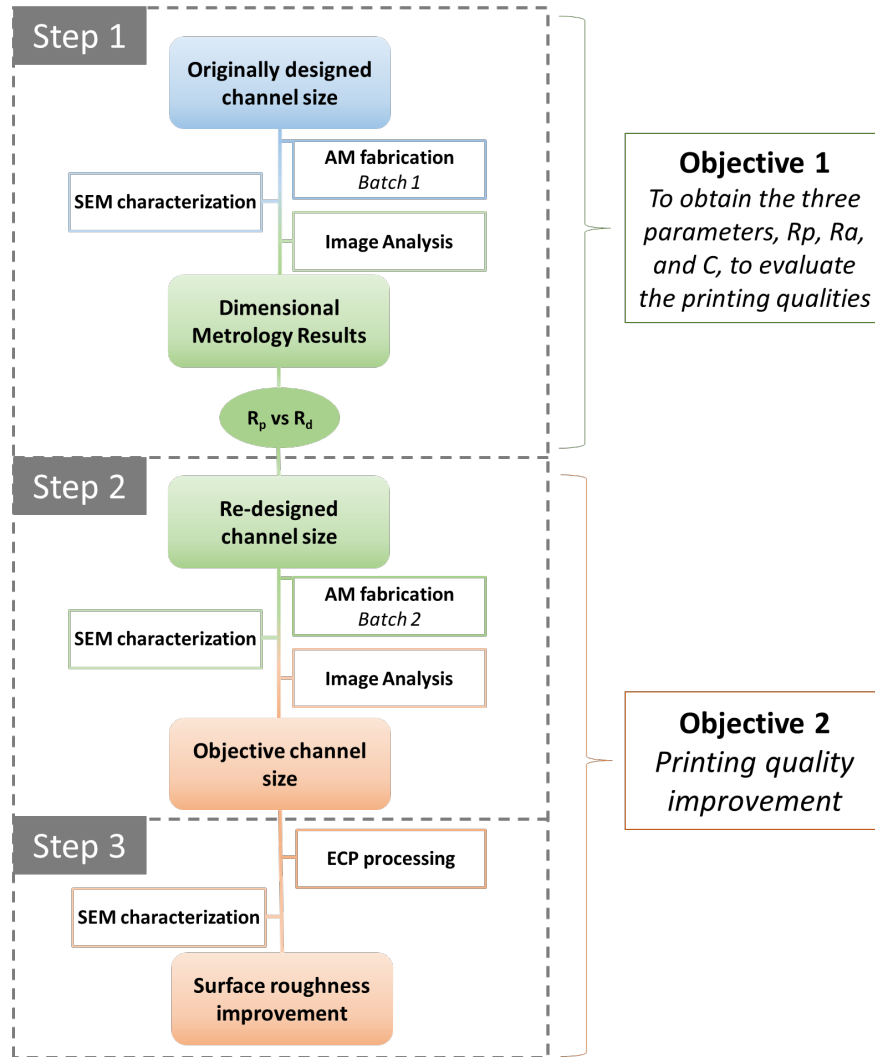


Figure 1.8 Overview of the task of the dimensional characterization and surface improvement

1.3.2 Transpiration Cooling Effectiveness Investigations

To evaluate the cooling performance of the AM transpiration cooling structures, the transpiration cooling effectiveness was investigated using a steady-state IR thermography in this study as mentioned in Section 1.2.3. Four transpiration structures, straight round microchannel structure, compact sphere packing porous media, woven wire matrix structure, and blood-vessel microchannel structure were designed and fabricated using the DMLS technique for this conjugate

heat transfer investigation as shown in Fig. 1.9. One advanced film cooling design, the laidback fan-shaped film cooling structure (Fig. 1.9 (e)), was also fabricated using DMLS as a baseline case for the cooling evaluation. In addition to various cooling passage designs, more straight hole specimens were investigated with different channel sizes ($D = 300 \mu\text{m}$, $400 \mu\text{m}$, $500 \mu\text{m}$) and hole pitches ($P = 1.5D$, $2D$, $3D$) to assess the effects of different geometric parameters along with porosities. The work details in this task will be introduced in Chapter 4.

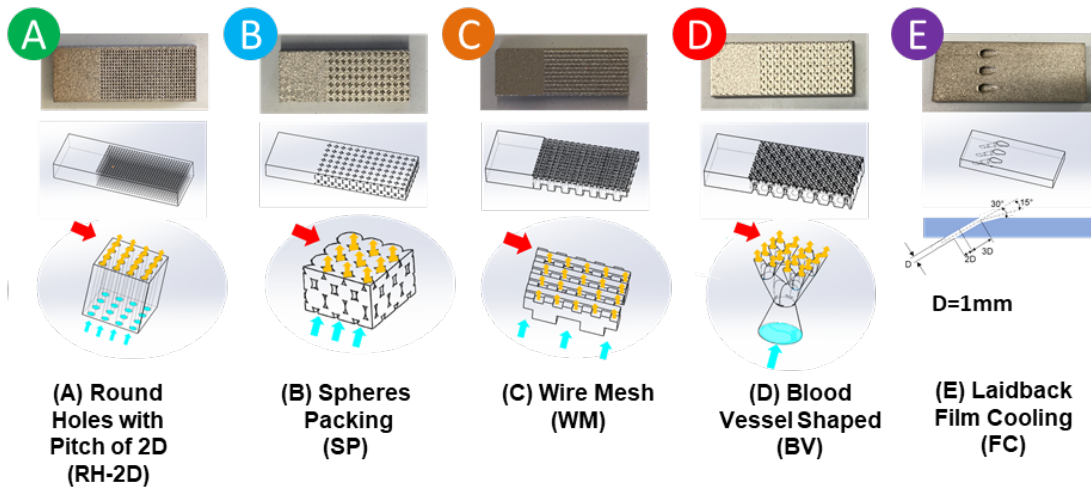


Figure 1.9 Geometric designs for transpiration cooling and film cooling structures

1.3.3 Heat Transfer Coefficient Investigations

The main purpose of this task is to develop a technique to measure the heat transfer coefficient distributions at the target surfaces of transpiration cooling specimens. As mentioned above, the theoretical fundamentals of the transient heat transfer tests fail for the transpiration cooling structures, while the difficulties of the steady-state tests lie on the engineering side: the fabrication, alignment, and attachment of the foil/tape heater without blocking numerous outlets. In this task, a micro-lithography technique was employed to deposit the surface heater directly on top of the transpiration cooling target surface. The heater coil pattern was designed based on the

distribution of the ejection holes at the interested surface to provide uniform and stable heat flux during the steady-state tests. After the surface heater fabrication, the steady-state wind tunnel tests were conducted to obtain the heat transfer coefficient distributions at the target surface. Chapter 5 will demonstrate the HTC investigation work in detail.

1.3.4 Machine Learning Modeling to Predict Cooling Performance

The DMLS additive manufacturing produces microchannels with higher channel size variations than traditional manufacturing, such as laser cutting or wire cutting. Such variations in transpiration cooling structures lead to different thermo-fluid characteristics (wall friction, vortex interaction, turbulence intensity, etc.) and possible blockages of coolant passages, which would impact the cooling performance significantly, as shown in Fig. 1.10. In this task, a neural network model was developed to predict the cooling performance based on channel size distributions and possible related blockage. The input channel size distribution was from the metrology results from Task 1.3.1, while the output images were overall cooling effectiveness distributions. The training data was obtained from high-fidelity CFD simulations. This work will be illustrated in Chapter 6.

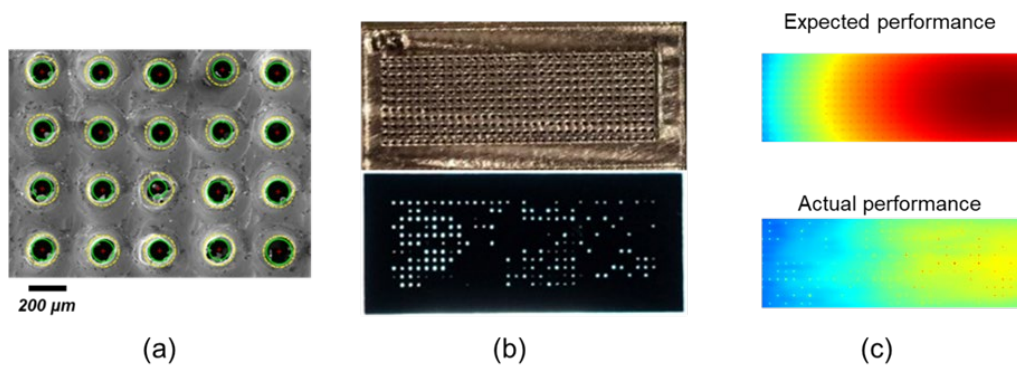


Figure 1.10 The impact of the channel size variations on the cooling performance: (a) SEM photo of various channel sizes; (b) Possible blockage caused by the AM fabrication; (c) Cooling efficiency reduction by the clogging issues

2.0 Dimensional Characterization of AM Microchannels

The first task in this dissertation is to characterize the dimensional geometries of the transpiration cooling channels made by the DMLS technique. In order to evaluate the printing qualities of the microchannels, three parameters, the averaged as-printed channel size, the arithmetical mean deviations of the channel profile, and circularity tolerance were investigated by SEM characterization and the image segmentation technique. It is important to note that while geometric designs play an essential role in generating coupons with desirable qualities, changing materials or machines will create very different parts in terms of dimension, density, microstructure, and surface characteristics. Therefore, the metallic samples presented in this work are all fabricated with the same material (IN 718) and unchanged printing process parameters in the same AM system (EOS M290). In this chapter, the methodology, results and discussions of this presented metrology are described in detail. Part of the results in this chapter has been published by Min et al.[120].

2.1 Methodology

2.1.1 Specimen Designs and Fabrication

The present work employed the direct metal laser sintering technique to fabricate 9 different types of test specimens with Inconel 718 alloy powder in the EOS M290 additive manufacturing system. The general process DMLS technique consists of three steps, i.e., powder

distribution, laser scanning, and working stage adjustment, to complete a working cycle. The process begins with a layer of metal powder dispersed and leveled in the building chamber by a roller or distributor. A certain area of the powder bed is then heated by the laser scan based on the CAD design. Subsequently, the powder bed in the build chamber is lowered for the refilling and redistribution of a new layer of powder. The CAD-design controlled repetition of such working cycles completes the printing process. Finally, the as-printed coupons are then subject to the supporting material removal process in the MV2400-S electrical discharge machining system and the de-powdering process using compressed air.

In this work, the printing parameters of all test coupons are listed in Table 2.1. Straight holes with three different pitch values ($P = 1.5D$, $P = 2D$, $P = 3D$) were designed and fabricated for the subsequent tests, as shown in Fig. 2.1. For the same pitch value, three channel diameters of 0.3mm, 0.4mm and 0.5mm were printed. Thus, a total of 9 different test specimens were made in this task. The printing direction was along the channel direction.

Table 2.1. Inconel 718 parts build parameters

Parameter	Value
Printing Setting	EOS_DirectPart IN 718 Version 102
Laser Spot Size	100 μm
Layer Thickness	40 μm
Powder Size	15-80 μm

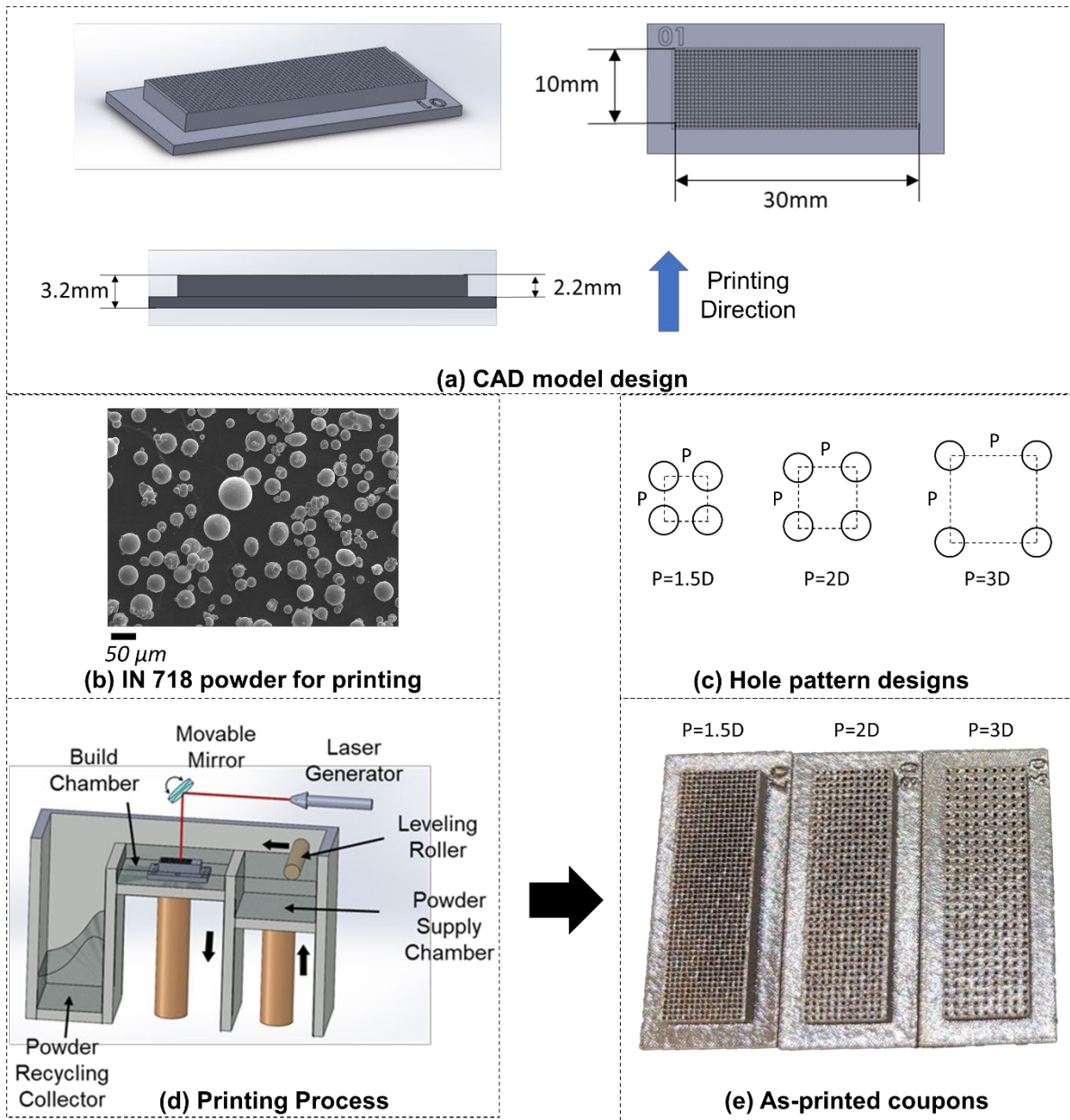


Figure 2.1 Sample dimensional designs and specimen printing, (a) Dimensional design of specimens; (b) Inconel 718 powder for additive manufacturing; (c) Three channel spacing designs; (d) Schematic of DMLS process; (e) As-printed test specimens with radius of 200 μ m and different hole pitches.

2.1.2 SEM Characterization

In this study, each specimen made by DMLS method was cut into three sections in order to capture the inner surface features of the microchannels. The cross-sectional surface of each slice was polished and then imaged by a scanning electron microscopy. Therefore, four surfaces (bottom surface, cut 1 surface, cut 2 surface and top surface) were characterized by SEM for each sample, as shown in Fig. 2.2. For each surface, a total of 70 holes were sampled and imaged for further analysis. Fig. 2.3 exhibits representative SEM micrographs for the cross-sectional view of microchannels on the bottom surface of different hole-size and pitch configurations.

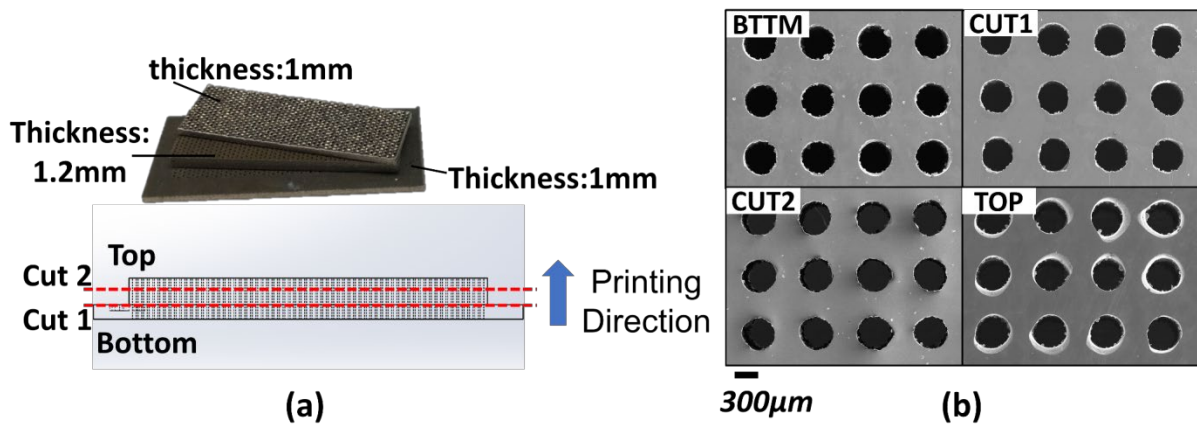


Figure 2.2 Sample slicing for SEM characterizations. (a) cutting positions of the specimen, (b) micrographs of the four cutting surfaces

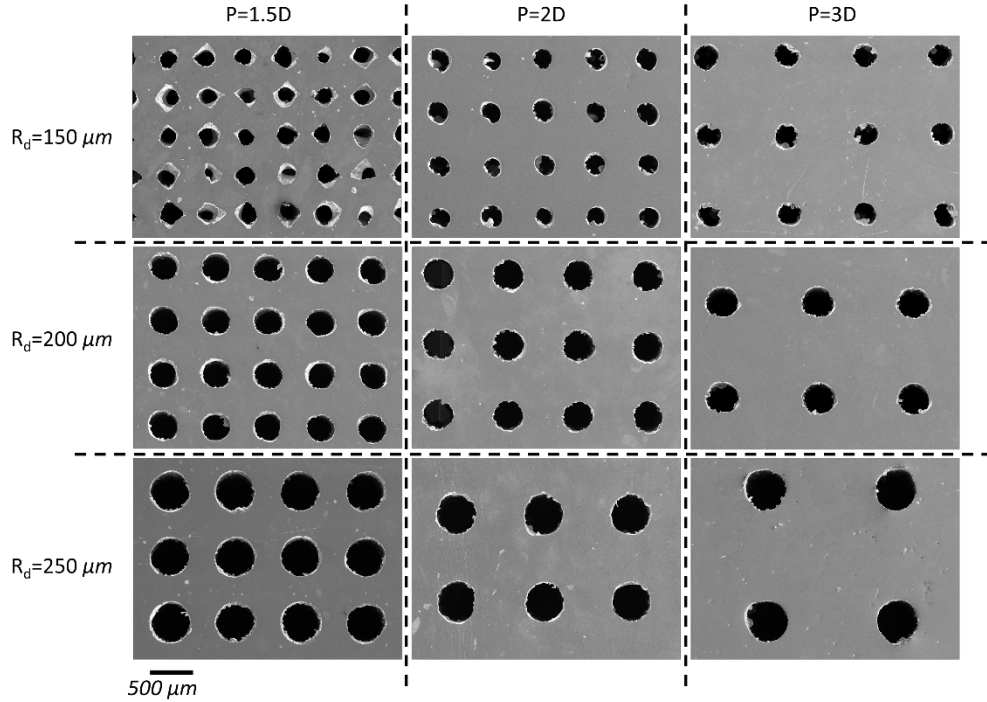


Figure 2.3 Representative SEM graphs for cross-sectional views of microchannels

2.1.3 Image Segmentation and Data Analysis

The subsequent step after obtaining the SEM micrographs of each surface was the image segmentation process to identify surface features, i.e., edge profiles of microchannels. The multi-level Otsu method [99] was used in this study. Otsu's method is the most commonly used algorithm for image segmentation, which selects a global threshold value by maximizing the separability of the foreground and the background in gray scales. The details of Otsu's method are reviewed as follows.

Consider an image containing a total number of N pixels divided into M grayscale levels ($1, 2, 3, \dots, M$), with n_i being the number of pixels at grayscale value i . The possibilities (p) of each intensity level can be calculated as Eq.(2.1).

$$p(i) = \frac{n_i}{N} \quad (2.1)$$

Assume the image is divided into two classes, foreground and background, by a gray value t as the threshold. The class probability of foreground and background is given by

$$w_1(t) = \sum_{i=1}^t p(i) \quad (2.2)$$

$$w_2(t) = \sum_{i=t+1}^M p(i) \quad (2.3)$$

Otsu's method searches for a threshold value T to maximize the inter-class variance σ_b in Eq. (2.4) based on discriminant analysis. The T value can be calculated by an iterative algorithm for this maximization process.

$$\sigma_b^2 = w_1(\mu_1 - \mu_T)^2 + w_2(\mu_2 - \mu_T)^2 \quad (2.4)$$

where μ_1 , μ_2 and μ_T are the mean grayscale values of foreground class, background class, and whole image, respectively, as shown in the following equations.

$$\mu_1(t) = \sum_{i=1}^t ip(i) / w_1 \quad (2.5)$$

$$\mu_2(t) = \sum_{i=t+1}^M ip(i) / w_2 \quad (2.6)$$

$$\mu_T = \sum_{i=1}^M ip(i) \quad (2.7)$$

If the image contains more than two classes of features, a multi-level Otsu method can be applied by a few modifications to the equations mentioned above. If the number of classes of pixels

L defines classes ($C_1, C_2, C_3, \dots, C_L$) by ($L - 1$) thresholds ($T_1, T_2, T_3, \dots, T_{L-1}$), the modified interclass variance in Eq. (2.8) can be described as

$$\sigma_B^2 = \sum_{j=1}^L w_j (\mu_j - \mu_T)^2 \quad (2.8)$$

where

$$w_j = \sum_{i \in C_j} p(i) \quad (2.9)$$

$$\mu_j = \sum_{i \in C_j} ip(i) / w_j \quad (2.10)$$

The iterative algorithm can be applied to Eq. (2.8) for finding the optimal thresholds set ($T_1, T_2, T_3, \dots, T_{L-1}$). Liao et al. [121] proved that the maximization of σ_B^2 in Eq. (2.8) can be replaced by maximizing $\sigma_B'^2$ in Eq. (2.11) as follows to further reduce the number of iterations. This modified equation was used in this study to find a suitable threshold set for image segmentation.

$$\sigma_B'^2 = \sum_{j=1}^L w_j \mu_j^2 \quad (2.11)$$

In this study, the multi-level Otsu method mentioned above was applied for image segmentation for cross-sectional SEM images of the microchannels using an in-house developed MATLAB program. The complete characterization process included SEM micrographs acquirement, thresholds calculation, and image segmentation as shown in Fig. 2.4. Fig. 2.4 (a) shows one example grayscale photo of the cross-sectional view of microchannels. This micrograph was separated into three classes: void area inside the hole, the solid part, and the brightened edge area, based on the two dividing threshold values T_1 and T_2 , which were calculated by multi-level Otsu method from the image histogram (Fig. 2.4 (b)). Subsequently, the image was transformed

into a binary image for hole feature identification, in which the hole shapes were demonstrated by white areas in Fig. 2.4 (c). The coordinates of centroid (C_x , C_y) of each hole (red cross) were calculated based on the numerical integration of coordinates of each white pixel divided by the area of each hole A_k in Eq. (2.12) - (2.13).

$$C_x = \frac{\int_{A_k} x dA}{A_k} \quad (2.12)$$

$$C_y = \frac{\int_{A_k} y dA}{A_k} \quad (2.13)$$

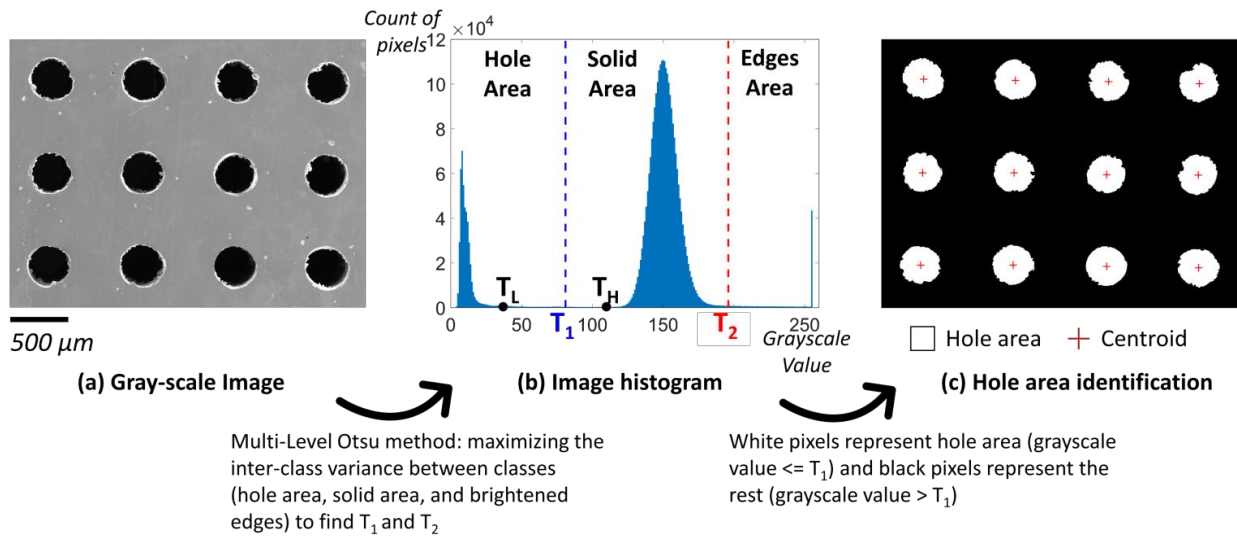


Figure 2.4 Image segmentation process, (a) SEM micrograph for microchannels; (b) Image grayscale histogram and two dividing threshold values T_1 and T_2 ; (c) Identified hole areas using white dots.

Hole profiles from each SEM photo were extracted from the binary image for further analysis. Fig. 2.5 shows two examples of profile extractions. The extracted profile could be plotted in a polar coordinate, in which the origin was set at the centroid of the hole. The relationship between the radius R of each data point on the profile and the corresponding polar coordinate θ

were obtained as shown in Fig. 2.5. The averaged radius of each hole can be calculated from Eq. (2.14) by averaging the radius values of all the data points on the profile (red dots). The commonly used roughness indicator, Ra , is the arithmetic average value of the roughness profile determined from deviations of the averaged value line (blue dash-dot line) given by Eq. (2.15). As mentioned above, 70 holes were selected as the sample pool for each surface, which led to 280 hole profiles for 4 surfaces in total for each specimen. To statistically analyze the dimensional parameters, all profiles from one specimen were put into one plot as shown in Fig. 2.6 with all centroids set to the origin of the coordinate plane.

$$\bar{R}_k = \frac{\int_0^{2\pi} R(\theta) d\theta}{2\pi} = \frac{1}{n} \sum_{i=1}^n R_i \quad (2.14)$$

$$Ra_k = \frac{1}{n} \sum_n |y_i| \quad (2.15)$$

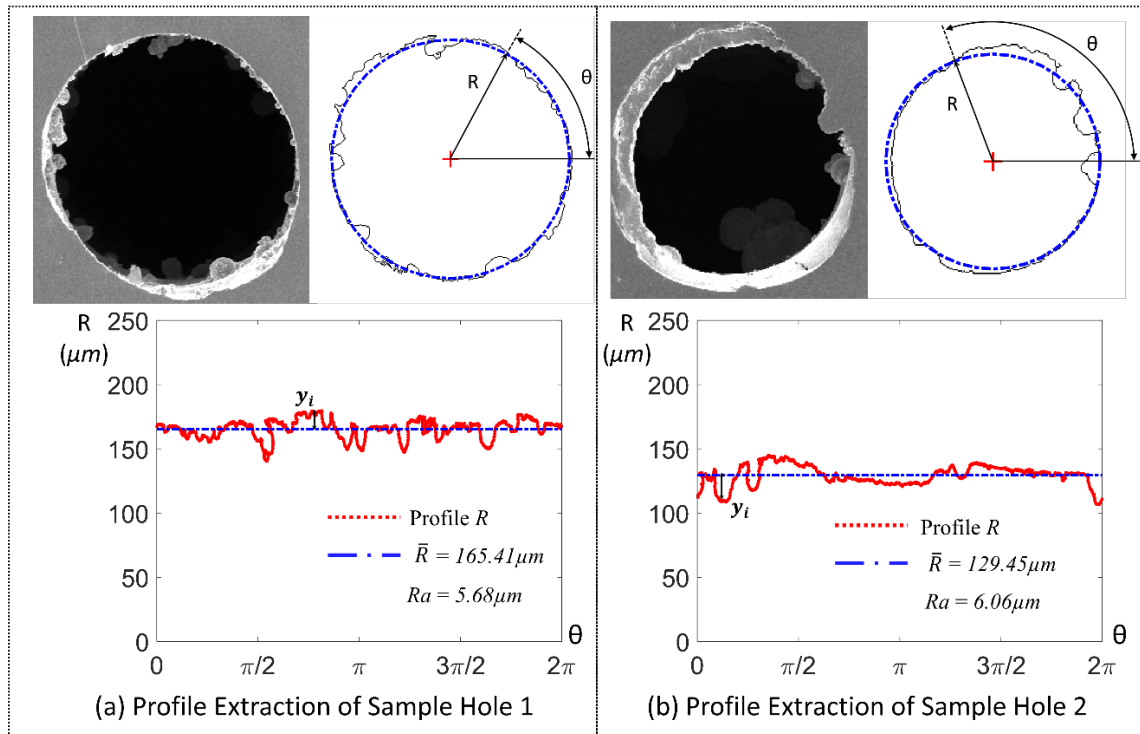


Figure 2.5 Two examples of the profile extraction for two channels with identical designed sizes

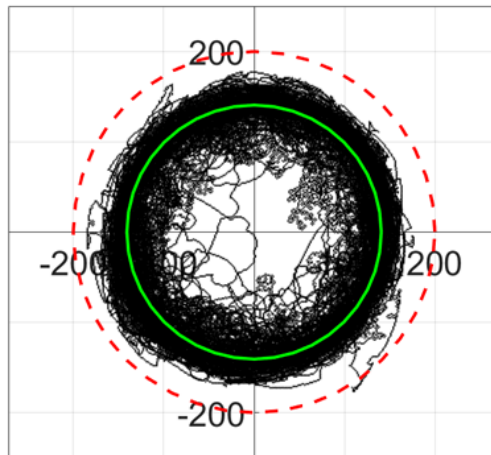


Figure 2.6 Combined profiles of 280 hole profiles

The third parameter, circularity tolerance, is commonly measured by inscribing and circumscribing the data points of a channel profile as shown in Fig. 2.7 (a). In general, the smaller the circularity tolerance is, the rounder the hole profile is. For additively manufactured specimens, as shown in Fig. 2.7 (b), particle attachments sometimes approached or even occupied the centroid of the hole profile, making the radius of the inner circle almost 0. In such cases, circularity tolerance is determined only by the circumcircle. To exclude such extreme cases, in this paper, not all data points in the combined profiles were used to calculate the circularity tolerance value. Instead, only 98% of data points were evaluated in the plot, excluding 1% data points close to the centroid and 1% far from the centroid. The selected 98% of data points are plotted in blue as shown in Fig. 2.7 (c), so the radial width of the blue band represents the C value.

Therefore, in this research, three parameters (the average radius of all the profiles, the arithmetical mean deviation from the average radius, and the circularity tolerance) were used to evaluate the printing quality. The as-printed average radius as close as the objective radius was

preferred. Smaller values of the other two parameters, indicating smaller roughness and rounder channels, were also preferred.

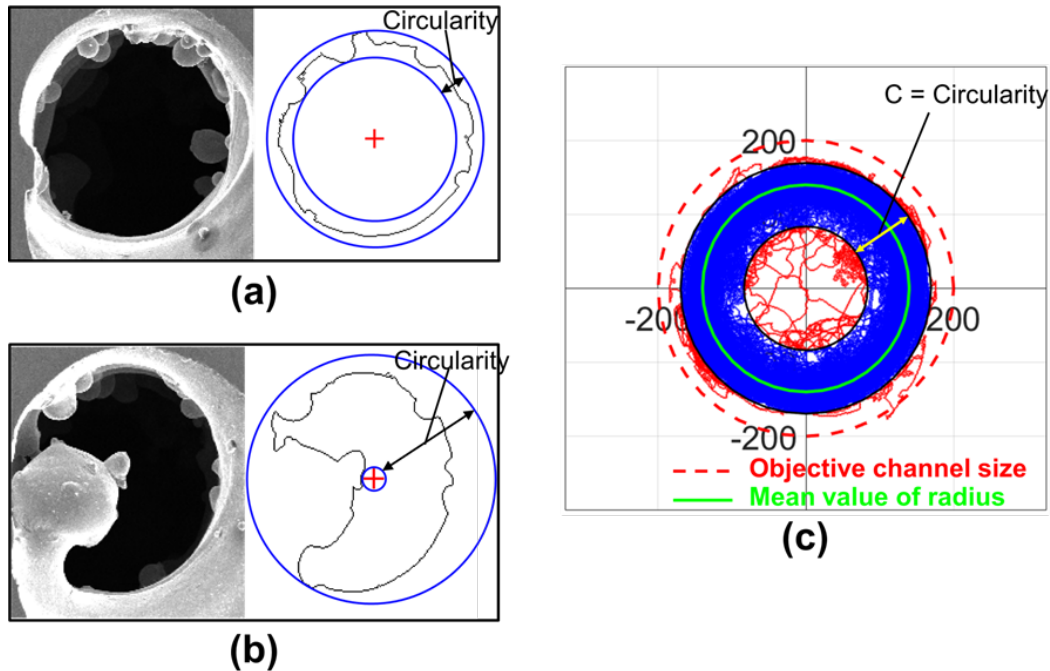


Figure 2.7 Circularity tolerance definitions: (a) the common definition of circularity tolerance, (b) an extreme example of the solid part approaching the centroid, (c) circularity tolerance definition in this study.

2.1.4 Uncertainty Analysis

The uncertainty of image segmentation depends on the accuracy of edge detection, which is determined by the threshold values in the Otsu’s method. In this study, three peaks observed in the image grayscale histogram (Fig. 2.4 (b)) from left to right represent hole area, solid part and brightened edges area respectively. The interested hole area and the remaining part of the image (solid part and brightened edges) were separated based on the grayscale value T_l as shown in Fig. 2.4 (b). Therefore, the grayscale value T_l should be set in the valley part of the histogram between two main peaks: the left peak representing the void phase, and the right one associated with the

solid phase. The possible position of threshold value T_I could be in a grayscale range from the lower bound value T_L to the higher bound value T_H . Pixels with grayscale levels between T_L and T_H could be considered as the uncertain area for image segmentation. This area contains all the possible positions of hole edge pixels. Fig. 2.8 shows such uncertain areas using red highlighted dots. As shown in the middle image of Fig. 2.8, the uncertain areas occupied 4.3% of the hole areas (pixels with gray-scale values between T_L and T_H) identified by Fig. 2.4 (b). Most of such uncertain areas occurred at the edges of the holes, while a small number of them were located in the solid part. Four subplots were made for closer observations of such uncertain areas near four edges of the holes as shown in side-figures of Fig. 2.8. Each subplot contains two parts: the left part is an enlarged photograph of a hole, and the right part is an image covering the same area as the left one with only the uncertain area highlighted using red dots. By comparing the two parts, the location of the uncertain areas could be identified from the original photos. Those subplots show that most of the uncertain areas appear on the interior channel walls (perpendicular to the sliced surfaces) inside the holes. As shown in the middle picture of Fig. 2.8, most uncertain areas (red dots) were not located on the sliced surfaces; instead, they appeared inside the channels. As a result, the areas should be considered as the interior area of the holes on the sliced surface. In this image segmentation method, the interior areas of the holes were defined as all pixels with a grayscale value lower than T_I . Therefore, pixels with values from T_L to T_I should not be considered as uncertainty. The uncertain area could be further narrowed down to pixels with grayscale values from T_I to the higher bound value T_H . The ratio of the narrowed uncertain area to the hole area in Fig. 2.8 was 1.6%. Thus, the uncertainty of the identified hole area for Fig. 2.8 was in a range of 1.6% - 4.3%. In this study, the overall uncertain area was determined by all pixels with grayscale values between T_L and T_H and the narrowed uncertain area was defined by all the pixels with

grayscale values between T_L and T_H for each photograph. The ratios of the overall uncertain areas to the identified hole areas for all the images were less than 4.8%, and the ratios of the narrowed uncertain areas to the hole areas were all smaller than 1.8%. These two small values represented a low level of uncertainty for hole area identifications, demonstrating the reliability of the multi-level Otsu method for image segmentation.

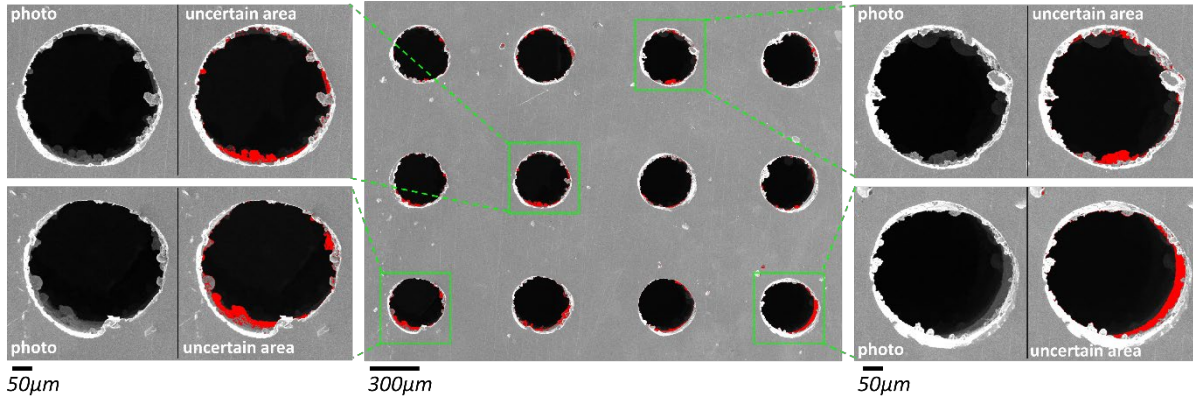


Figure 2.8 Uncertain area (red area) analysis of the image segmentation technique

2.2 Results and Discussions

Figure 2.9 shows the comparison between the mean radiuses of different surfaces in this study. The red, green, and blue bars represent the mean radius values of the as-printed samples with three different designed radius of $150\mu m$, $200\mu m$, and $250\mu m$, respectively. The ratio (R/R_d) of the as-printed radius R to the designed radius R_d was demonstrated by markers in different colors (red for the designed radius of $150\mu m$, green for $200\mu m$, and blue for $250\mu m$), and shapes (circles for hole pitch value of 1.5D, triangles for 2D, and squares for 3D). The values of R/R_d represented by such markers could be read from the secondary y-axis on the right-hand side. The error bars of the radius data represent the averaged values of arithmetical mean deviations, R_a .

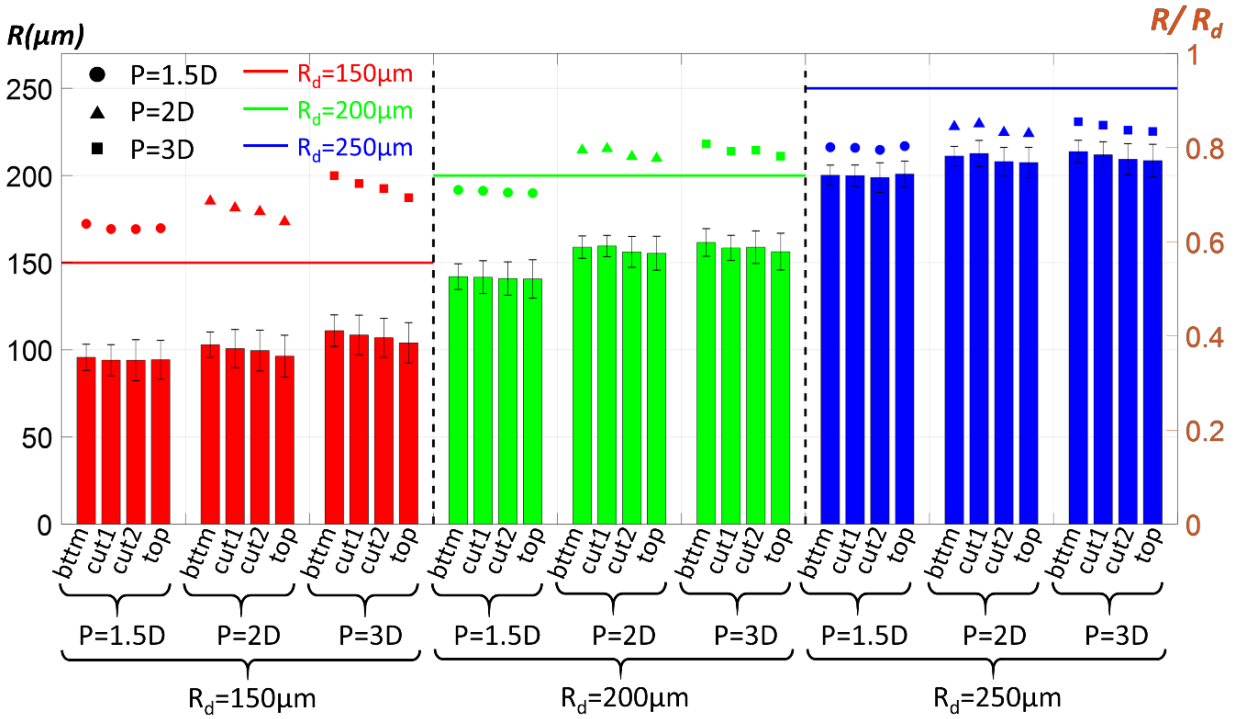


Figure 2.9 Comparison of the mean radius of different hole configurations

Three major conclusions can be drawn from the results in Fig. 2.9. First, the ratio of the as-produced channel size to the designed value R/R_d increased as the designed radius increased. The average value of R/R_d was around 0.65 for specimens with a designed radius of $150\mu\text{m}$, while the value increased to higher than 0.8 for coupons of $250\mu\text{m}$. These ratios demonstrated that the size offset from design to product was significant for additively manufactured microchannels, especially when the feature size was small and close to the laser spot size. The second tendency observed from the figure is that larger hole pitch increases the ratio R/R_d . It was possibly because the distance between contour laser scans of adjacent holes increased as the hole pitch increased, reducing the interactions between the molten pools caused by the adjacent contour scans. As a result, more distant and cooler molten pools at the hole edges reduced the amount of the sintered powders at the edge, producing larger hole areas in each layer. Third, results indicated that the

opening of the channel to form a hole reduced slightly from the bottom surface to the top. In the DMLS process, the part was built layer by layer from bottom to top. Unwanted powders sintered at the channel edges in the previous layer could transfer heat to the subsequent layer, hence sintering more loose powders to the feature edges. Such propagation of powder particle attachments may cause the reduction of channel size from bottom to top.

Figure 2.10 shows a comparison of the values of Ra between different hole configurations. Similar to Fig. 2.9, the bar chart demonstrates the absolute values of Ra , and the markers represent the relative roughness using ratio values of Ra/R . As indicated in the figure, all roughness values were smaller than 15% of the as-produced channel radius. Also, the Ra values decreased as the designed channel size increased, which means a larger designed channel size led to a smoother channel surface. This decreasing trend of Ra/R combined with the increasing trend of R/R_d along with the increase of the designed channel size showed that the printing quality was enhanced when larger channels were produced. Additionally, channel size reduction caused by the propagation of powder particle attachments discussed above was also demonstrated by the increase of Ra values, which was observed along the printing direction in most of the hole configurations.

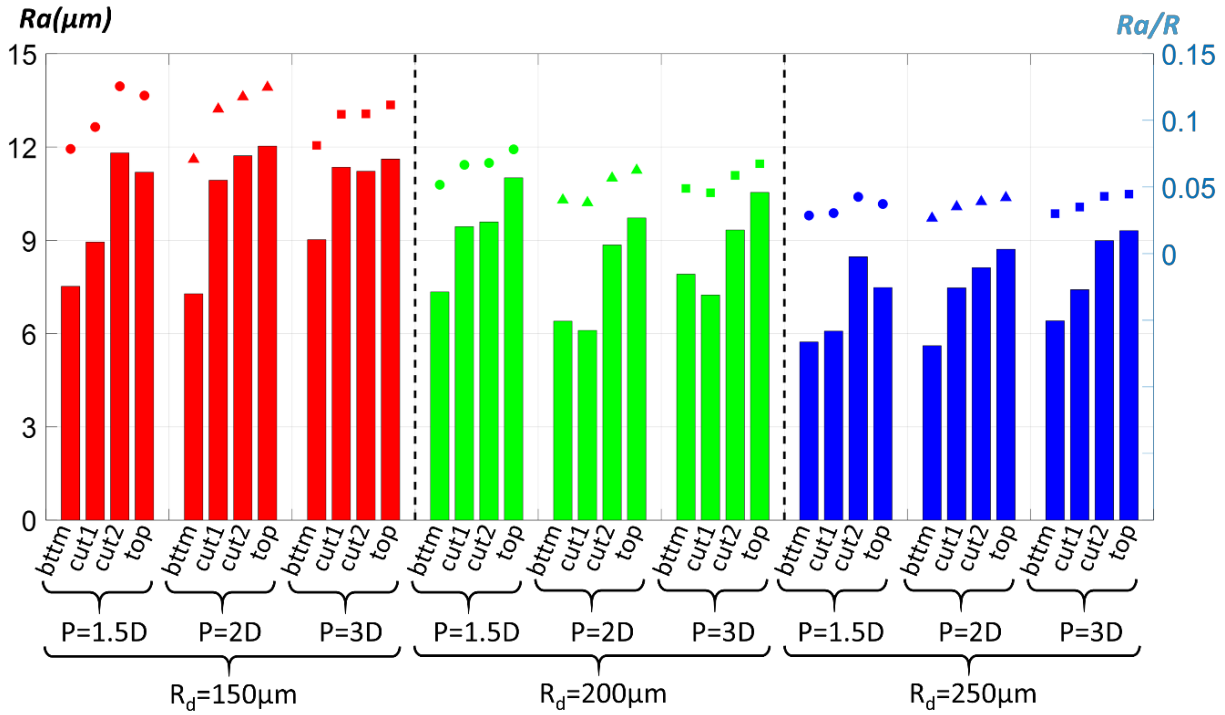


Figure 2.10 Comparison of arithmetical mean deviations of different hole configurations

One of the dimensional metrology task goals, as aforementioned, is to investigate the effect of different hole configurations on the printing qualities of microchannels made by AM. To view the effect of different hole sizes and pitches, the overlapped channel profiles for all 9 hole configurations were displayed in Fig. 2.11. About 98% of data points in this figure were plotted using blue dots and the rest were red to present circularity tolerance. It is obviously seen from the figure that the mean channel radiuses of the as-printed specimens are all smaller than the objective radius. Also, larger designed radiuses lead to larger as-printed channel sizes and thinner annular bands in blue, representing a higher ratio of R_p/R_o and smaller circularity tolerance value C . Results indicated that the printing quality was relatively low when the designed feature size dropped closer to the laser spot size in DMLS fabrication; printing qualities increased as the designed value increased.

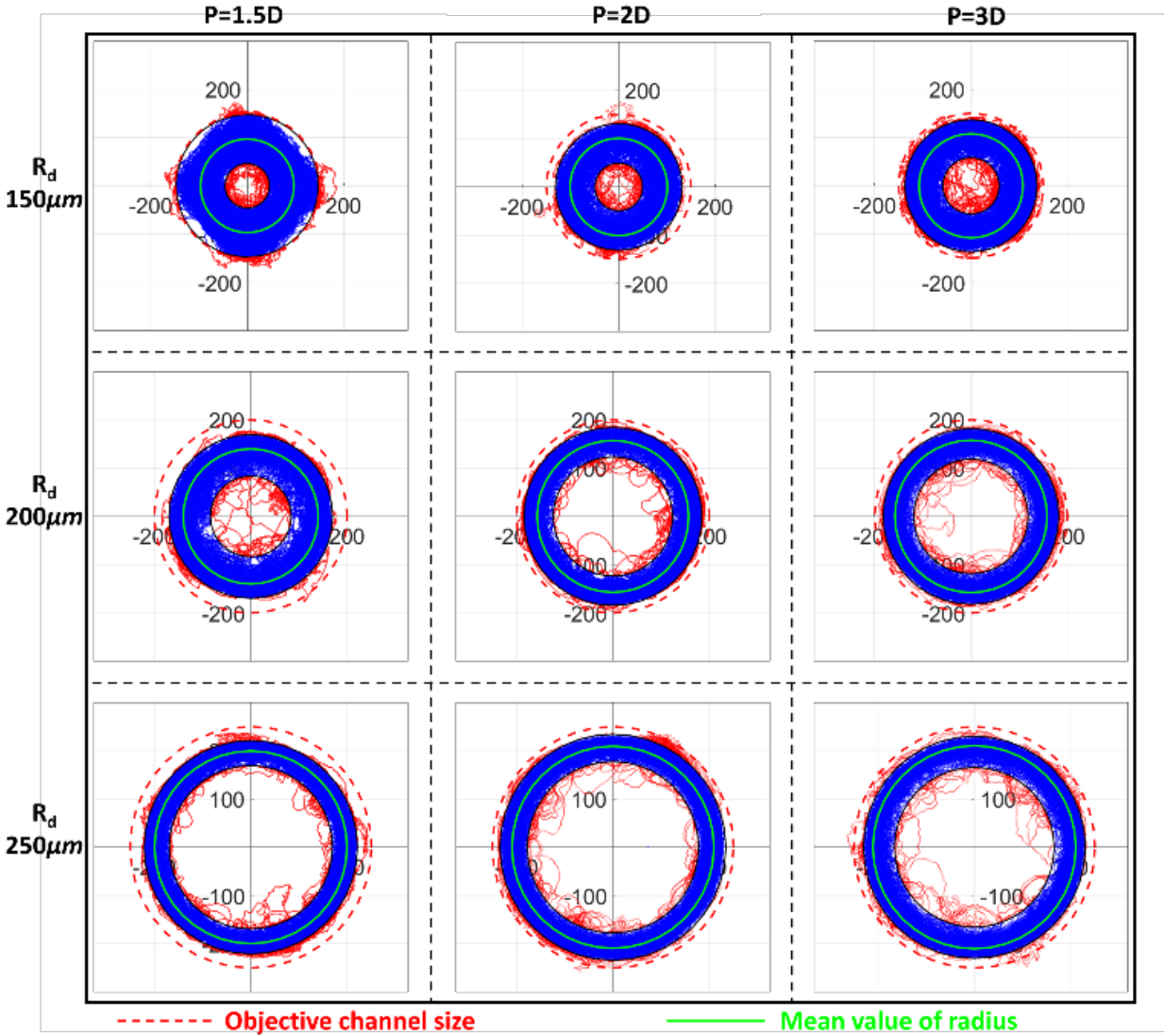


Figure 2.11 Combined profiles of the specimens from the originally designed group

Figure 2.12 shows the quantitative analysis of three parameters, the ratio of the as-printed radius and the objective radius R_p/R_o , the arithmetical mean deviation of all data points Ra , and the circularity tolerance C , respectively, as summarized in Section 2.1.3. The three diagrams indicated that all the ratios of the as-printed radius over the designed radius were less than 1, in the range of 0.65 – 0.85. Also, as the designed radius increased, the ratio of R_p/R_o increased, the roughness value Ra and the value of C decreased. This means the smaller feature size printed by AM, the

larger relative errors were generated due to the laser spot size being close to the feature size. And smaller channel sizes would leave smaller unscanned areas inside channels in each layer of powders, leading to more heat accumulated from the molten pool at the channel edge scanned by laser, sintering more unwanted powders at the edges. Thus, the as-printed channel sizes decreased and roughness increased as the designed channel sizes decreased.

An increased magnitude in hole pitch also improved printing qualities, especially for smaller channel sizes. In general, a larger hole pitch should be able to provide a larger distance between contour laser scans at the hole edges, reducing interactions between adjacent scans that would cause unwanted particle attachments. For samples with a designed channel radius of 200 μm , the impact of hole pitch was observed from pitch of 1.5D to 2D, but less significant from pitch of 2D to 3D. For specimens with a larger designed channel size of 250 μm , the pitch value appeared to be no longer a decisive factor on the values of Ra and C . This is possibly because distances between adjacent channels were sufficiently large to lower the impact from adjacent laser contour scans for channels with a designed radius of 200 μm and pitch of 800 μm (2D). Further increase of the hole pitch showed less impact to improve the surface qualities.

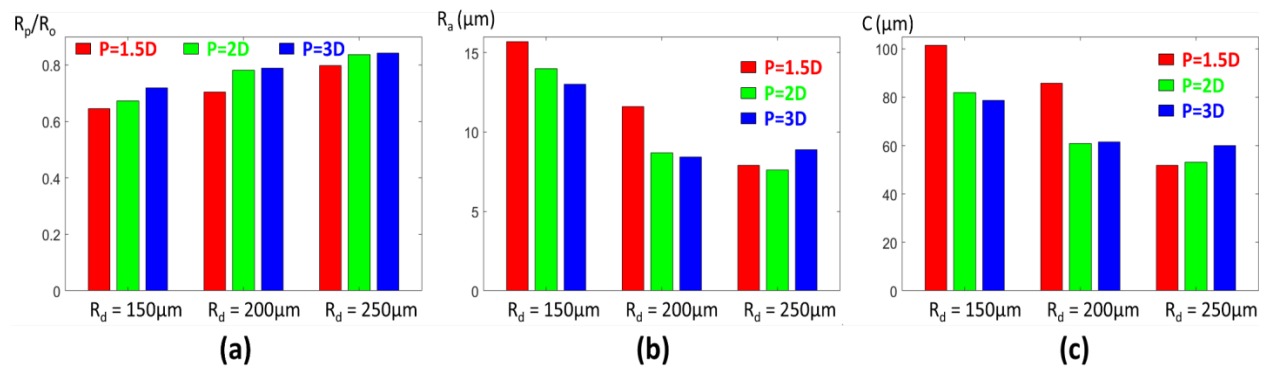


Figure 2.12 Quantitative results of dimensional metrology: (a) the ratio of the as-printed radius and the objective radius R_p/R_o , (b) arithmetical mean deviation of all data points Ra , (c) the circularity tolerance C .

3.0 Surface Improvement of AM Microchannels

The dimensional characterization results in Chapter 2 showed the microchannels made by AM exhibited significant contraction of channel sizes from the designed values. Also, considerable surface roughness was observed due to particle attachments at the inner surface of the microchannels. To address the contraction issue, the CAD-based compensation technique was used in this study to make the cooling channel size close to the objective values, providing the straight-hole transpiration cooling specimens with a desired channel size. In addition, the electrochemical polishing method was performed on a redesigned specimen to improve the surface roughness at inner surfaces. This two-step surface improvement work will be introduced in this chapter. This work has been published by Min et al. [122].

3.1 CAD-Based Compensation for Sample Redesign

3.1.1 Methodology

In Section 2.2, the dimensional characterization results demonstrated that a size contraction occurred from the designed channel diameter to the as-produced channel size during the AM printing process, as shown in Fig. 2.11. One viable approach for the accurate control of channel size is going through compensation of the product design to offset the shape deformation. The prevalent method in traditional manufacturing of determining geometry compensation is finding a compensation factor from the shrinkage study in casting and injection molding [123]. This method

was employed by Pyka et al. [124] to compensate for the systematic offset of the additively manufactured lattice structures. Huang et al. [125] established an analytical model to calculate a set of compensation factors for different sections in a part made by AM. In order to apply this CAD-based compensation method in this study to make the as-printed channel size approach to the designed values, the correlations between the two values were required. Figure 3.1 shows the relationship of the as-produced mean radius and the design value obtained from the SEM characterization in Chapter 2. It was observed that for each hole pitch, a linear correlation could be realized between the designed and the printed channel size. Therefore, based on the correlations, the redesigned channel sizes for nine different objective hole configurations could be calculated, as shown in Table 3.1.

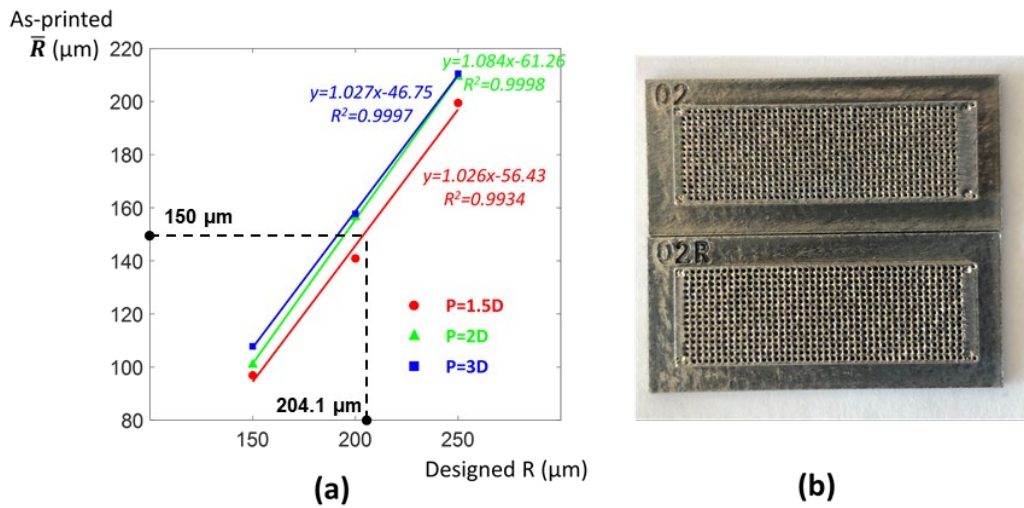


Figure 3.1 CAD-based compensation: (a) correlation between as-produced channel size and designed values and (b) comparison of originally designed sample and redesigned sample

Table 3.1 Redesigned channel sizes

Objective Radius	P = 1.5D	P = 2D	P = 3D
150 μm	204.1 μm	194.9 μm	191.5 μm
200 μm	252.9 μm	241.0 μm	240.2 μm
250 μm	301.6 μm	287.1 μm	288.9 μm

3.1.2 CAD-Based Compensation Results

The redesigned specimens were printed using larger designed hole sizes in Table 3.1, then characterized by SEM images at both top and bottom surfaces. The cross-sectional micrographs of the originally designed samples and the redesigned ones are presented in Fig. 3.2. It can be seen from the figures that the redesigned holes are getting rounder and larger, making the hole profiles get closer to the objective channel profiles, which are the green circles. Fig. 3.3 shows the comparison of the overlapped hole profiles of the two groups for all hole configurations. Compared to the originally designed group, we can see that the averaged as-printed channel sizes get closer to the objective values, and the width of the blue bands are smaller, which means the circularity tolerances are smaller. This improvement of the surface qualities of the re-printed samples can be observed from the quantitative analysis as well. Fig. 3.4 compared the three parameters, R_p/R_o , Ra , and C in the redesigned group and the originally designed group. The R_p/R_o ratios are closer to 1 in the redesigned group, showing that the as-printed channel sizes are much closer to the objective values. Also, all the redesigned specimens have smaller roughness value Ra and smaller circularity tolerance value C , which represent smoother inner surface and rounder hole shape. It can be concluded that the printing quality was improved by the CAD-based compensation to redesign the samples.

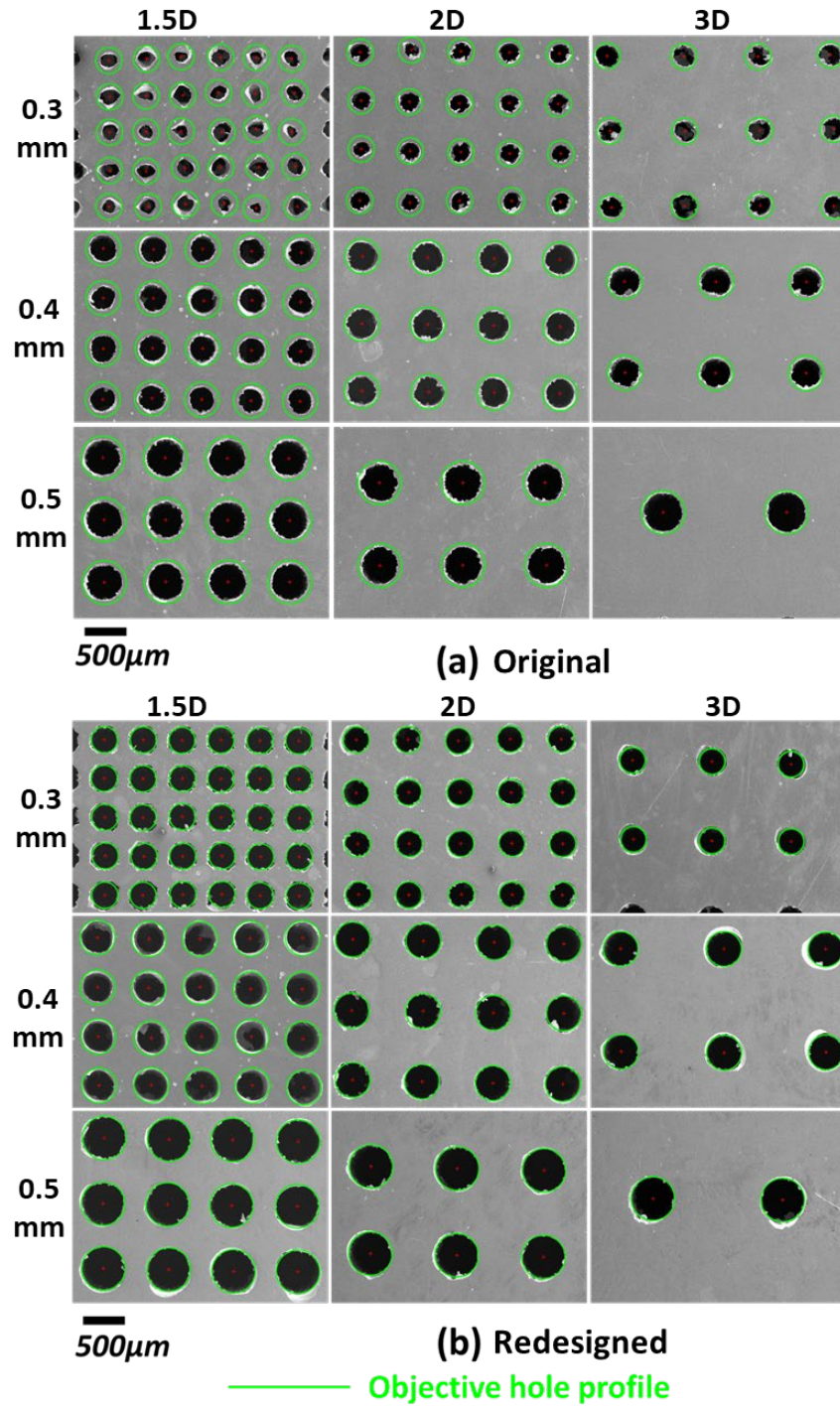


Figure 3.2 Micrograph comparison between (a) the originally designed group, (b) the redesigned group

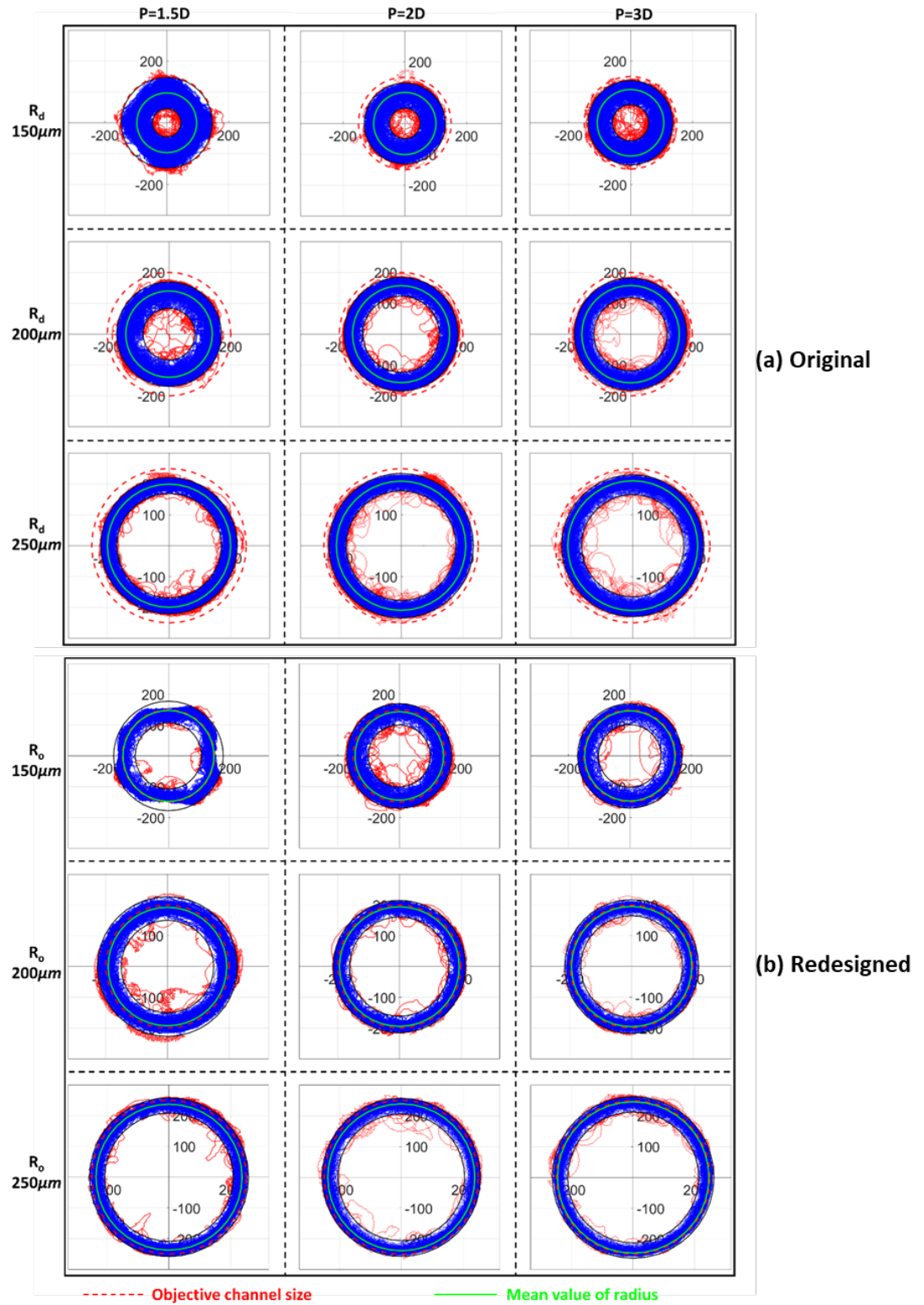


Figure 3.3 Combined profiles comparison

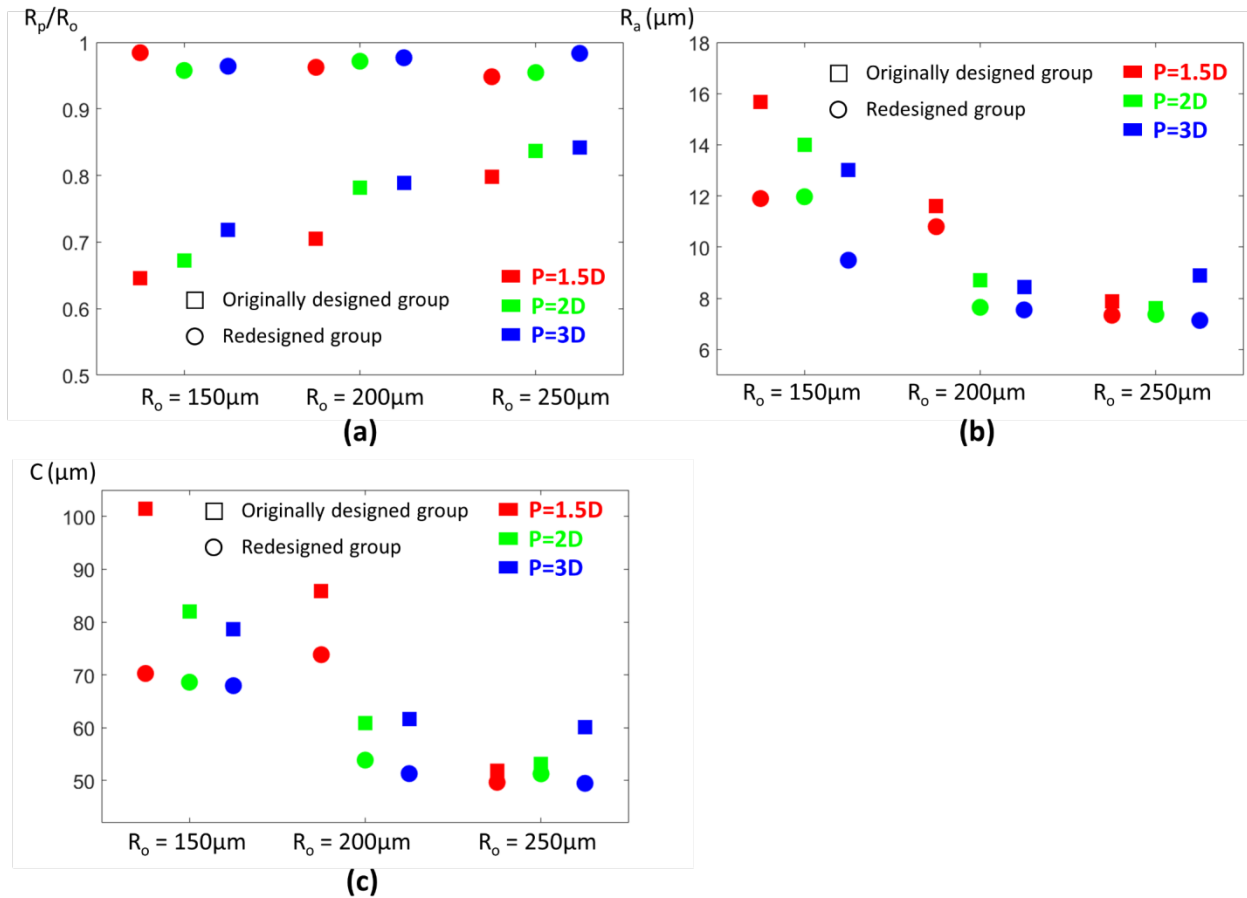


Figure 3.4 Quantitative results of dimensional metrology of both two groups. (a) the ratio of the as-printed radius and the objective radius R_p/R_o , (b) the arithmetical mean deviation of all data points R_a , (c) the circularity tolerance C .

3.2 Electrochemical Polishing Process

3.2.1 Methodology

The surface roughness impacts the materials' functional properties in the microchannels, such as frictional behavior, internal convective heat transfer, pressure drop, and turbulence generation, etc. As mentioned above, deformations due to hatch overlaps and particle attachments

exert a significant impact on producing inner surface roughness of the printed microchannels. However, due to the small size and intricate geometries, the traditional surface treatment methods, such as surface machining, mechanical polishing etc., hardly deal with the surface roughness in AM channels. In recent years, electrochemical polishing, also known as electropolishing, has been used for the AM metal parts to reduce surface roughness. In the ECP process, the interested part is immersed in the bath of electrolyte, connecting to the positive wire of a DC power supply, while the negative electrode is attached to the cathode. During the test, the metal surface gets oxidized and dissolved in the electrolyte when the current passes from the anode to the cathode. This method can improve the surface finish regardless of the complex geometries of the AM sample. By adjusting the current intensity, solution composition, test duration, and temperature, the surface finish can be controlled in the ECP process. Baicheng et al. [126] has applied this method to the AM IN 718 tubes with inner diameters of 8mm. Their results showed that the surface roughness decreased from $6.05\mu\text{m}$ to $3.66\mu\text{m}$ after 5 minutes of ECP. Pyka et al. [127] also applied this method to Ti6Al4V open porous structures. The results showed the surface roughness was reduced by more than 40% in 8 minutes of ECP.

With the success of the ECP process on the AM tubes or Titanium, this study utilized this method on the additively manufactured microchannels. The schematic view of the ECP experiment setup is presented in Fig. 3.5. The ECP process was performed for the redesigned specimen with an objective channel radius of $150\mu\text{m}$ and pitch of 3D. In this ECP test, the specimen after CAD compensation with an objective channel radius of $150\mu\text{m}$ and pitch of 3D was selected for the electrochemical polishing test. This sample was selected mainly due to the small designed channel size generating relatively larger surface roughness value based on the characterization results.

Also, the larger hole pitch value could provide a thicker wall between adjacent holes, preventing the acid from penetrating the channel wall to destroy the microchannels.

The IN 718 sample was connected to a copper wire and placed in the center of acid solution as the anode. The electrode was made by an adhesive copper tape on one end of the sample protected by silicone paste to prevent reactions between the acid solution and the copper electrode. Four cylindrical graphite bars were evenly distributed around the sample as the cathode. The electrolyte was prepared by mixing 20% vol. sulphuric acid into absolute methanol. The current density used in the ECP process was $50A/dm^2$, which was calculated based on the total contact area acquired from the CAD model of the sample design. With a stirring bar spinning on the bottom of the beaker at a speed of 200rpm, the sample was entirely immersed in the solution at room temperature for 1 minute. After being polished, the specimen was rinsed by water and ethanol and dried with compressed air. The top and the bottom surfaces were then characterized by SEM and analyzed in the same way as described in Chapter 2.

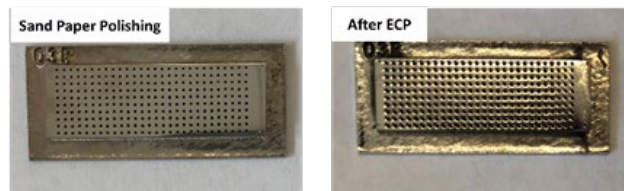
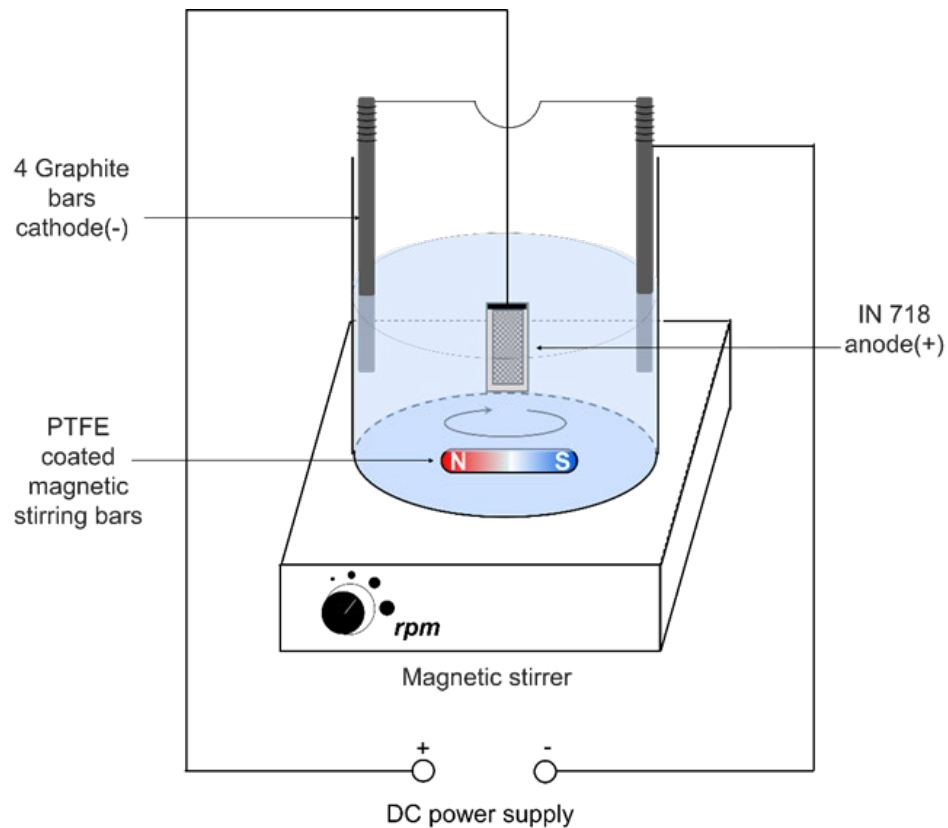


Figure 3.5 ECP test setup and the sample before and after ECP process

3.2.2 Surface Improvement Results

In this study, the redesigned specimen with an objective channel radius of $150\mu\text{m}$ and pitch of 3D was polished by the electrochemical polishing method. Fig. 3.6 shows four example micrographs of the bottom and the top surfaces before and after the ECP process, respectively. The micrographs on the left show the morphology of the hole cross-sections before the ECP process, while the corresponding photos on the right show the same holes afterward. It can be intuitively

concluded from the figure that the microchannels got larger and rounder, and the surface roughness was reduced as well.

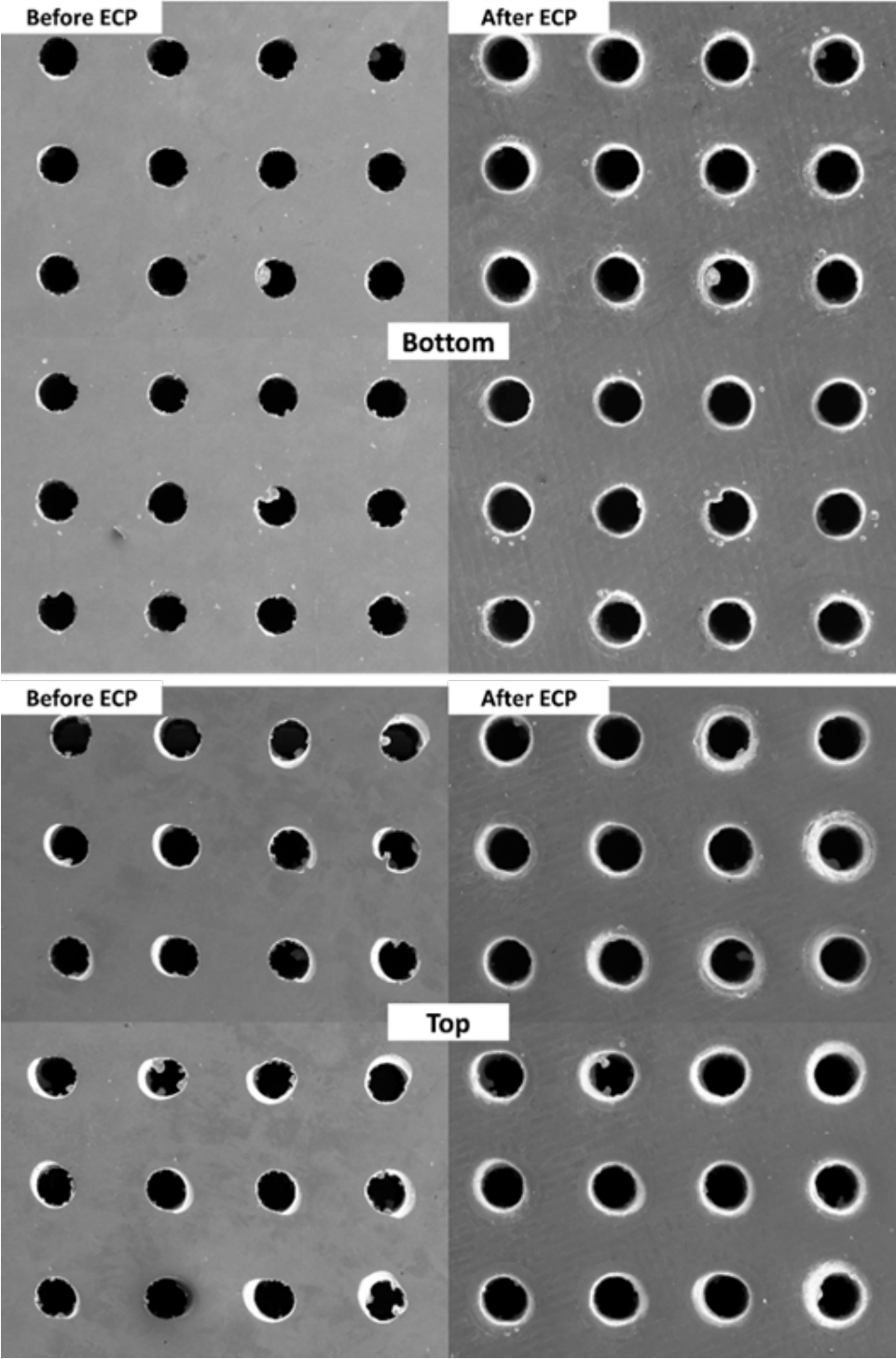


Figure 3.6 SEM photos of two surfaces before and after ECP process

To quantitatively analyze the surface improvement of CAD compensation and the ECP process, the combined channel profiles were presented in Fig. 3.7, demonstrating the specimen with an originally designed channel radius of 150 μm and pitch of 3D, a redesigned channel radius of 191.5 μm , and the same redesigned sample after the ECP process. In the figure, the significant reduction of the width of the blue annular band from the redesigned sample to the sample after ECP is observed, indicating the printing quality was improved greatly by the ECP process. The same conclusion could be made from the statistical analysis in Fig. 3.7 (b). The value of R_p/R_o increased from 0.72 to 1.04 from the originally designed specimen to the sample after ECP, indicating that the produced channel size could be almost the same as the objective size. Both of the other two values, the roughness value Ra and the circularity tolerance value C , dropped after CAD compensation and further down after the ECP process. The Ra and C values of the ECP polished sample decreased more than 50% from the originally designed sample, which means a significant surface quality improvement was achieved by redesigning the channel size and the ECP process.

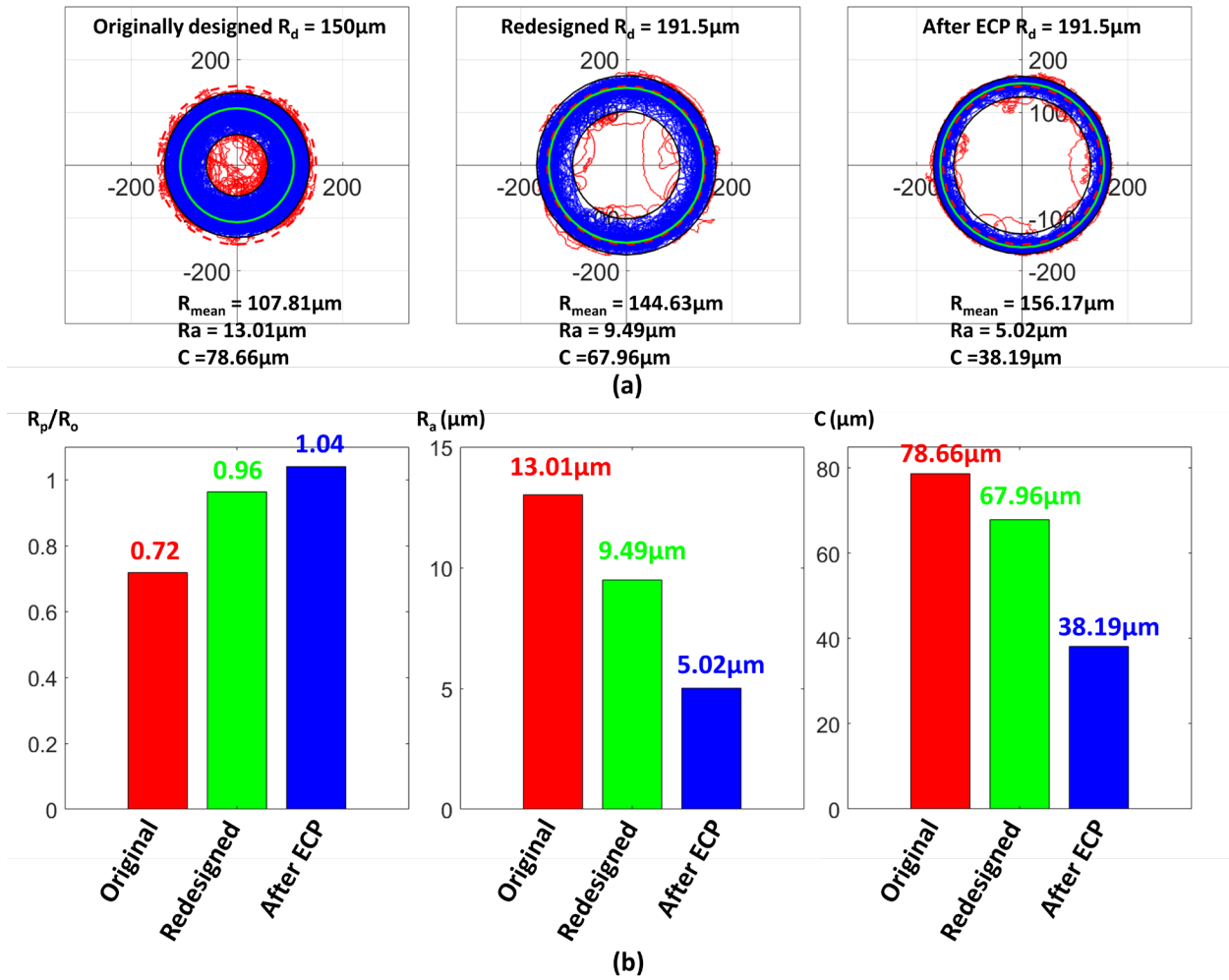


Figure 3.7 Comparison of the originally designed sample, redesigned sample and the sample after ECP. (a) comparison of combined profiles, (b) comparison of three geometric parameters.

4.0 Transpiration Cooling Effectiveness Investigations

Chapter 1 discussed the advantages introduced by the additive manufacturing technique on transpiration cooling structure design and fabrication. In this chapter, several transpiration cooling structures, e.g., straight round microchannel structure, compact sphere packing porous media, woven wire matrix structure, and blood-vessel microchannel structure, were fabricated using the DMLS method and tested in the wind tunnel heat transfer experiments. The cooling performance of these AM-made samples were compared with the state of art film cooling structure made in the same way to show the potential of the transpiration cooling design. Also, with the capability to fabricate the specimens having the as-printed channel size close to the objective values introduced in Chapter 3, the straight-hole transpiration cooling structures with different geometric designs were further investigated in this chapter to evaluate the effects of these design parameters on the cooling performance. The following sections demonstrate the detailed work, part of which has been published in Min et al.'s papers [128, 129].

4.1 Cooling Performance of AM-Made Transpiration and Film Cooling

4.1.1 Methodology

In this study, five different structures of transpiration cooling specimens were designed and fabricated in comparison with a single-row film cooling structure made by the same DMLS method as shown in Fig. 4.1. The cooling passages were built in the IN 718 plate with a dimension of

30mm × 12mm × 3.2mm. The microchannels of the first two transpiration cooling designs (Fig. 4.1 (a) and (b)) were in-line straight round holes with a designed diameter of 0.3mm perforating through the metal plate with different channel spacings. The design idea of spheres packing specimen and wire mesh specimen both came from the traditional porous metal: the structure of spheres packing was similar to the compact powder pack made by high-temperature sintering while the wire mesh structure originated from the wire weaving process. In addition, blood vessel shaped microchannels were designed to simulate the real blood vessels, consisting of numerous tiny subbranches of passages near the outer skin. Fig. 4.2 demonstrates the specific dimensions of the transpiration cooling passages and the corresponding SEM images for the target surfaces. The film cooling structural design came from the state-of-the-art laidback film cooling holes [130] as shown in Fig. 4.2 (f).

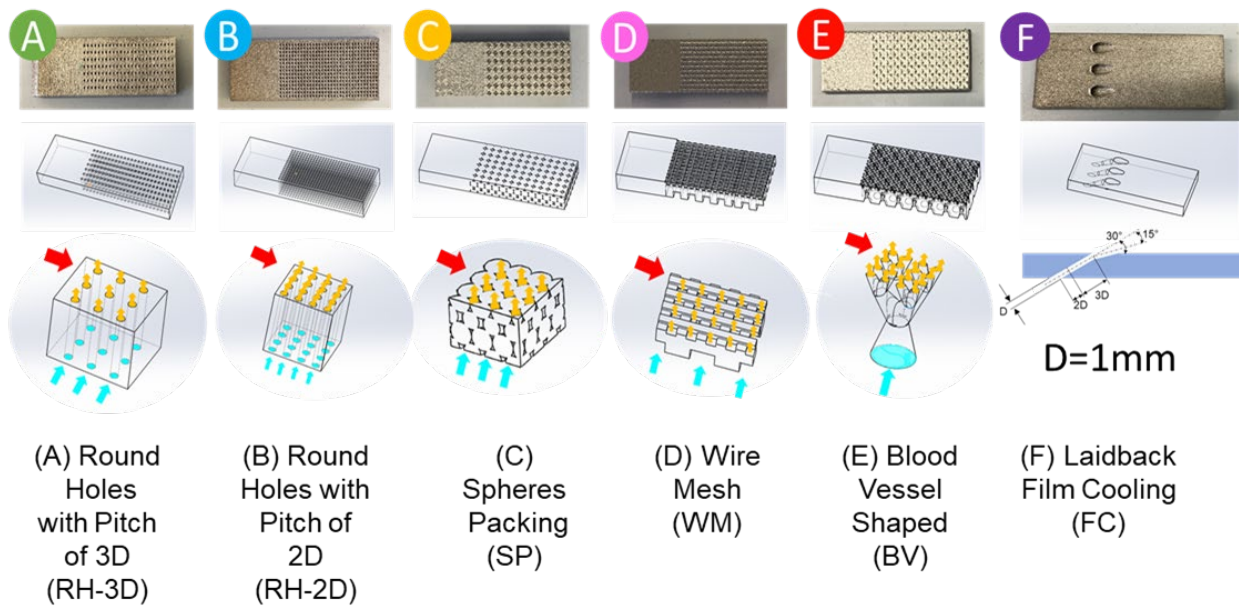


Figure 4.1 Schematics of five transpiration structures and one film cooling design

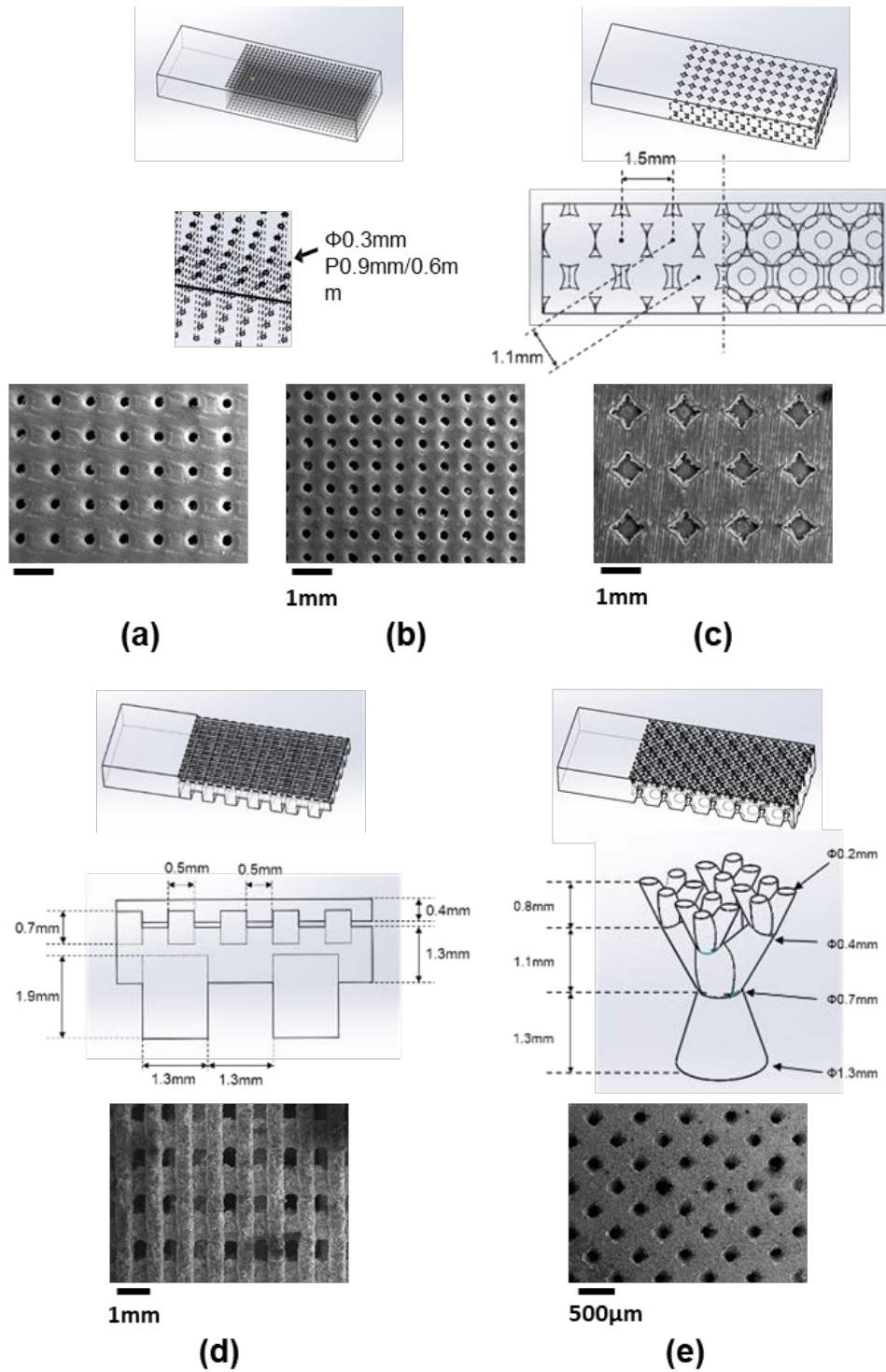


Figure 4.2 Dimensions and SEM micrographs of the transpiration cooling structures: (a) Round Holes with Pitch of 3D; (b) Round Holes with Pitch of 2D; (c) Spheres Packing Design; (d) Wire Mesh Design; (e) Blood Vessel Design

In order to facilitate a rational comparison of the cooling performance among different cooling structures, the identical coolant consumption rate was used to cool the same area of the target surfaces for different test samples. In transpiration cooling, the non-dimensional coolant flow rate, the injection ratio, is defined as:

$$F = \frac{\rho_c v_c}{\rho_g v_g}, v_c = \frac{\dot{m}_c}{\rho_c A_{eff}} \quad (4.1)$$

where ρ_c and ρ_g are densities of coolant flow and mainstream flow, v_c is the average velocity of coolant flow over the area of coolant coverage, v_g is mainstream flow velocity, \dot{m}_c is the coolant mass flow rate, and A_{eff} is the effective cooling area covered by the coolant film as shown in Fig.

4.3.

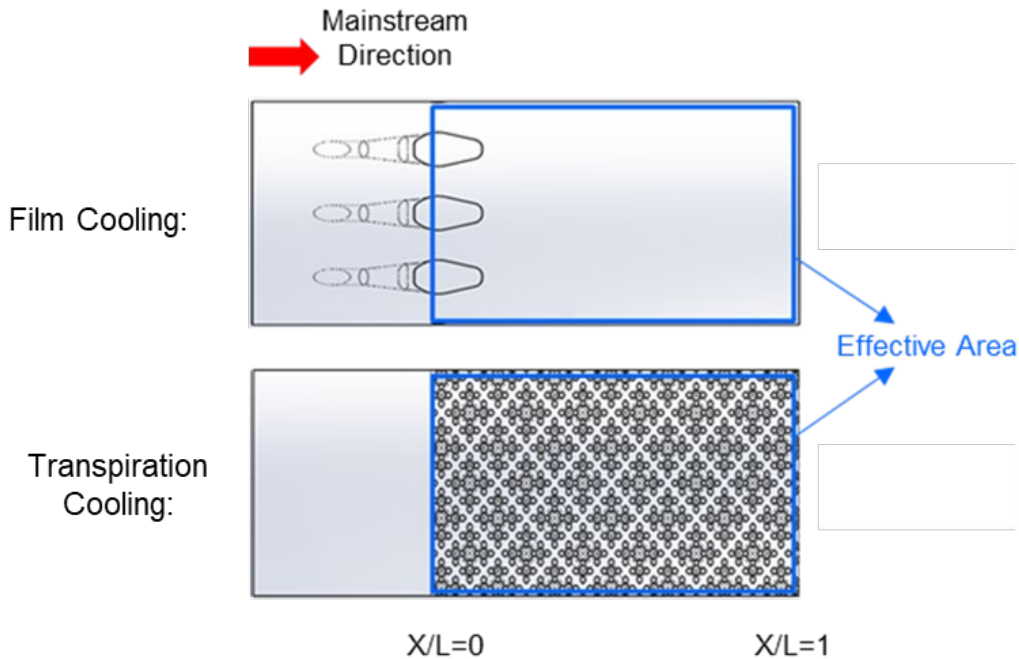


Figure 4.3 Effective coolant covered area

The infrared (IR) imaging technique was employed to capture the wall surface temperature of the test specimens in the present study. Using this method, two surface temperatures, i.e., the

wall temperature with the coolant coverage, and the one without coolant injection, could be obtained under the steady-state flow conditions to calculate the transpiration cooling effectiveness as defined in Eq. (1.9). Three different injection ratios ($F = 1.2\%$, $F = 2.4\%$, and $F = 3.6\%$) of the coolant with room temperature at 21°C were tested for all cooling structures. For each injection ratio, four groups of wall temperatures were recorded under four mainstream temperatures, generating the plot of $(T_{w(M=0)} - T_w)$ vs $(T_{w(M=0)} - T_c)$ as shown in Fig. 4.4. The slope of the curve fitting for each injection ratio represents the local transpiration cooling effectiveness, reducing the uncertainties from a single test.

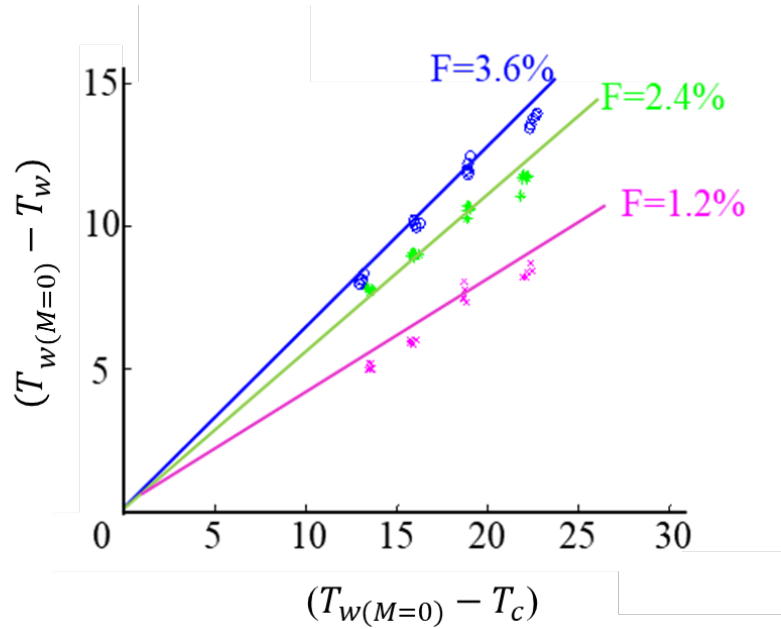
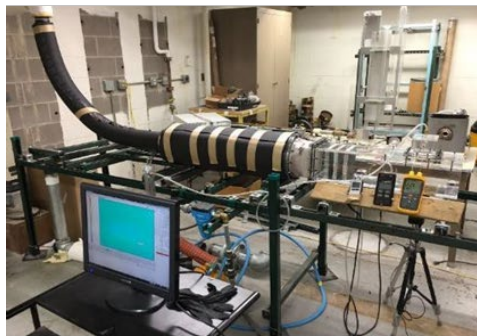
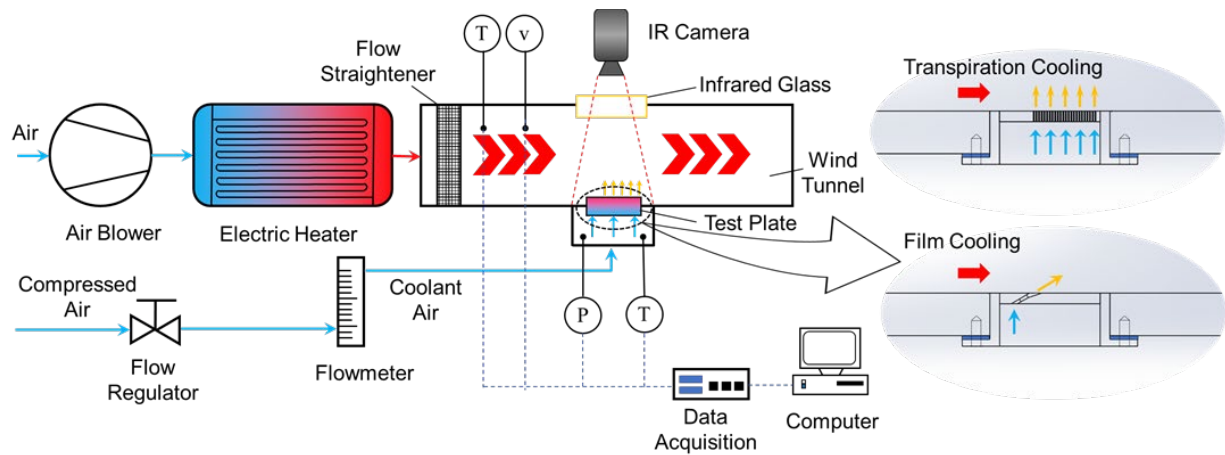


Figure 4.4 Transpiration Cooling Effectiveness Curve Fitting

4.1.2 Experimental Facilities

Figure 4.5 shows the schematic and the photograph of the test rig to investigate the transpiration cooling effectiveness. The mainstream flow was introduced into an electric heater, heated to four different target temperatures (45°C, 50°C, 55°C, 60°C) before entering the square cross-sectional wind tunnel with a dimension of 200mm × 200mm. The heated flow was then directed through a flow straightener and kept a constant velocity at 11m/s ($Re = 98000$) for all test conditions. On the coolant side, cooling air with room temperature (21°C) was supplied from a compressed air source, injecting into the test specimens from the coolant plenum. For each target mainstream temperature, three separate steady-state tests were conducted using different coolant injection ratios ($F = 1.2%$, $F = 2.4%$, and $F = 3.6%$). During each steady-state test, the hot surface temperature of the test plate throughout the experiment was monitored by a FLIR A310 infrared camera. The mainstream and coolant temperatures were measured by K-type thermocouple insertions in the wind tunnel and the coolant plenum. The velocity of the hot stream was calculated based on the Pitot tube readings. The volume flow rates of the coolant were recorded by the Dwyer series RM flowmeter.



Test Conditions:

1. Injection Ratio: $F = 1.2\%; 2.4\%; 3.6\%$
2. Coolant Temperature: $T_c = 21\text{ }^\circ\text{C}$
3. Mainstream Temperature: $T_{gset} = 45, 50, 55, 60\text{ }^\circ\text{C}$
4. Mainstream Velocity: $v_g = 11\text{ m/s}$ ($Re_g = 98,000$)

Figure 4.5 The schematic and photograph of the test rig and the test conditions

4.1.3 IR Camera Calibration

The mechanism of the IR image technique comes from the Stefan-Boltzmann Law of radiation, which describes the correlation between radiation energy and the temperature of a blackbody. However, in the real world, the amount of radiation emitted from the interested object highly depends on the emissivity, which is a value between zero (perfect absorber) and one (blackbody). To accurately measure the emissivity value is difficult because the measurement depends not only on the nature of the surface (material, roughness, surface temperature, etc.) but also on the environment factors (environment temperature, humidity, etc.). Therefore, calibration

tests were required before using the IR thermography technique to capture the target surface temperatures.

The use of IR camera for surface temperature measurement generally results in more accurate readings with higher values of surface emissivity. Thus, all test surfaces were painted black to increase the emissivity after being rinsed with water and ethanol. To calibrate the IR readings, each black painted coupon was installed on the same test rig (Fig. 4.5) without providing any coolant air supply and mainstream flow. A digital controlled hot plate (PMC Dataplate S720) was then installed from the backside of the coupon, touching the coolant side surface to heat the coupon from 21 °C to 65 °C, as shown in Fig. 4.6. During the heating process, the hot plate temperature was set to 35 °C, 45 °C, 55 °C, and 65 °C, respectively, and held for 10 minutes to let the coupon surface temperature reaching the steady state for each given temperature setting. As the metal plate is very thin (3.2mm), the surface temperature approached a nearly homogenous condition after reaching the steady state, making the temperature difference smaller than 0.2 °C all over the sample surface. The nearly isothermal steady-state surface temperatures were measured by four thermocouples attached to the coupon by copper tape at different locations, as shown in Fig. 4.6 (a). The IR camera that was to be calibrated recorded the temperature maps of the top surface for all the four temperature settings. This would lead to a correlation between the IR camera recorded temperature readings and the corresponding thermocouple readings, as shown in Fig. 4.6 (b).

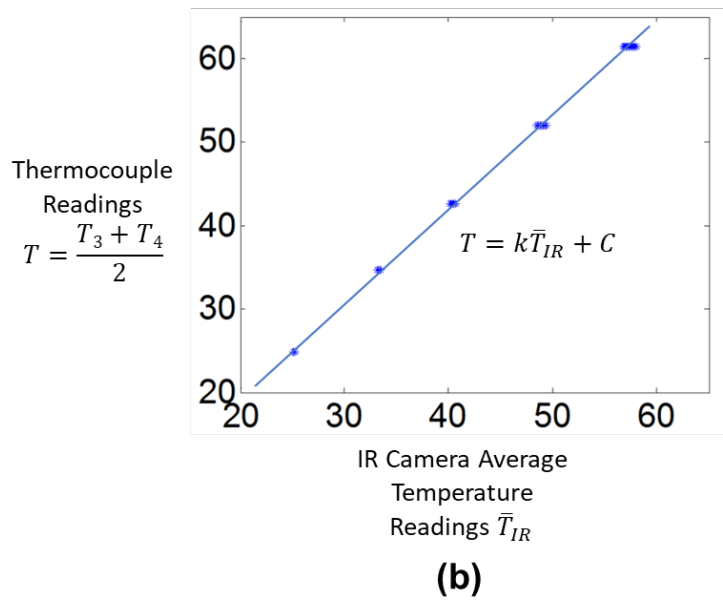
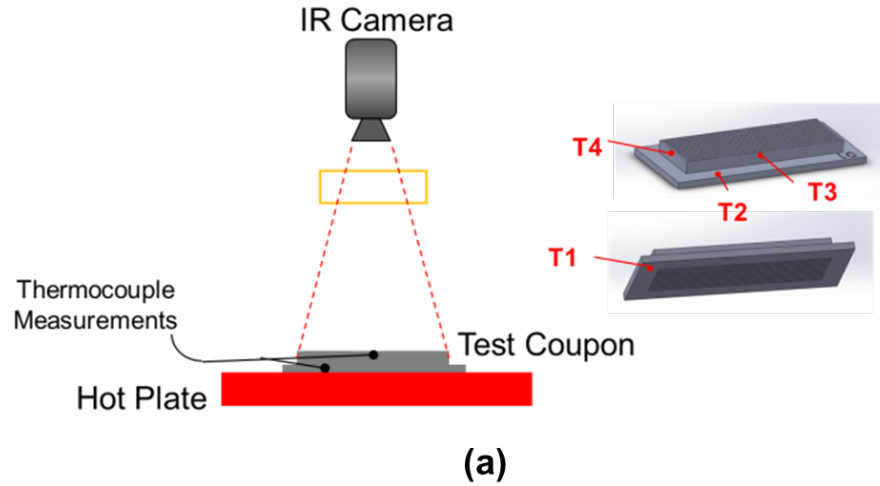


Figure 4.6 IR calibration: (a) Calibration test setup; (b) The calibration curve of one sample

4.1.4 Uncertainty Analysis

The uncertainty of the transpiration cooling effectiveness is determined by the uncertainties of thermocouple and IR readings for the temperature measurements. Based on the theory of uncertainty propagation developed by Kline[131], the uncertainties of the transpiration cooling effectiveness are calculated as

$$\frac{\delta\Phi}{\Phi} = \sqrt{\left(\frac{T_w - T_c}{(T_{w(M=0)} - T_c)^2} \frac{\delta T_{w(M=0)}}{\Phi}\right)^2 + \left(-\frac{1}{T_{w(M=0)} - T_c} \frac{\delta T_w}{\Phi}\right)^2 + \left(\frac{T_{w(M=0)} - T_w}{(T_{w(M=0)} - T_c)^2} \frac{\delta T_c}{\Phi}\right)^2} \quad (4.2)$$

In the present study, the uncertainties of K-type thermocouple readings of the mainstream temperature and coolant temperature were both 0.5K. Uncertainty of wall temperature obtained by IR camera was controlled within 1K after the thermocouple calibration using K-type. Therefore, the total uncertainty of the present cooling effectiveness was estimated in a range of 6.2%, 5.6%, 5.2% and 5.0% for mainstream temperature at 318K, 323K, 328K and 333K, respectively.

4.1.5 Results and Discussions

Shown in Fig. 4.7 are comparative distributions of the transpiration cooling effectiveness, Φ , at the target surfaces of different cooling structures. The color from blue toward red represents the local Φ value from low to high. It can be seen that the transpiration cooling effectiveness in the film covered area increases as the injection ratio increases. With more coolant injection, the effect of the film coverage improved more significantly for transpiration cooling structures than film cooling structures. This difference is possibly caused by the “lift-off” of coolant jets for film cooling at a high injection ratio (3.6%), leaving more hot air entrainment into the wall. In contrast, the coolant of transpiration cooling would have a stronger tendency of attaching closer to the target surface, enhancing the coolant protection of the target surface.

The test plate with blood-vessel-shaped microchannels performed the best among all five transpiration cooling structures, as it renders the highest averaged transpiration cooling effectiveness of 0.57 with an injection ratio of 3.6%, as shown in Fig. 4.8. The complex internal channels of the BV design enhanced the convective heat transfer inside the wall while the numerous outlets at the target surface provided uniform film coverage, both improving the cooling

efficiency significantly. For the same reason, the round-hole transpiration cooling structure with a pitch to diameter ratio of 2 ($P = 2D$), which leads to much more compact cooling channels within the test plate, outperformed the one with a hole spacing of $P = 3D$. The round-hole design of $P = 3D$ showed the lowest effectiveness at all three injection ratios due to simple internal geometry and lowest porosity. At a low injection ratio of 1.2%, the $P = 2D$ round-hole structure had comparable cooling effectiveness with spheres packing and the blood vessel structure. As the injection ratio increased, the higher turbulence intensities generated by the complex internal structure elevated the heat removal capabilities. Therefore, the transpiration cooling with complex internal geometries, including spheres packing, wire matrix mesh, and blood-vessel design, demonstrated better performance than a simply perforated plate at $F=2.4\%$ and $F=3.6\%$.

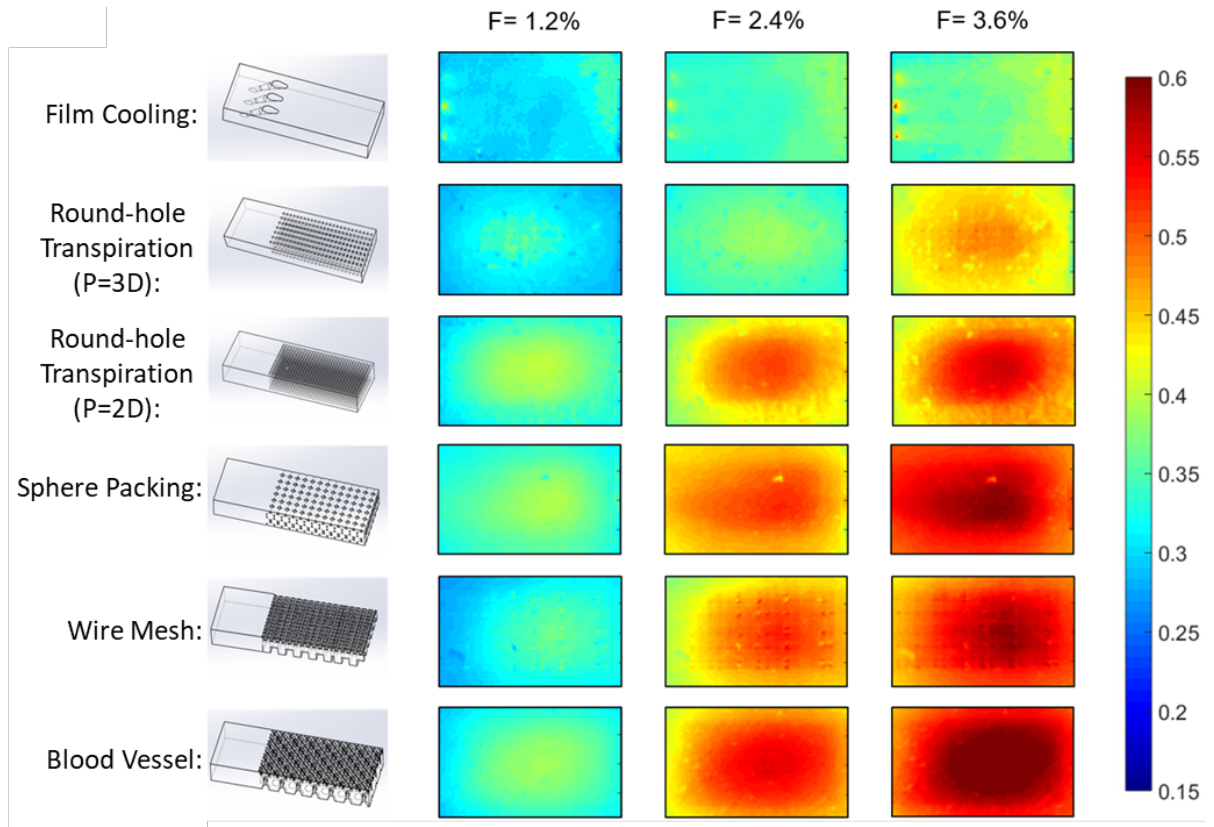


Figure 4.7 Transpiration cooling effectiveness comparison

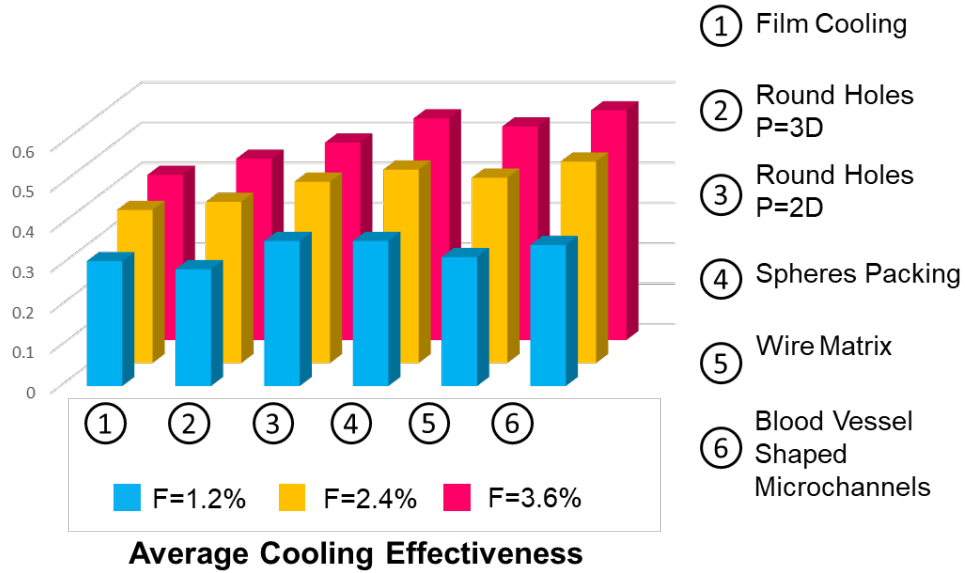


Figure 4.8 The area-averaged transpiration cooling effectiveness comparison

Most of the transpiration cooling studies looked into the impact of porosity on the cooling efficiencies, as mentioned in Section 1.1 and 1.2. A higher porosity of metal plates generally leads to a lower target surface temperature. In this study, the relationship between porosity and transpiration cooling effectiveness is shown in Fig. 4.9 (a). It can be found that the transpiration cooling effectiveness, Φ , is not a monotonically increasing function of the porosity, ε . The wire mesh design with the highest level of porosity among all geometries did not perform the best on the cooling efficiency. One plausible reason is that the opening area of the wire matrix was large, generating low local internal velocity inside the plate. This low-speed flow passed through the wire matrix without much turning and mixing, leading to the low convective heat transfer. These effects resulted in the low values of Φ , which could not be determined simply by porosity.

Another factor observed to the impact of Φ value is the designed internal solid-fluid interface surface area. Fig. 4.9 (b) demonstrates the effect of the designed internal area ratio, which is defined in Eq. (4.3). Here the blood vessel and sphere packing designs has the highest

transpiration cooling effectiveness, benefiting from the enlarged internal wetted surfaces, which significantly enhances the heat removal capabilities in the wall. Although round hole structure with a pitch of $P = 2D$ shows the highest internal solid-fluid ratio, the cooling effectiveness is not comparable to the BV and SP design due to the lower level of mixing generated by the simple straight channels.

$$R_{internal} = \frac{A_{int}}{A_{eff}} \quad (4.3)$$

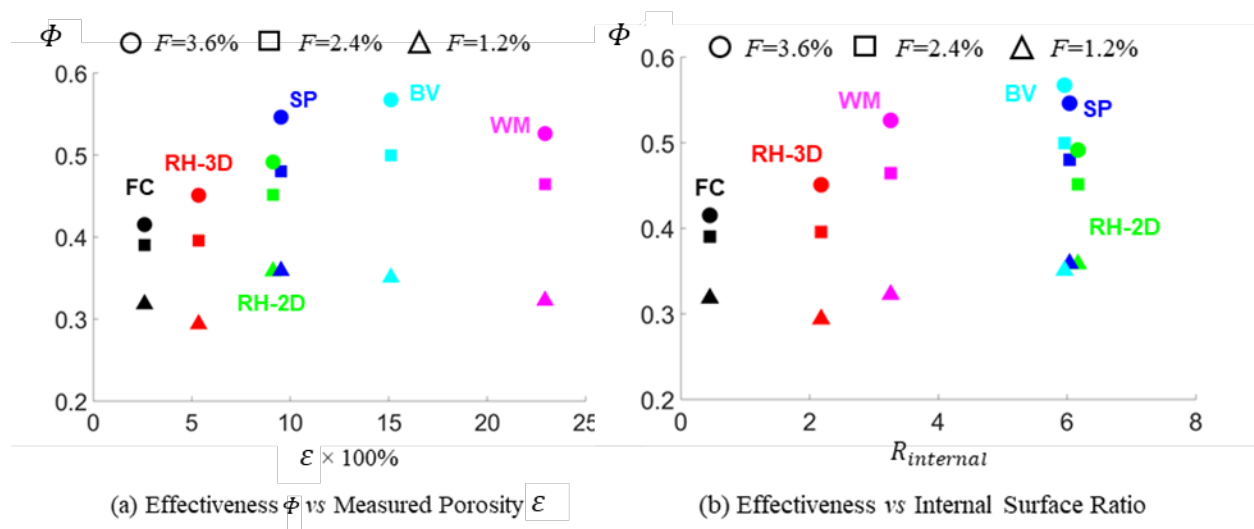


Figure 4.9 Effect of porosity and internal surface area on the transpiration cooling effectiveness

Figure 4.10 shows the spanwise-averaged, streamwise-distributed transpiration cooling effectiveness. In all three sub-figures, the Φ values of all the five transpiration cooling cases increase initially, reaching a peak in the middle part ($x/L = 0.4 \sim 0.8$) of the target surface. On the contrary, the value of Φ for the film cooling case initiates with a peak immediately downstream to the film cooling hole and declines consistently along the streamwise direction, followed by a slight increase near the rear end of the test section. This initial drop of the Φ value of film cooling was possibly because of the lift-off phenomenon downstream of the ejection hole area. The strong film

cooling ejection penetrated the hot gas, exposing the target surface without coolant film protection, which resulted in lower Φ values in the middle part of the test section. Further downstream, the coolant film reattached to the surface, leading to a slight increase of the Φ value in film cooling. For transpiration cooling, the coolant film was getting thicker by the coolant replenished from numerous small pores or outlets along the mainstream direction, leading to an increase of Φ from the leading edge. The highest cooling effectiveness area occurred around the mid-section of the test plate ($x/L = 0.4 \sim 0.8$) rather than near either end of the test section. A possible reason for this phenomenon was that the convective cooling inside the porous media played an important role in cooling the mid-section by dissipating the heat into the surrounding areas. This uniformly distributed heat sink (coolant) inside the substrate effectively lowered the surface temperature in the center part of the substrate, leading to higher Φ values there. On the contrary, the coolant flow in film cooling only passed through the film cooling holes near the leading edge of the test plate, resulting in the peak of Φ distribution occurring at the very beginning.

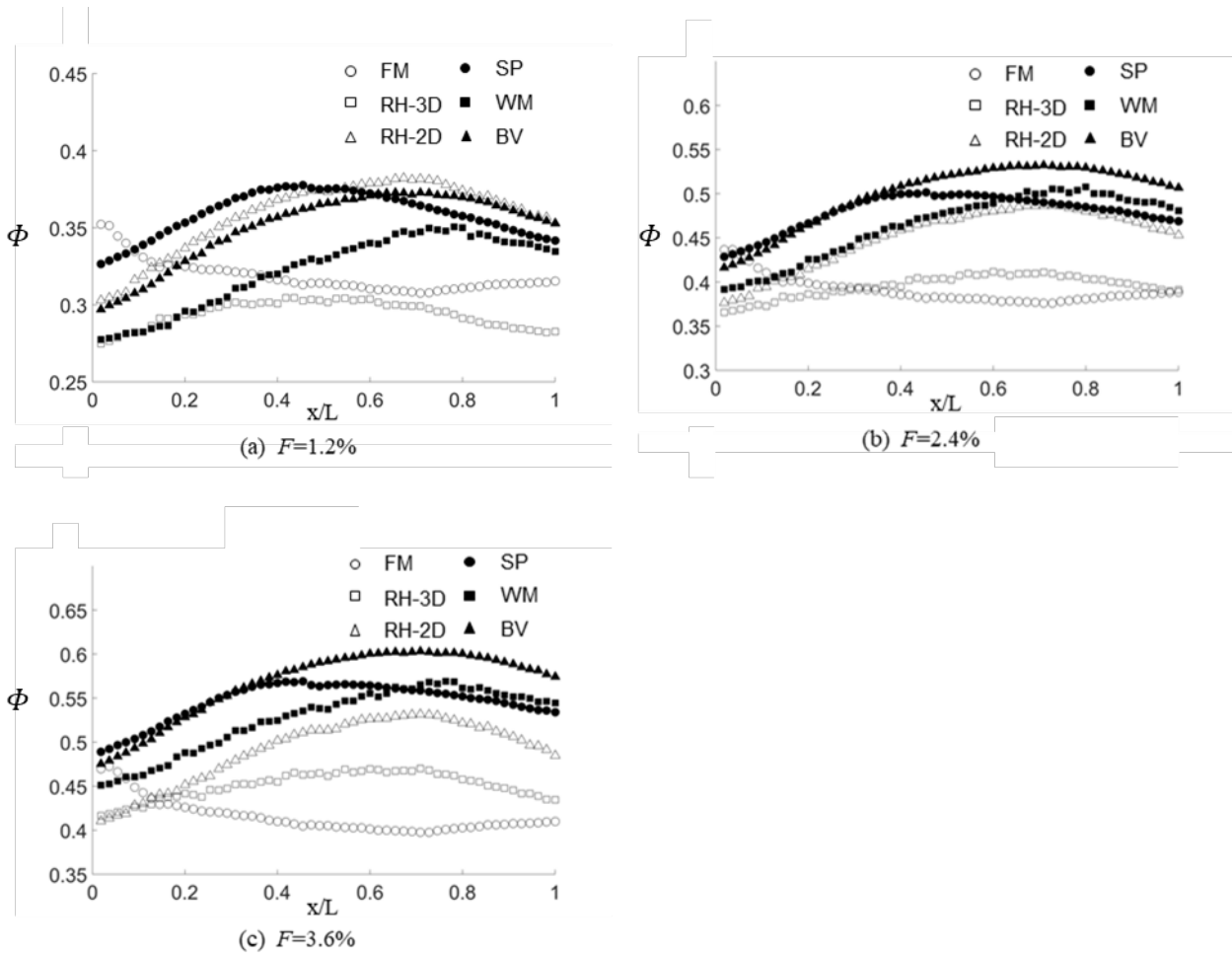


Figure 4.10 Spanwise averaged, streamwise distributed transpiration cooling effectiveness

In summary, the work in this section compared the cooling performance of the AM-made transpiration cooling and film cooling structures. The results showed that the cooling potential of the transpiration cooling at the target surfaces was higher than its film cooling counterpart. The above analysis also showed that the internal solid-fluid interface area in the porous substrate could be a significant geometric parameter to affect the cooling performance other than the commonly investigated parameter, the porosity, in the previous literature. The effects of the geometric parameters for straight-hole configurations will be further investigated in the next section.

4.2 Effect of Geometric Parameters on the Cooling Performance for Straight-Hole Transpiration Cooling Configurations

4.2.1 Methodology

The work in this section investigated the effects of geometric parameters on the transpiration cooling effectiveness of different straight-hole structures. Most previous studies looked mainly into the impacts of a unified geometric parameter, i.e., the porosity. A comparison of the five different transpiration cooling designs in Section 4.1 suggested that the porosity may not be the sole parameter dominating the thermo-fluid performance of a transpiration cooling system [132]. With significant convective heat transfer prevailing inside the porous substrate, the internal heat transfer area should be considered as an important parameter as well. With this notion in mind, this study made use of arrays of small straight round holes as a reference test model to experimentally examine the effects of porosities and internal heat transfer areas on the performance of transpiration cooling.

The straight-round-hole inline configurations (Fig. 4.11) were employed in this section for the geometric parameter study. Each unit cell contains one hole and the surrounding solid part as shown in the figure. Eq. (4.4) and (4.5) give each unit cell's area and the total number of the unit cells within a transpiration cooling area A respectively.

$$A_{unit} = P^2 = (nD)^2 \quad (4.4)$$

$$N = \frac{A}{P^2} = \frac{A}{(nD)^2} \quad (4.5)$$

where P is the hole pitch, n is the pitch-to-diameter value, and D is the hole diameter.

Therefore, the total outlet area, the porosity, and the internal solid-fluid surface area can be calculated as:

$$A_o = \frac{1}{4}N\pi D^2 = \frac{A}{4P^2}\pi D^2 = \frac{\pi A}{4n^2} \quad (4.6)$$

$$\varepsilon = \frac{A_o t}{At} = \frac{\pi}{4n^2} \quad (4.7)$$

$$A_i = N\pi Dt = \frac{\pi At}{n^2 D} \quad (4.8)$$

where A_o is the total outlet area, ε is the porosity, t is the wall thickness, and A_i is the internal wetted area.

It can be concluded from Eq. (4.6) – Eq.(4.8) that the porosity is a function of the pitch-to-diameter ratio value n only, while the internal solid-fluid interface area is a function of both pitch value n and the channel diameter D . This means when designing the straight-hole transpiration cooling structures, using various channel diameters with the same pitch-to-diameter value would not change the porosity but the internal wetted area. A larger channel diameter would lead to a smaller inner solid-fluid interface area. Therefore, nine straight-hole configurations with three different pitch values ($P = 1.5D$, $P = 2D$, $P = 3D$) and three channel sizes (0.3mm, 0.4mm, 0.5mm) were designed and fabricated in this section for the investigation of the effect of porosity and internal surface area on transpiration cooling effectiveness.

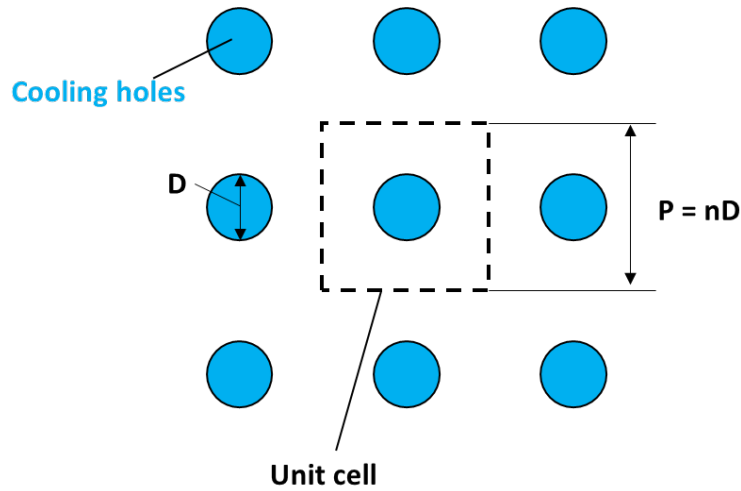


Figure 4.11 The illustrative drawing of a cross-sectional unit cell

The accurate fabrication of microchannels was essential in this study to provide various microchannel configurations for investigating the impact of the geometric parameters. As described in Chapter 2, the DMLS method generates straight microchannels with size contractions from the designed channel sizes to the as-produced values. Such offset would deviate the geometric dimensions of the cooling structures from the originally designed levels of porosity and internal surface area. This would be a significant source of uncertainty for the intended study and negatively impact the quality of measured data. To alleviate this geometry control issue, the CAD compensation method that was introduced in Chapter 3 and Chapter 2 was employed to make the channel size close to the designed values. Fig. 4.12 shows the SEM photos for the outlet surface of the as-printed samples after the CAD model redesign. It is evident that the as-produced channel size is close to the objective values (green circles). Table 4.1 shows a comparison between the average channel sizes at the outlet surface made with the CAD-correction and the originally designed values. All the ratios of the as-printed channel size to the corresponding design value are

close to 1. These as-printed coupons were painted in black to increase the radiation emissivity, as shown in Fig. 4.13, for the subsequent heat transfer test.

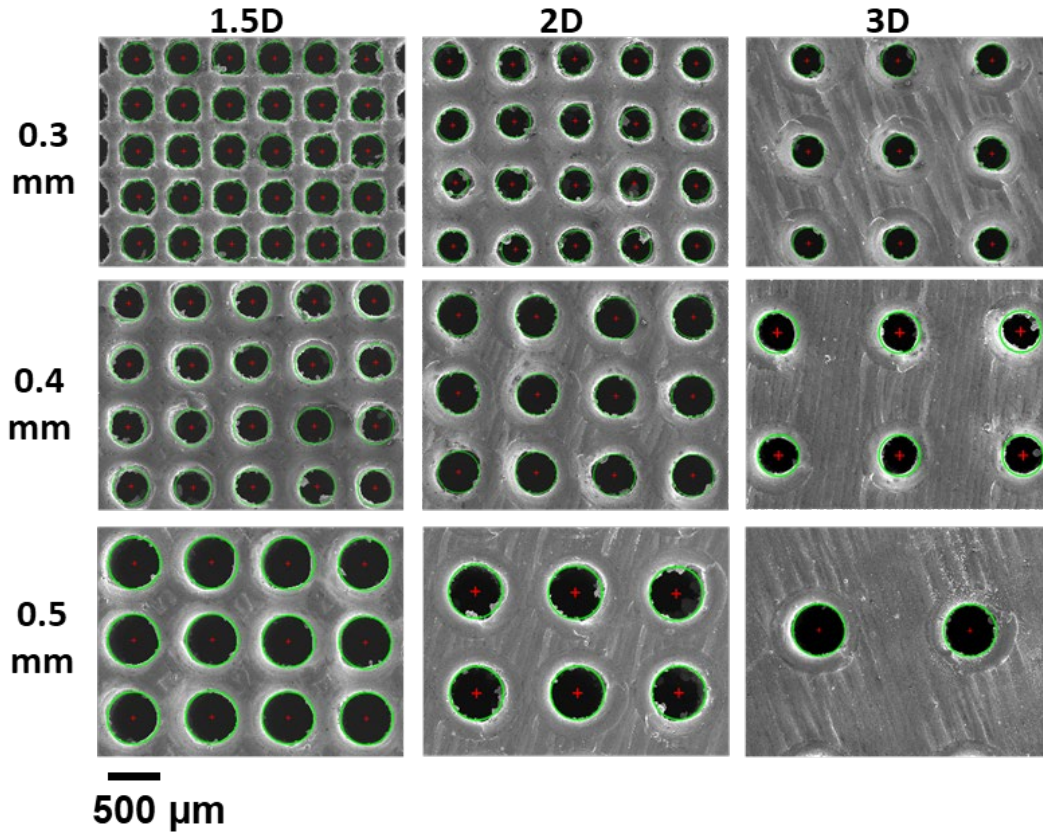


Figure 4.12 SEM photos at the outlet surfaces of the as-printed samples after CAD compensation

Table 4.1 Comparison of objective channel sizes and as-produced channel sizes

Objective Channel Diameter	Hole Pitch	Designed Channel Size	Averaged As-printed Channel Size	R_p/R_o
300 μm	P = 1.5D	408.2 μm	293.6 μm	0.979
	P = 2D	389.8 μm	289.7 μm	0.966
	P = 3D	383.0 μm	295.4 μm	0.985
400 μm	P = 1.5D	505.8 μm	392.8 μm	0.982
	P = 2D	482.0 μm	399.6 μm	0.999
	P = 3D	480.4 μm	394.5 μm	0.986
500 μm	P = 1.5D	603.2 μm	487.9 μm	0.976
	P = 2D	574.2 μm	490.0 μm	0.980
	P = 3D	577.8 μm	491.4 μm	0.983

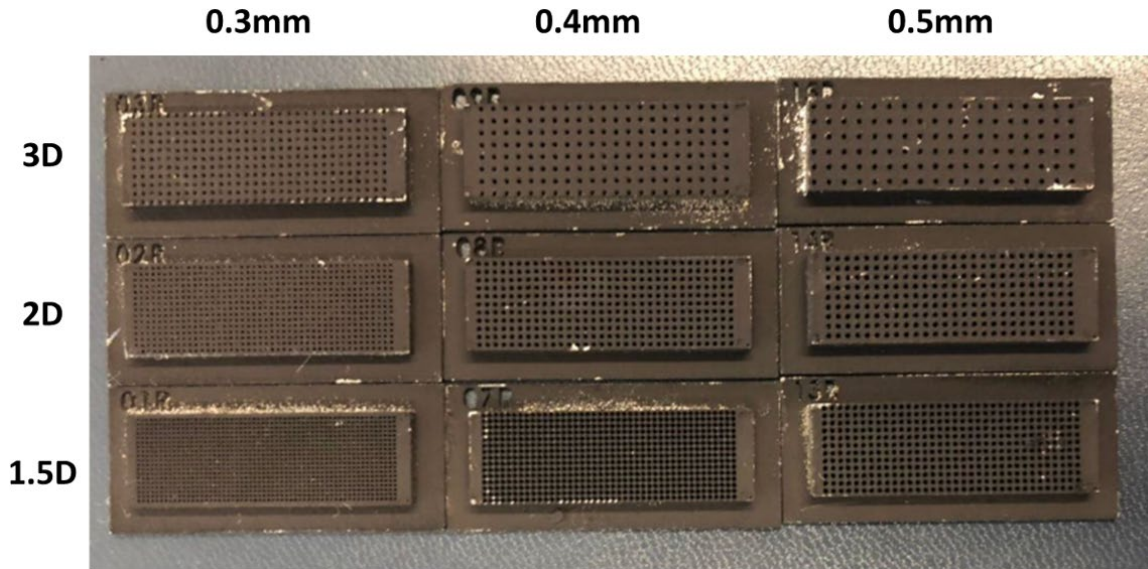


Figure 4.13 Black painted test specimens for the heat transfer test

4.2.2 Results and Discussions

The transpiration cooling effectiveness distributions of the nine configurations are displayed from top to bottom in Fig. 4.14. The results under three mass-flow rates are presented from left to right. One consistent observation is that the highest cooling effectiveness area for all cases occurred in the region slightly downstream to the mid-section, rather than the downstream most region. The high cooling effectiveness was caused by the accumulation of the coolant film from upstream, combined with the conduction effect diffusing the heat to the surroundings. Three conclusions can be drawn from the test results: First, the transpiration cooling effectiveness increases when using a larger injection ratio; Second, with the same designed channel diameter, the transpiration cooling effectiveness drops as the hole spacing increases; Third, the cooling performance decreases with the increase of the transpiration hole size.

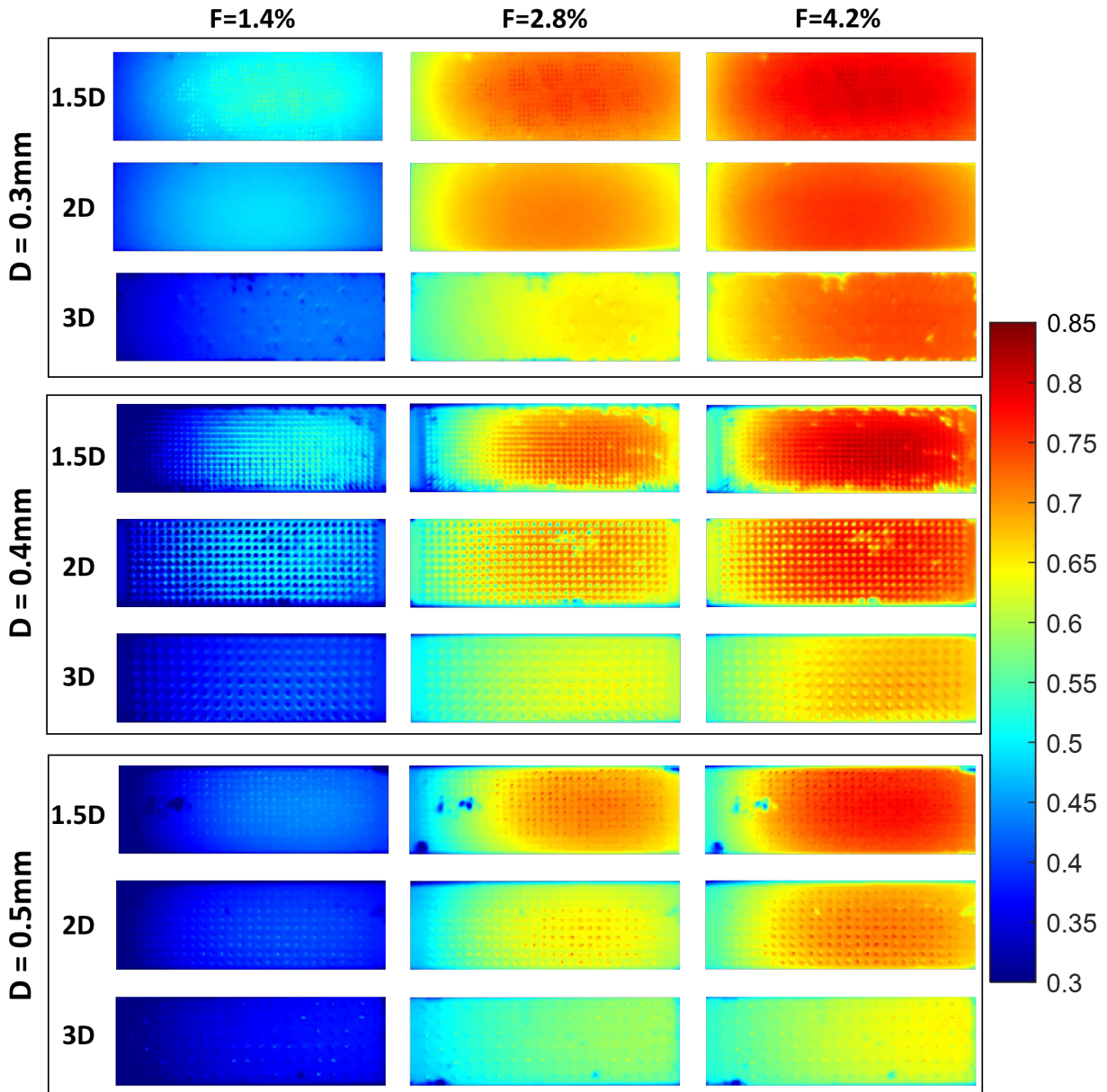


Figure 4.14 Transpiration cooling effectiveness distributions of various hole configurations

The quantitative analysis in Fig. 4.15 of the area-averaged transpiration cooling effectiveness further confirms the tendency observed above. When an increase in the injection ratio F from 1.4% to 2.8%, the averaged Φ values in all cases increase more than 40%, while a much smaller increment, <20%, exhibited when further increasing the injection ratio F to 4.2%.

More coolant injection, implying a higher coolant flow rate, can provide better cooling protection over the hot surface. However, keep increasing the F value can lead to the coolant film's lift-off, as the coolant jets of high momentum fail in attaching to the surface and penetrate the hot-gas stream. Such a lift-off phenomenon associated with a high injection ratio offsets the effect of more coolant introduced in the boundary layer over the protected surface, hence lower the level of cooling performance. When comparing the effects of different hole spacing, the smaller hole-pitch-to-diameter ratio P results in higher cooling efficiency. For a given coolant flow rate or a fixed amount of coolant consumption, the smaller P leads to a higher level of porosity ε of a given test sample. It also suggests that the overall size of the opening area A_o on the sample top surface subject to transpiration cooling increases. As discussed in Section 1.2.3 and 4.1.5, a higher ε value can elevate heat removal capability inside the wall beneath the coolant protected surface, while a larger coolant outlet area A_o reduces the ejection momentum, making coolant attachment to the protected surface more uniform and stable. Thus, a smaller hole-pitch-to-diameter ratio shows better transpiration cooling performance.

The parametric influence of hole size D alone on the cooling efficiency Φ is different from the effects of the hole-pitch-to-diameter ratio P , as described above. Both the coolant outlet area A_o and the porosity ε are a function of P only based on Eq. (4.6) and (4.7). With the same P value, specimens with varying hole size D have identical ε and A_o , as shown in Table 4.2. However, the internal solid-fluid interface area A_{int} is a function of both P and D . A larger designed diameter D leads to a smaller A_{int} , which reduces the convective heat transfer area inside the wall. This impact from the A_{int} is analogous to the effect of compactness β in heat exchanger analysis. The compactness value β , defined as the ratio of the internal wetted area to the volume, is commonly used to evaluate the heat transfer capability of heat exchanger [133]. A high value of β provides a

larger heat transfer area within a specific volume, leading to higher heat exchange efficiency. Similarly, the enlarged A_{int} augments the heat removal capabilities in the porous substrate. Therefore, the designed compactness values β were introduced in this study as a geometrical parameter to evaluate the cooling performance. Table 4.2 shows the β values of all test specimens, and a plot of the correlations between compactness β and transpiration cooling effectiveness Φ is presented in Fig. 4.16. It can be seen that for all three coolant injection ratios, the Φ value is getting higher when using a larger designed β value. These results show that the compactness value β is a more dominating geometrical parameter than porosity to evaluate the transpiration cooling effectiveness.

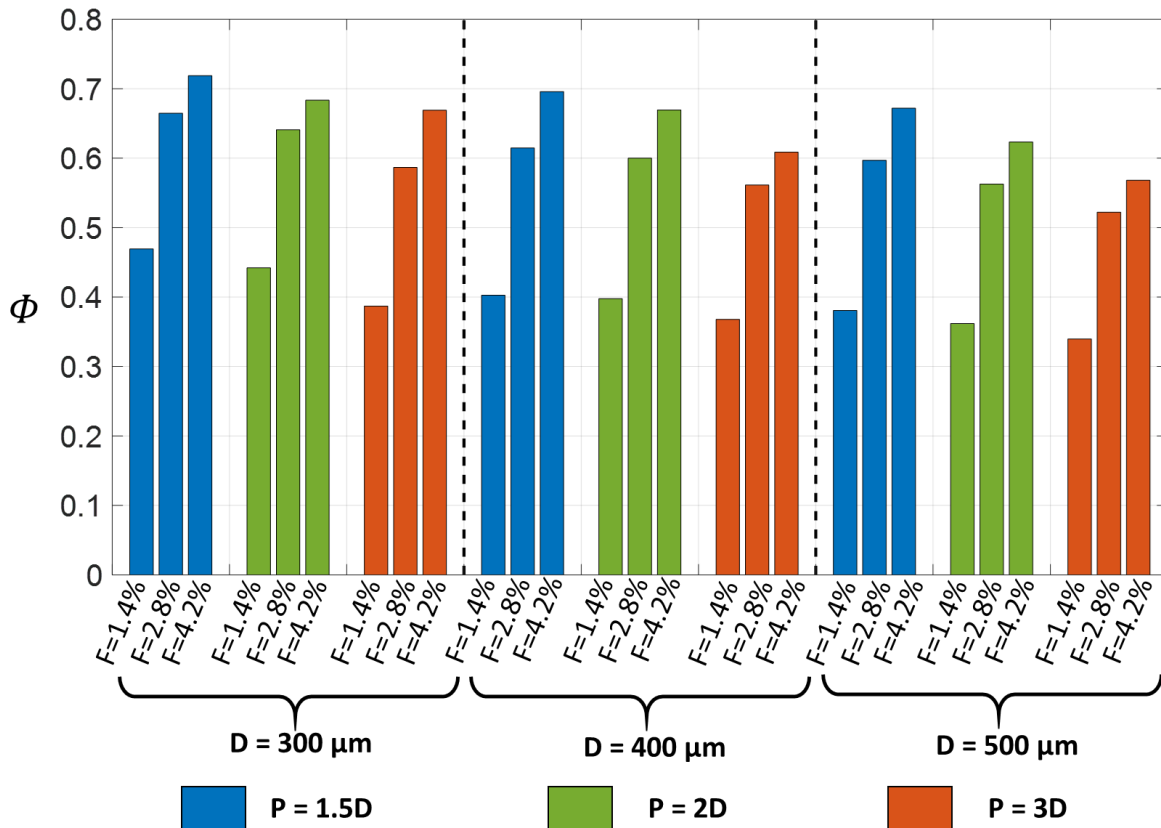


Figure 4.15 Area-averaged transpiration cooling effectiveness comparison

Table 4.2 Porosity and compactness comparison of various hole configurations

Objective Channel Diameter	Hole Pitch	Designed Porosity ε	Designed Compactness β (m^2/m^3)
300 μm	P = 1.5D	0.349	4654.2
	P = 2D	0.196	2618.0
	P = 3D	0.087	1163.6
400 μm	P = 1.5D	0.349	3490.7
	P = 2D	0.196	1963.5
	P = 3D	0.087	872.7
500 μm	P = 1.5D	0.349	2792.5
	P = 2D	0.196	1570.8
	P = 3D	0.087	698.1

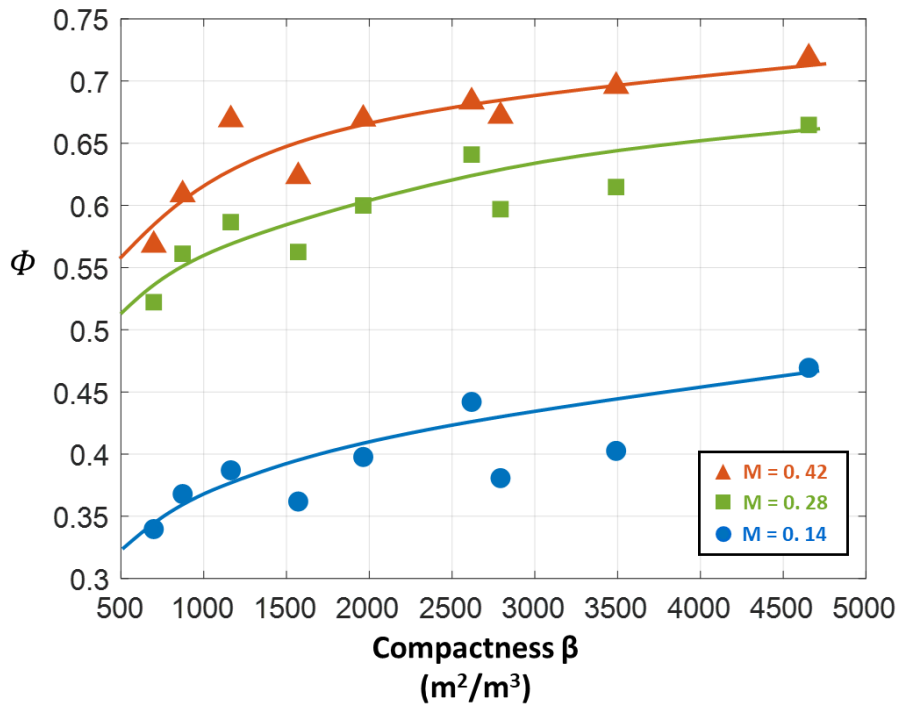


Figure 4.16 Plot of the transpiration cooling effectiveness vs. compactness

5.0 Heat Transfer Coefficient Investigations

While a significant number of studies have been focused on the cooling effectiveness of transpiration cooling, much less study on characterizing the heat transfer coefficient (HTC) with transpiration cooling can be found in the open literature. Experimental HTC data with detailed local distributions are particularly lacking. The cause of such an absence of HTC studies on transpiration cooling stems from the complex geometric conditions in conjunction with difficulties in experimental setup on the target surface. With hundreds of ejection holes in a small area, it is challenging to attach a tape/foil heater onto the surface without clogging the coolant ejection. Moreover, the nature of the porous media in transpiration cooling fails in complying with the semi-infinite conduction model, thus the transient HTC measurement approach often implemented for turbine heat transfer studies is inadequate to use here. Benefiting from the advancement of manufacturing technique, a thin layer of silver wiring could now be coated onto the target surface of a resin sample made by additive manufacturing (AM) without blocking the channel outlets. An electric circuitry was arranged to provide the target surface with a designed resistance pattern so that a uniform heat flux (UHF) boundary condition can be achieved when the circuitry is fed with a constant direct current. Hence the steady-state HTC experiment became possible for transpiration cooling structures. The design of the microheater and details of the HTC measurements are described below. A manuscript regarding the work in this chapter has been submitted to and accepted by the ASME Turbo Expo conference 2021 [134].

5.1 Micro-Lithography Method for Surface Heater Fabrication

The objective of the surface heater design is to provide a uniform heat flux boundary condition over the target surface. The surface heater fabrication process was divided into three steps to achieve this goal. In the first step, the low thermally conductive test plates were fabricated using stereolithography (SLA) printing. Step 2 is to design the wiring patterns to ensure uniform heating power on the target surface. The third step is to use a physical vapor deposition (PVD) technique to coat the silver pattern onto the target surface. These three steps will be illustrated in the following three sections.

5.1.1 SLA Printing of Transpiration Cooling Samples

The steady-state heat transfer test requires a low thermally conductive test sample to reduce the conduction loss to the cold side. Hence, transpiration cooling plates with the same dimensions as the specimens in Chapter 4 were made by an SLA printer (3D Systems Viper SI2) using resin material (Somos® WaterShed XC 11122). The sample's thermal conductivity is lower than 0.3 W/m·K based on the user guide of the material. Five straight-hole configurations were designed and fabricated by the SLA printing, as shown in Fig. 5.1. Three of these five samples with the same hole size (500 μm) have three different hole pitches (2D, 2.5D, and 3D) so that the effect of the hole pitch can be studied. Also, three samples have the same pitch (3D) but different designed hole diameters (400 μm , 450 μm , and 500 μm) for studying the effects of the hole size.

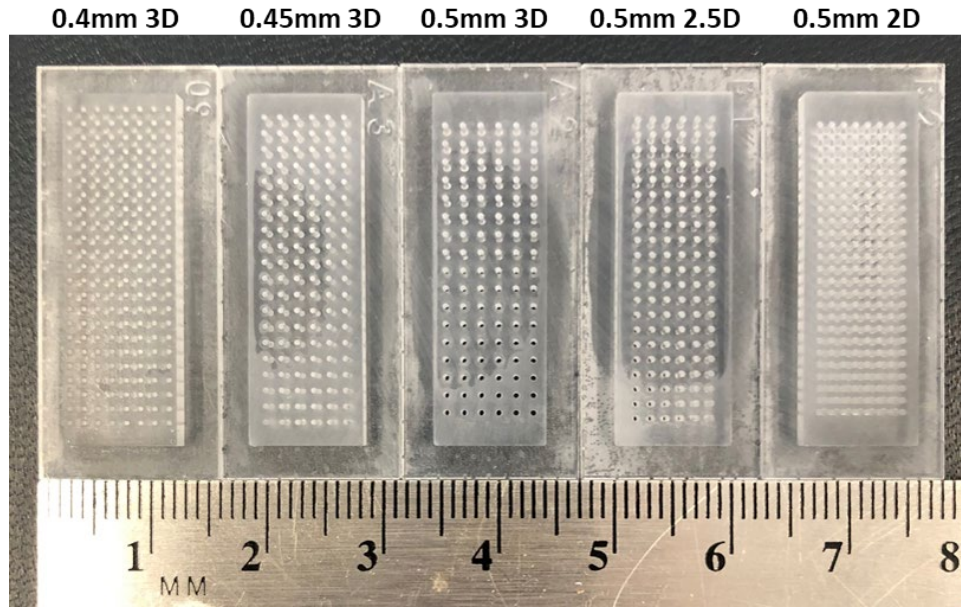


Figure 5.1 SLA printed transpiration cooling samples

5.1.2 Surface Heater Design

The surface heater attached to the limited surface area must contain two parts, the patterned wiring part as the heating zone and the leads zone with two electrodes connected to the power supply, as shown in Fig. 5.2. To minimize the interference from these physical features with the flow and transport phenomena in the heat transfer test, two specific designs were developed to address this issue. First, the thickness of the circuit pattern needs to be as thin as possible ($< 1\mu\text{m}$), hence the original surface profile can be well preserved, and the increase in surface roughness is insignificant. For the two electrodes, a silver-epoxy paste was used to connect the copper wire between the power supply and the surface heater, thereby generating humps on the surface. Therefore, these two electrodes were placed on the downstream end of the test section to minimize the interference with the flow and heat transfer test.

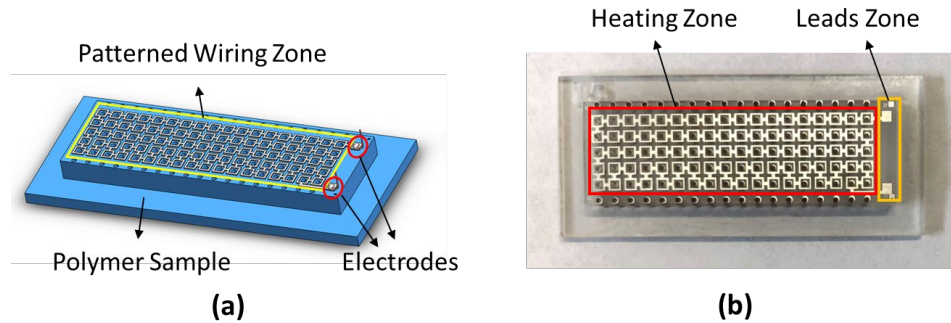


Figure 5.2 Surface heater design: (a) A schematic view; (b) The top view photo of the surface heater

The patterned circuit design is the key to providing a uniform heating condition. Most commercial tape heaters covering hollow surfaces use an in-series circuit design as shown in Fig. 5.3. The asymmetric in-series circuit around the hole would produce non-homogeneous heat flux, generating noises and uncertainties for the subsequent HTC data acquisition. To negotiate hundreds of holes distributed at the target surface, an in-series circuit will require a long single wire with many turns and curves, resulting in high electric resistance overall. Therefore, the initial tentative pattern design used a parallel circuit as shown in Fig. 5.4 (a). This circuit design consisted of five parallel blocks, each of which was represented by the wiring between the two connection points in the figure (i.e., the first block is the circuit between connection point A and B, the second is between C and D, and so on). Fig. 5.4 (b) shows the equivalent circuit diagram, in which the electrical resistance from R_1 to R_5 represents the five parallel blocks. The electrical resistances of R_1 to R_5 are equal because all these five circuit blocks are designed identically. However, the voltage distributed to these blocks is slightly different because a resistance (R_0) of the wire between the parallel blocks exists. It causes a voltage drop along the wire, although the resistance of R_0 is relatively small, only about $1/23$ of R_1 . Therefore, the voltage applied to the blocks further away from the input electrodes is smaller, resulting in $U_5 < U_4 < U_3 < U_2 < U_1$. Such voltage differences

contributed to a non-uniformly heat flux when applied a direct current to the circuit. This, in turn, led to a significant temperature difference between each block in the static heating test, as shown in Fig. 5.4 (d).



Figure 5.3 An example of the commercial heater design [135]

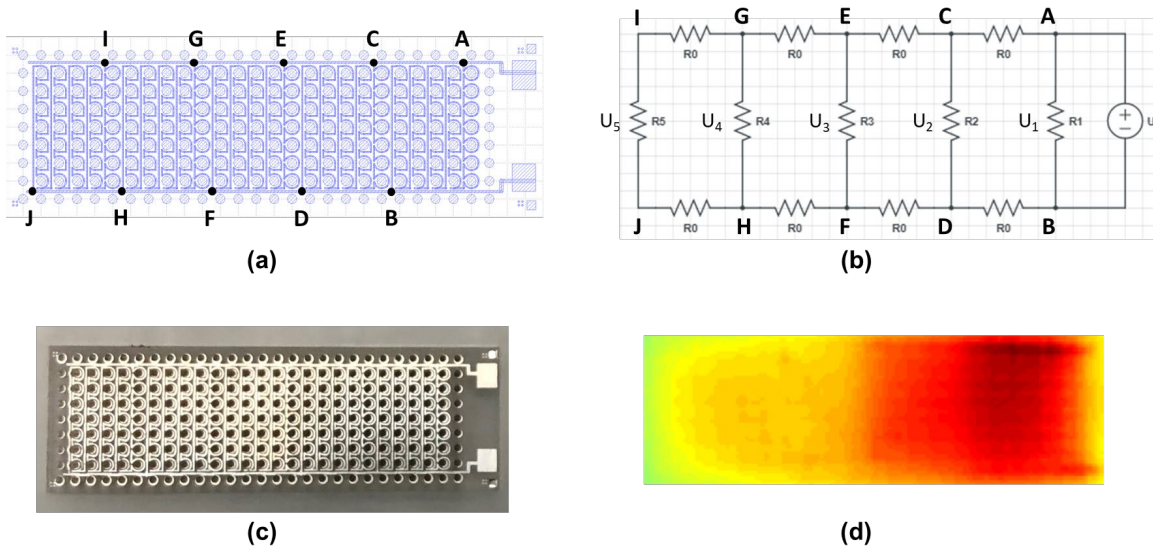


Figure 5.4 The tentative surface heater design: (a) circuit pattern design; (b) the equivalent circuit diagram; (c) Top view photo of the heater; (d) the non-uniform temperature distribution during heating

An improved circuit pattern design was developed to produce identical heating power in each unit cell area. With uniform heating in each unit cell and in-series connection joining all the unit cells, the electric power generation was expected to be uniform throughout the entirety of the test surface with a large number of transpiration cooling holes. Fig. 5.5 shows one unit cell on the

transpiration cooled surface, which contains the opening area of a coolant hole and the surrounding solid area. The solid area is divided into four zones with identical areas, displayed by four colors in the figure. A parallel circuit with two identical current paths was designed within the unit cell, as shown in Fig. 5.5 (b). This was to provide the same heating power for the two branches when the current was offered. Fig. 5.5 (c) shows the equivalent circuit diagram in the unit cell. With the symmetry of the two current paths, the power in zone 1 is equal to zone 3, while the power in zone 2 is equal to zone 4. Thus, the uniform heating pattern design was reduced to the governing equations as shown in Eq. (5.1) - Eq. (5.5). The width of the connection wire w_c and the horizontal wire w_h were set empirically based on the available space between adjacent holes. The vertical wire width w_v could then be calculated as shown in Table 5.1.

$$P_1 = I_c^2 R_c + 2I_h^2 R_v \quad (5.1)$$

$$P_2 = I_h^2 R_h \quad (5.2)$$

$$R_c = \rho \frac{L_c}{w_c t} \quad (5.3)$$

$$R_v = \rho \frac{L_v}{w_v t} \quad (5.4)$$

$$R_h = \rho \frac{L_h}{w_h t} \quad (5.5)$$

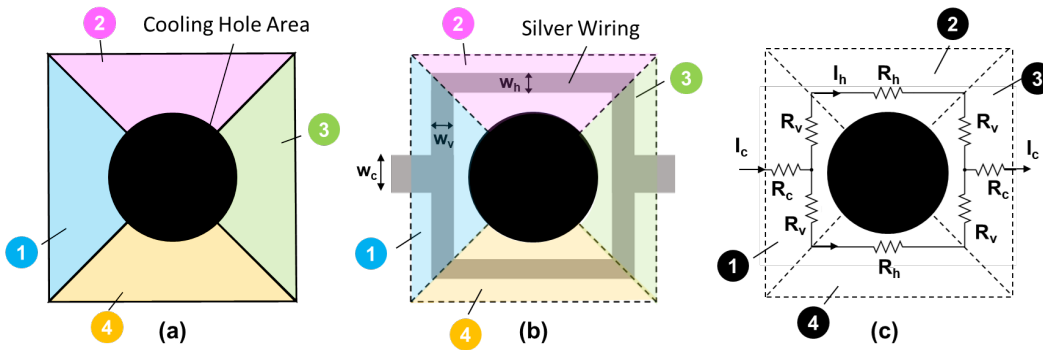


Figure 5.5 The circuit design in a unit cell: (a) Four evenly divided solid zones in a unit cell; (b) Silver wiring pattern design in a unit cell; (c) The equivalent circuit diagram

Table 5.1 Wire width designs of the surface heaters with different hole configurations

Hole configuration	Width of connecting wire, w_c	Width of horizontal wire, w_h	Width of vertical wire, w_v
D = 400 μm P = 3D	200 μm	100 μm	146.4 μm
D = 450 μm P = 3D	200 μm	100 μm	150 μm
D = 500 μm P = 3D	200 μm	100 μm	153.1 μm
D = 500 μm P = 2.5D	200 μm	100 μm	137.3 μm
D = 500 μm P = 2D	120 μm	60 μm	78 μm

5.1.3 Surface Heater Fabrication

The micro-lithography technique was employed to coat the silver wiring pattern directly atop the transpiration cooling target surface. This technique was widely used for fabricating microelectromechanical systems (MEMS) devices such as sensors [136, 137], actuators [138, 139], and transistors [140, 141]. Facilitated with the photomask or shadow mask on the substrate, the patterned thin-film material can be deposited onto the target surface by physical vapor deposition to produce a designed circuit with tolerance within 10 μm . The coating process was completed by an electron-beam vapor deposition system (Plassys Electron Beam Evaporator MEB550S). Before the deposition process, the target surface of the transpiration cooling specimen was polished, cleaned, and then covered by a custom-designed commercial shadow mask (Photo Sciences, Inc.), which was a thin nickel-brass sheet with pattern features etched completely through the material. Source materials (Ag and Ti in this work) were then vaporized into the gaseous phase by the intense electron beam under a high vacuum, passing through the etched opening of the shadow mask. These gaseous atoms precipitated into the solid form of a thin film following the designed

pattern on the target surface. The wiring pattern was made of two materials, a thin layer (15 nm) of titanium at the bottom to enhance the adherence between resin substrate and a thicker layer (400 nm) of silver to complete the designed circuit. Fig. 5.6 (a) shows illustrative diagrams of the coated wire pattern. Two separate shadow masks were used for each vaporized specimen to complete the wire pattern fabrication as shown in Fig. 5.6 (b).

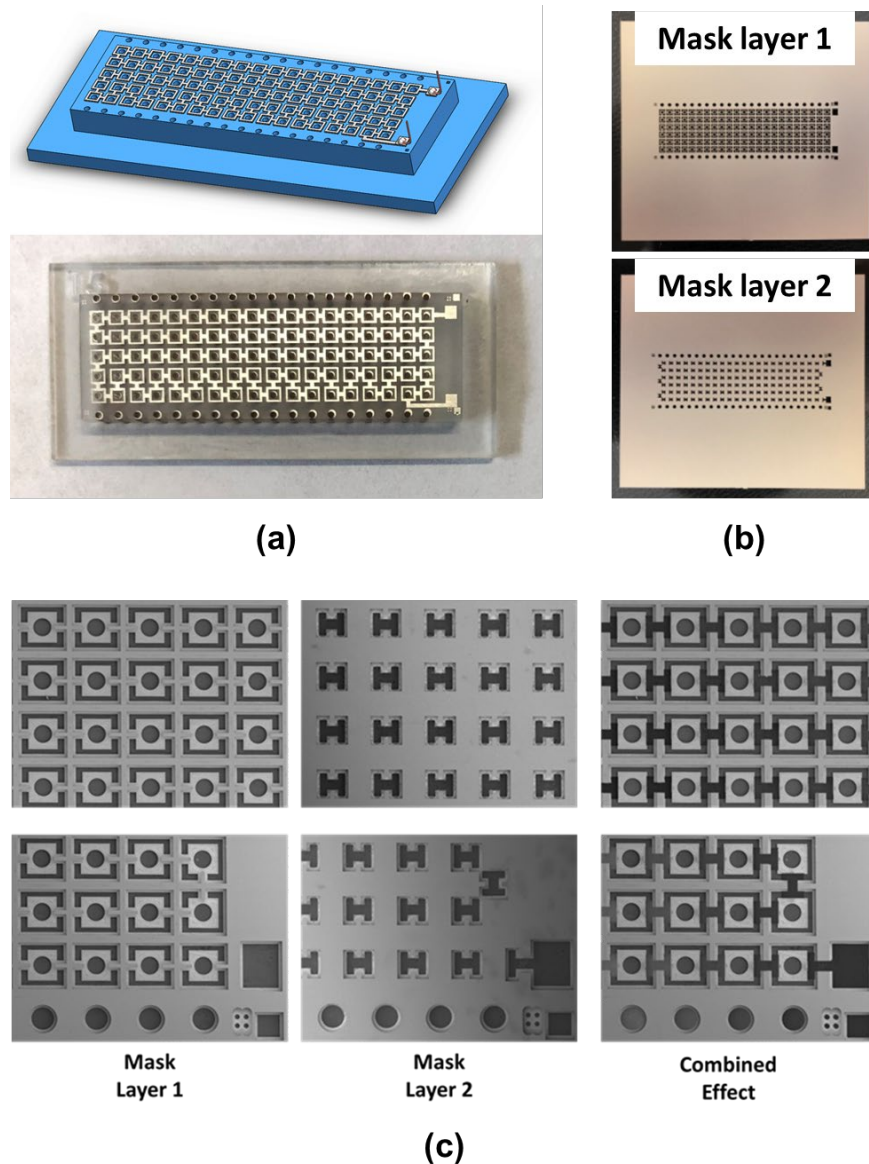


Figure 5.6 Illustrative figures of surface heater fabrication: (a) a schematic view and the photo of one coated example; (b) photo of two shadow mask; (c) SEM photos of the mask pattern and the combined effect of the designed pattern

Figure 5.7 shows the circuit pattern designs and surface heater photos of the as-produced five specimens with different hole configurations. A silver-epoxy paste adhesive (AI Technology INC) was used to attach two copper wires to the two electrodes in the leads zone near the downstream end of the test plate. Table 5.2 shows the measured electrical resistance at room temperature (21 °C) for the five test cases with different wire patterns. The as-produced resistance shown in Table 2 is consistently higher than the corresponding designed value by about 1 to 3 Ω . This is likely due to the resistance of the silver-epoxy paste manually applied after the vapor deposition process was completed. Each test plate after installing the microheater was then painted black to increase the emissivity for temperature measurement using infrared (IR) thermography. Prior to actual experiments for measuring the heat transfer coefficient, the static heating tests were conducted to examine the uniformity of the heat flux at the target surface. The test results were illustrated in Fig. 5.8. When applied electric power of 0.2W to the heater, the target surface's temperature variation needed to be smaller than 0.25 °C. The test plates which failed in meeting the 0.25 °C tolerance were refabricated and recoated until the uniform heating condition was achieved.

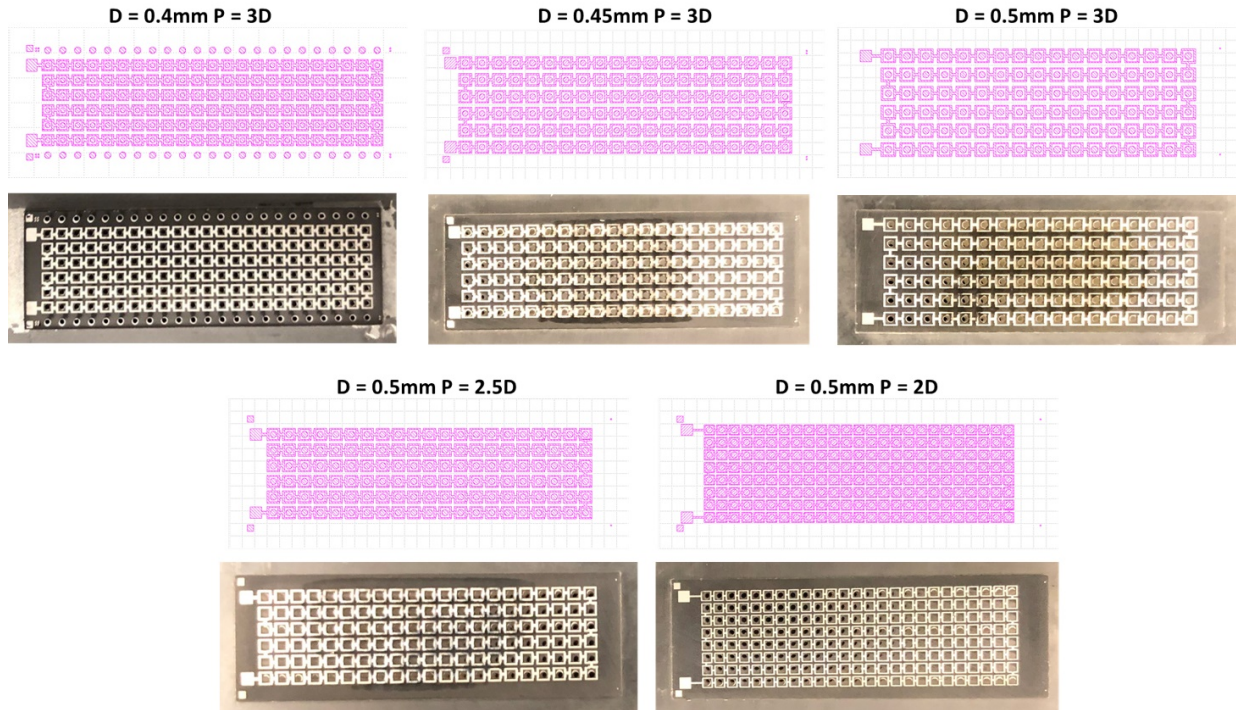


Figure 5.7 Circuit designs and the as-produced surface heaters

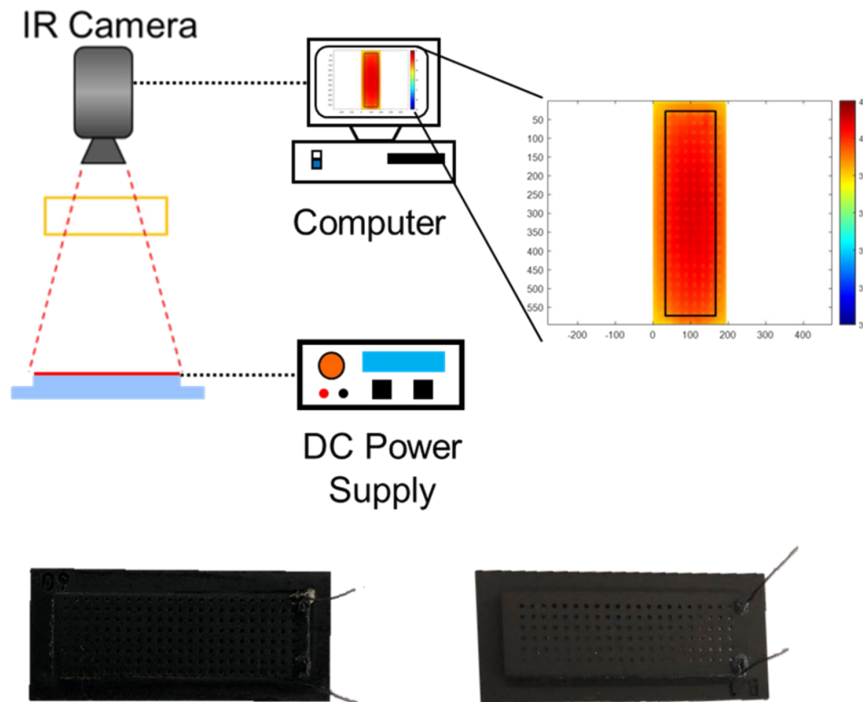


Figure 5.8 The static hating test setup and two example specimens after black painting

Table 5.2 Electrical resistance of the surface heaters

Hole configuration	Designed electrical resistance	As-produced resistance
D = 400 μm P = 3D	36.98 Ω	38.20 Ω
D = 450 μm P = 3D	35.83 Ω	37.92 Ω
D = 500 μm P = 3D	33.58 Ω	36.75 Ω
D = 500 μm P = 2.5D	37.92 Ω	40.01 Ω
D = 500 μm P = 2D	87.97 Ω	89.22 Ω

5.2 Heat Transfer Test

5.2.1 Methodology, Test Facility, and Procedure

As stated earlier, to estimate the efficacy and performance of a transpiration cooling system requires the quantitative information of overall cooling effectiveness φ , adiabatic cooling effectiveness η , and heat transfer coefficient ratio h_f/h_0 as demonstrated in Eq. (1.3). Typically, the overall cooling effectiveness $\varphi = (T_g - T_w)/(T_g - T_c)$ is presumed in the range of 0.5-0.8 under the real engine conditions [88, 91, 142]. This nondimensional surface temperature scaled with the mainstream and coolant temperatures can also be evaluated in a laboratory test described in Chapter 4 using the test section with a Biot number similar to the actual turbine airfoil [143, 144].

The main scope of this chapter is to characterize the local distributions of the other two parameters, η and h_f/h_0 , for evaluating the cooling efficacy. To experimentally determine the values of η , h_f , and h_0 , it requires different heat transfer and flow settings on the test surface, e.g.,

heater on/off, with/without coolant injections. Thus, three separate sets of steady-state tests were designed to obtain the local distributions of these variables, as shown in Fig. 5.10. These three tests in the figure would be referred to as Test A, Test B, and Test C hereafter.

Test A is the adiabatic cooling effectiveness (η) test. The mainstream temperature was kept at 50°C, while the coolant temperature was 21°C. Using this significant temperature difference ($T_g - T_c$) in attaining the data for η could reduce the relative errors of the temperature measurement, minimizing the total uncertainties in the results. Meanwhile, keeping the hot gas temperature below 55°C could avoid the deformation of the resin-made test plate. During the test, the steady-state wall temperature was recorded by a calibrated IR camera (FLIR A310) when the surface heater was off. The wall temperature recorded will be further corrected by factoring in the heat loss estimated by a finite-element method (FEM), as shown in Section 5.2.2.

Test B is to determine the local magnitude and distribution of h_f with coolant injection and Test C is the corresponding test to determine h_0 without injection. In each test, the wall temperatures were recorded by the IR camera under two heating conditions at the target surface: heater on or off. Both the mainstream and coolant in these two tests were heated to 35°C. Since the convective HTC is dictated predominantly by flow dynamics rather than thermal conditions, the HTC measurements could be obtained using the identical mainstream temperature and coolant temperature. With this approach, the level of heat conduction loss when the heater was on could be significantly reduced, as the temperature difference is much smaller from the hot side to the cold side than using hot mainstream and cold coolant.

In all three tests, three blowing ratios, $M = 0.125, 0.25,$ and $0.5,$ were used for the coolant injection. The temperatures of mainstream and coolant were measured by K-type thermocouples inserted in the wind tunnel and the coolant plenum, respectively. The mean velocity of the main

(hot) stream was measured by a Pitot tube. . The volume flow rates of the coolant were recorded by the Dwyer series RM flowmeter. A DC power supply (Agilent U3606A) provided heating power of 0.2W for Test B and C.

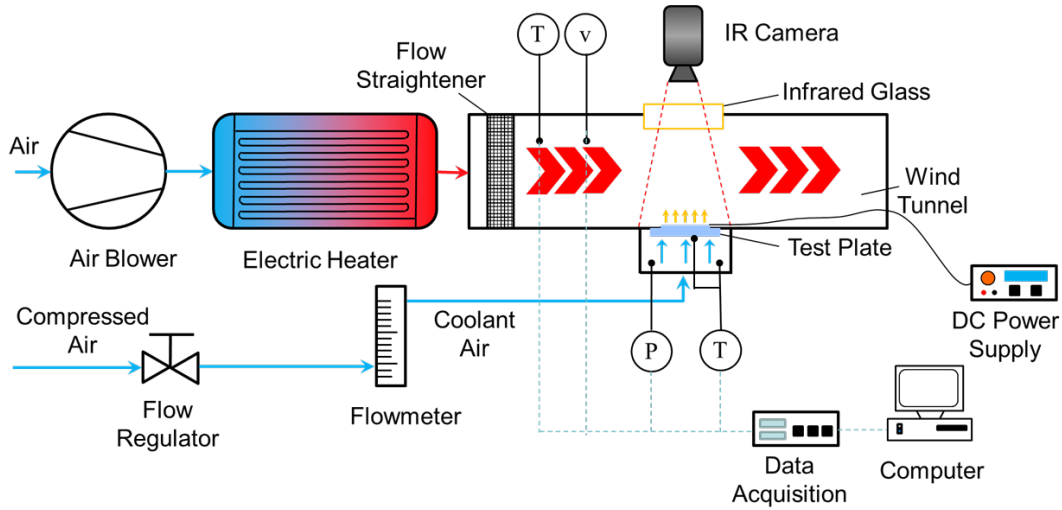


Figure 5.9 Test setup for HTC investigations

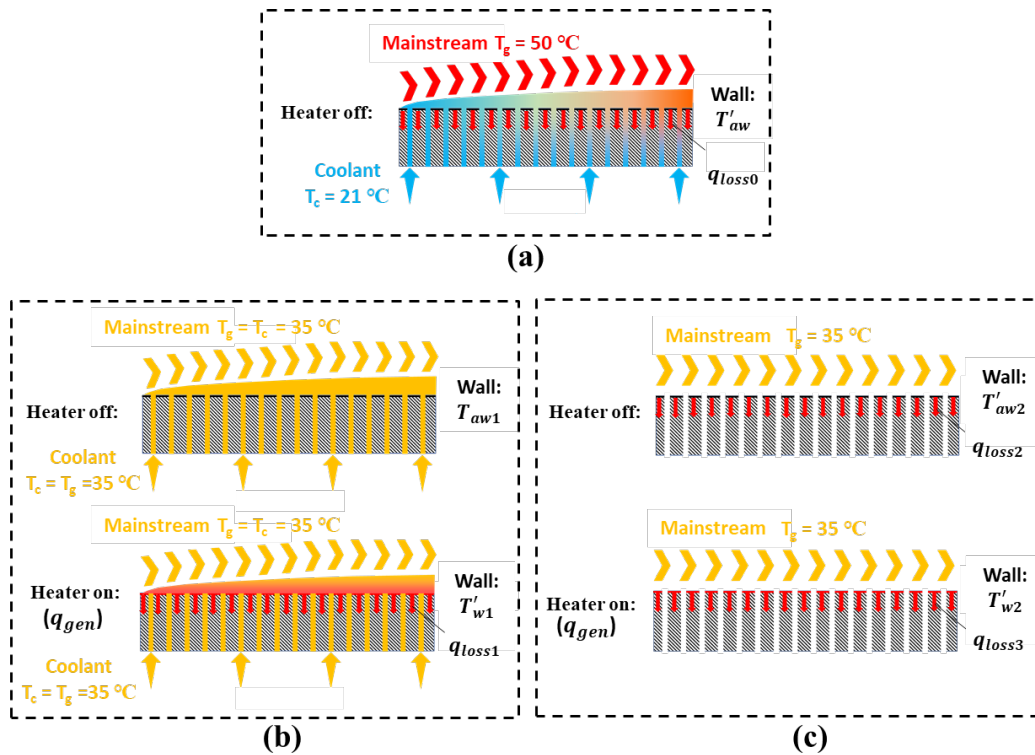


Figure 5.10 Steady-state heat transfer test: (a) Adiabatic cooling effectiveness test; (b) HTC test with coolant injection; (c) HTC test without coolant injection

5.2.2 FEM Post-Processing Method

On a perfectly adiabatic test surface, the adiabatic wall temperature T_{aw} is equal to the measured wall temperature T'_{aw} in Test A. The h_f and h_0 in Test B and C for such a perfectly adiabatic wall can be determined directly by $h_f = q_{gen} / (T'_{w1} - T_{aw1})$ and $h_0 = q_{gen} / (T'_{w2} - T'_{aw2})$, respectively. However, the target surfaces for these tests, though made of resin with low conductivity, were not perfectly adiabatic in reality. The coolant flowing inside the microchannels induced 3-D heat conduction in the test plate, causing uncertainties in the reported surface temperatures, especially in the near hole region and where the wall temperature was significantly higher than the coolant temperature. Therefore, a correction procedure is necessary to evaluate the heat conduction loss.

A 3-D finite-element computational model was developed to correct the experimental tests' non-adiabatic effects with coolant injection. By imposing the steady-state boundary conditions to the solid part of the test section, the heat flux through the target surface could be calculated. This effort to numerically quantify the magnitude of heat loss used a commercial finite-element code, ANSYS 19, with approximately 500,000 to 700,000 meshes for all the five cases shown in Fig. 5.11. Illustrated in Fig. 5.11 are the generated mesh, boundary conditions, and resulted temperature sketch for a partial domain of computation which consists of the first 16 rows and central 4 columns of coolant holes. The boundary conditions were set based on Brauckmann et al. [145] and Facchini et al. [146] 's work. The input of the target surface temperature in FEM was the temperature map obtained from the IR camera in the experiment. The holes' interior wall temperature was set as a linear function of z from T_c to local T_w . Based on the coolant flow rates, the hole interior HTC was evaluated by proper correlations available in the open literature [106].

In Test A, as the mainstream temperature was higher than the coolant temperature, the heat conduction into the heat sink (coolant) led to the measured wall temperature T'_{aw} lower than the adiabatic wall temperature T_{aw} . In this case, T_{aw} could be corrected by Eq. (5.6) using the conduction loss q_{loss0} and the heat transfer coefficient h_f . The magnitude of q_{loss0} could be obtained from FEM while h_f needed to be calculated from Test B. Since the mainstream temperature and coolant temperature were identical in Test B when the heater was off, this is essentially an isothermal system, and no conduction loss through the target surface would be a reasonable assumption. When the heater was turned on, q_{loss1} could be calculated from FEM analysis to correct h_f as demonstrated in Eq. (5.7). Therefore, the data correction process for h_f and T_{aw} is shown in Fig. 5.12. In Test C, the conduction loss q_{loss2} and q_{loss3} were evaluated by the 1-D conduction model since no coolant injection into the plate. The coolant side wall temperature was measured by the thermocouple attached to the backside of the coupon.

$$T_{aw} = T'_{aw} + \frac{q_{loss0}}{h_f} \quad (5.6)$$

$$h_f = \frac{q_{gen} - q_{loss1}}{T'_{w1} - T_{aw1}} \quad (5.7)$$

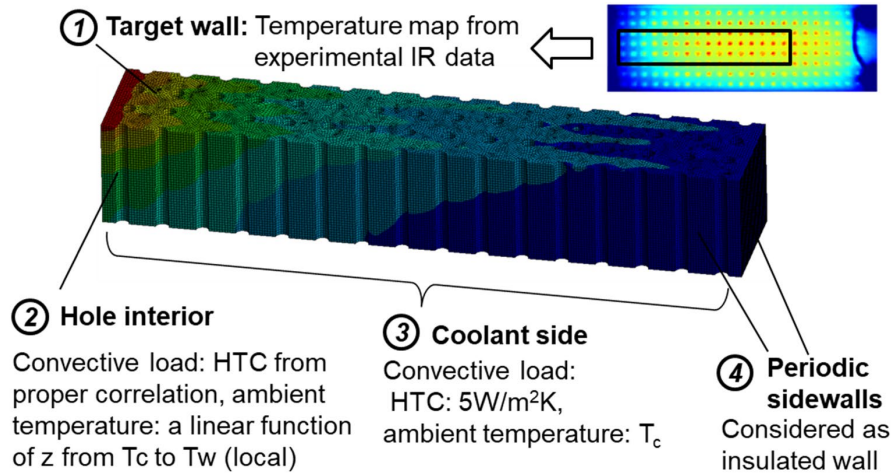


Figure 5.11 Meshing for FEA model and boundary conditions

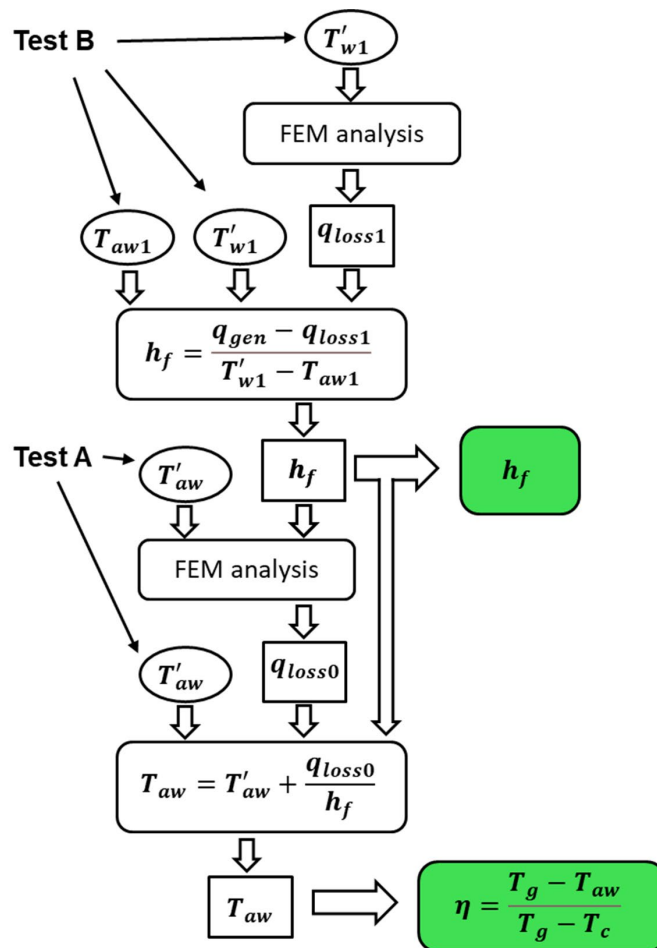


Figure 5.12 Flowchart of the post-processing to correct h_f and η

Figure 5.13 shows the calculation results of h_f and η directly from the experimental data (without conduction loss analysis) and after FEM analysis. Most evident is that the HTC values decrease after the heat-loss correction by FEM was made. In the regions between transversely adjacent holes, the HTC values drop significantly since the surface temperature is higher due to little coolant coverage, leading to higher conduction loss through the surface. The data exhibited in Fig. 5.13(b) suggest that the heat loss correction is particularly crucial for evaluating the adiabatic cooling effectiveness near the leading edge of the test section. The value of η upstream to the first row of cooling holes with heat-loss correction is much lower (nearly zero) compared to the corresponding value without the correction. This suggests that the former with heat-loss correction renders much more physically meaningful data and results.

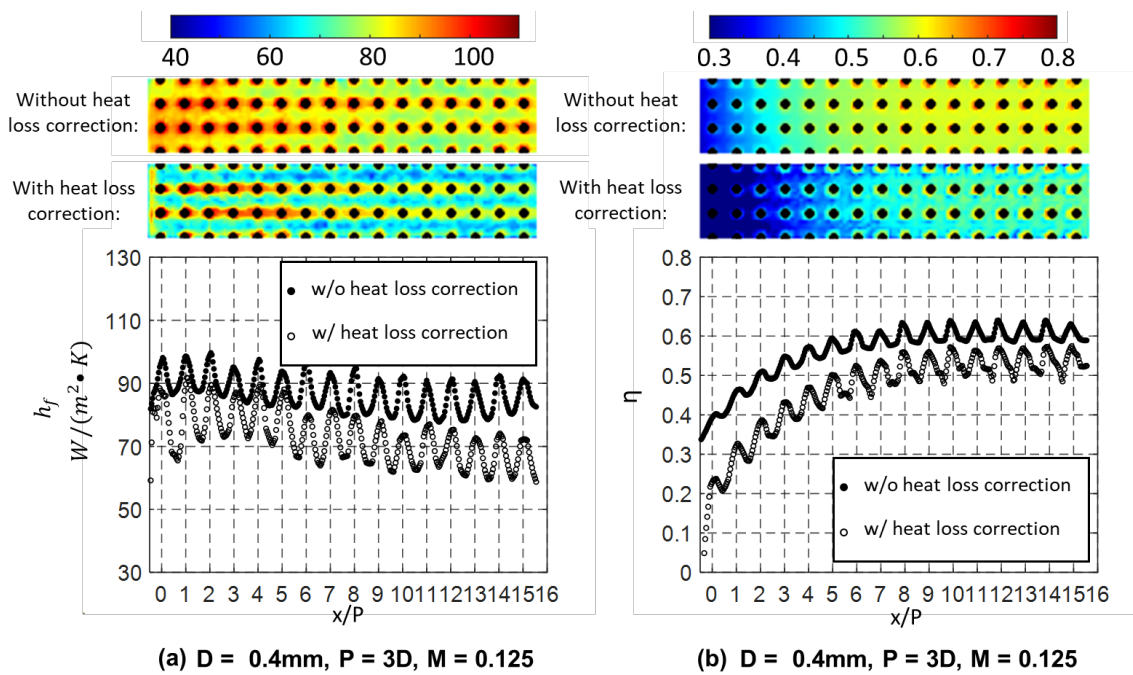


Figure 5.13 Comparison between experimental results with and without heat loss correction: (a) h_f map and spanwise averaged values; (b) η map and spanwise averaged values

The uncertainty analysis of HTC and the adiabatic cooling effectiveness can be performed based on the specs of instrument data used for the measurements of T_{aw} (0.5K), T_g (0.1K), T_c (0.1K), T_w (0.5K), q_{gen} (3%), q_{loss0} (estimated at 5%) and q_{loss1} (estimated at 5%) , as shown in Eq. (5.8) - (5.10). Accordingly, the calculated area-averaged uncertainties of adiabatic cooling effectiveness for all blowing ratios were smaller than 6.6%, while the area-averaged uncertainties of HTC were smaller than 4.3%.

$$\frac{\delta h_f}{h_f} = \sqrt{\left(\frac{1}{(T'_{w1} - T_{aw1})} \frac{\delta q_{gen}}{h_f}\right)^2 + \left(-\frac{1}{(T'_{w1} - T_{aw1})} \frac{\delta q_{loss1}}{h_f}\right)^2 + \left(\frac{q_{gen} - q_{loss1}}{(T'_{w1} - T_{aw1})^2} \frac{\delta T'_{w1}}{h_f}\right)^2 + \left(-\frac{q_{gen} - q_{loss1}}{(T'_{w1} - T_{aw1})^2} \frac{\delta T_{aw1}}{h_f}\right)^2} \quad (5.8)$$

$$\frac{\delta T_{aw}}{T_{aw}} = \sqrt{\left(\frac{\delta T'_{aw}}{T_{aw}}\right)^2 + \left(\frac{1}{h_f} \frac{\delta q_{loss0}}{T_{aw}}\right)^2 + \left(-\frac{q_{loss0}}{h_f^2} \frac{\delta h_f}{T_{aw}}\right)^2} \quad (5.9)$$

$$\frac{\delta \eta}{\eta} = \sqrt{\left(\frac{T_{aw} - T_c}{(T_g - T_c)^2} \frac{\delta T_g}{\eta}\right)^2 + \left(-\frac{1}{T_g - T_c} \frac{\delta T_{aw}}{\eta}\right)^2 + \left(-\frac{T_g - T_{aw}}{(T_g - T_c)^2} \frac{\delta T_c}{\eta}\right)^2} \quad (5.10)$$

5.2.3 Results and Discussion

The adiabatic cooling effectiveness distributions of the first 16 rows under different test conditions are shown in Fig. 5.14. The color images suggest that the adiabatic cooling effectiveness η increases as the blowing ratio M increases from 0.125 to 0.5 for all hole configurations. However, the increase of the η values from $M = 0.25$ to $M = 0.5$ is relatively insignificant as the increment from $M = 0.125$ to $M = 0.25$, implying that the excessive injection compromises the coolant efficacy for protection of the hot surface. This can be understood conceptually that when coolant covers the hot surface reaching a relatively developed regime and with a sufficient level of coolant present, injecting more coolant into the region might cool the target surface only marginally. This phenomenon was also found in many studies on the full-coverage film cooling, with an optimal blowing ratio ranging from 0.5 [147, 148] - 0.65 [149] for various cooling schemes (hole shape, hole size, injection direction, etc.). Further increase in coolant flow rate elevates the jet momentum, which generates more interaction and mixing with the mainstream flow and renders so-called the coolant “lift-off” phenomenon, resulting in little cooling enhancement.

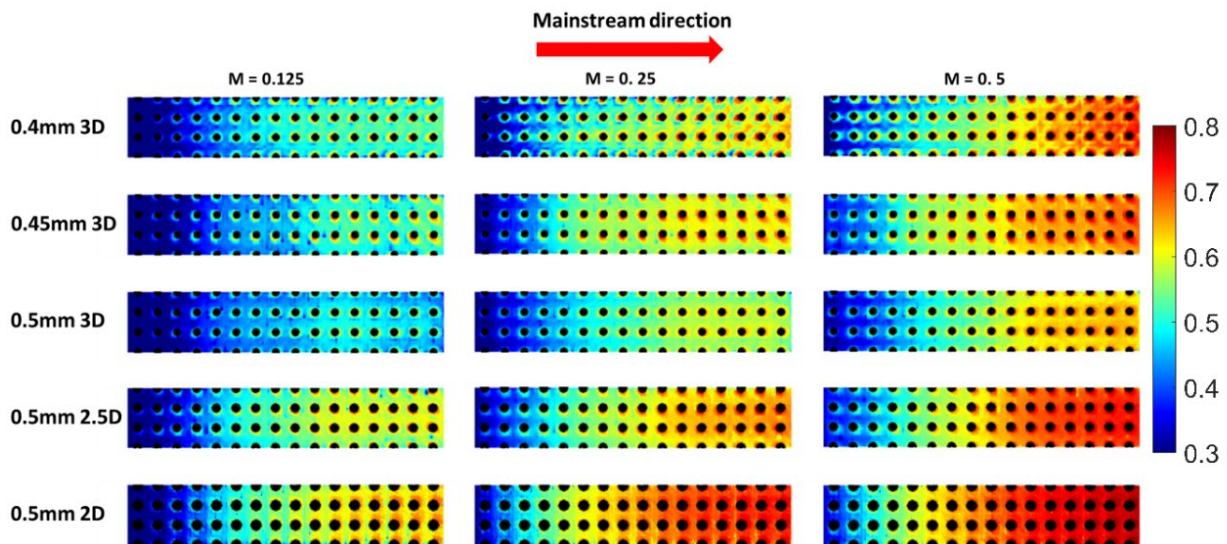


Figure 5.14 Adiabatic cooling effectiveness distributions

One significant trend shown in Fig. 5.14 (lower three rows) is that the cooling effectiveness with smaller hole spacing, i.e., smaller pitch-to-diameter ratio (P/D), is higher than that with larger values of P/D . More cooling holes or channels could be distributed on a given target surface area with a smaller hole pitch P . At a given blowing ratio, this leads to more coolant flow rate discharged over the target surface, hence higher η values overall.

Cooling hole or channel diameter, D , is also an important geometric parameter significantly affecting the cooling performance. The top three rows in Fig. 5.14 show the effects of hole diameter while the pitch is fixed at three times the hole diameter, i.e., $P=3D$. Note that for a fixed pitch or P/D ratio, the total size of the hole-opening area on a given target surface remains as a constant, unaffected by the size of the hole diameter. This also implies that, as illustrated in Fig. 5.15, number of coolant holes on a given target surface area increases for the cases with smaller hole diameters. For a given blowing ratio, the total amount of coolant flow rate introduced through all the cooling holes is constant. However, the results shown in Fig. 5.14 suggest that the case with a smaller hole size D renders a distribution of higher values in η . More cooling holes per unit area imply more coolant replenishment locally and a more uniform coolant coverage overall. This is the essence of transpiration cooling and a major advantage compared to film cooling with discrete holes of relatively large hole-diameters.

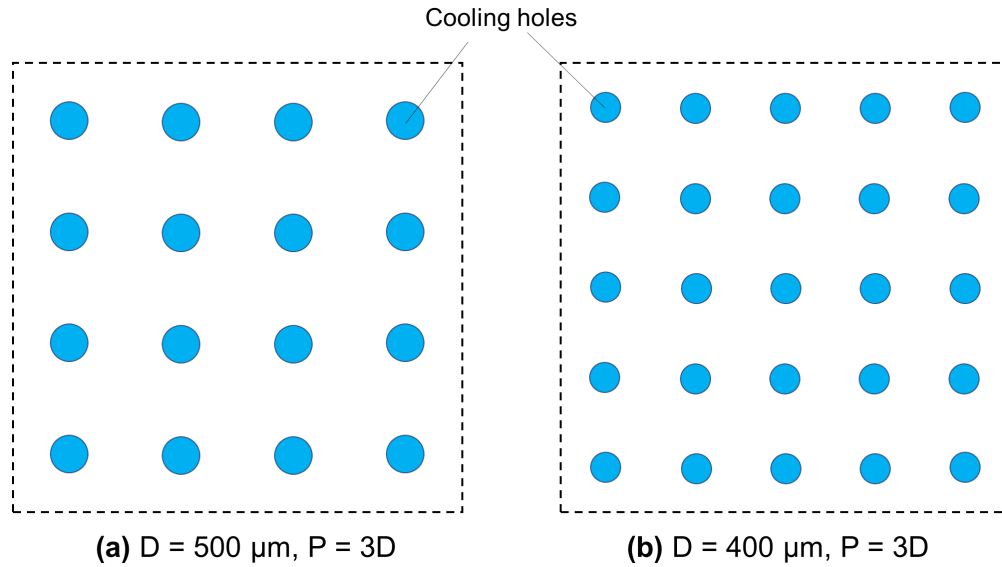


Figure 5.15 Cooling holes distribution in the same interested area

A quantitative comparison of the spanwise averaged adiabatic cooling effectiveness η with different hole sizes is presented in Fig. 5.16. Each hole configuration area containing the centered four columns of cooling channels along the mainstream direction was investigated, generating the spanwise averaged, streamwise distributed η data points. In the figure, the x-axis indicates the row number of the cooling channel arrays, and the y-axis is the adiabatic cooling effectiveness η value. We used markers with three colors in the figure to represent the three blowing ratios. The plot peaks depict the values at the hole areas, while the valleys represent the solid parts at the target surfaces. Since the IR camera can hardly capture the air temperature accurately inside the hole area, only the data points from the solid parts are used for the curve fitting as shown in the figure. As mentioned above, the η value of a smaller hole size D is slightly higher due to the larger number of hole openings distributed on the surface. Also, the effect of increasing the blowing ratio M from 0.25 to 0.5 is not as significant as the increase from 0.125 to 0.25, especially in the first few rows of the cooling hole arrays. This is because the coolant's higher momentum causes hot gas

entrainment and lift-off at a higher blowing ratio, weakening the coolant film protection. In the rear end, the slow film formation combined with the reattachment of the cooling jets enhances the cooling capability in the downstream area for the large M cases.

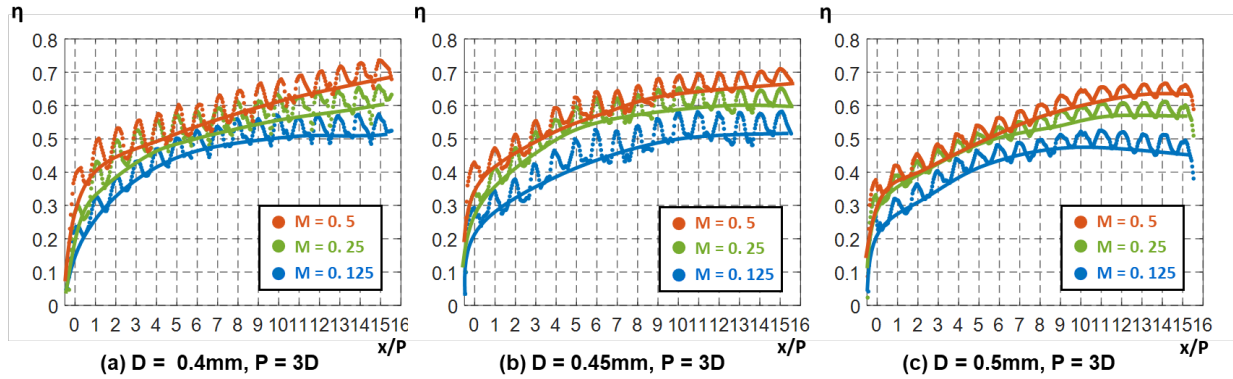


Figure 5.16 Spanwise averaged adiabatic cooling effectiveness comparison of different channel size

Figure 5.17 shows the comparison of the span-wise averaged, streamwise-resolved adiabatic cooling effectiveness for structures with various hole pitches. The values of η values increase significantly as the pitch-to-diameter ratio P decreases from 3 to 2. The η value in the relatively developed zone increases from 0.46 to 0.6 at the blowing ratio $M = 0.125$ when P drops from 3 to 2, while the increase is from 0.63 to 0.75 with $M = 0.5$. Since a smaller hole pitch P provides a larger opening area A_o , more coolant can be sent to the target surface, reducing the wall temperature substantially. A similar tendency as the previous Fig. 5.16 of the changing M is observed: the impact from $M = 0.25$ to $M = 0.5$ is not as pronounced as that from $M = 0.125$ to $M = 0.5$. Keeping increasing the coolant mass flow rate is not the most effective way to enhance cooling performance when the hot gas entrainment and coolant film lift-off occurs.

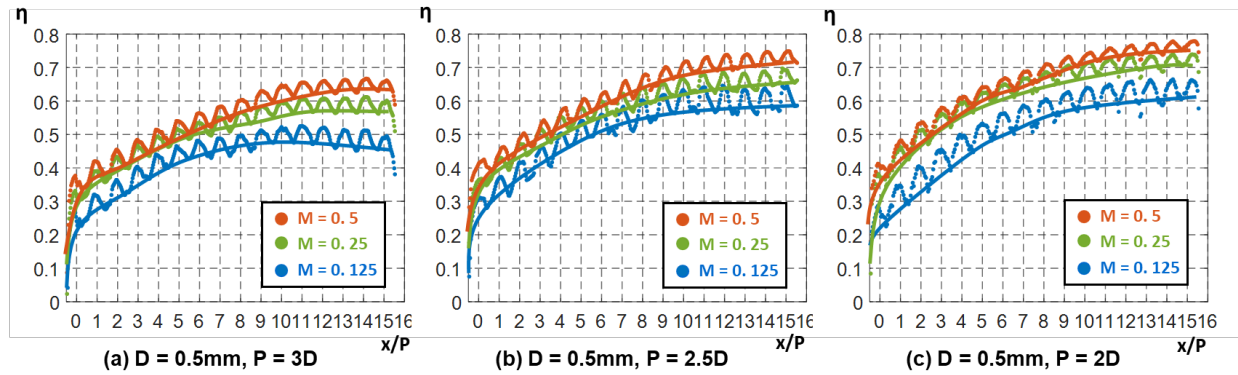


Figure 5.17 Spanwise averaged adiabatic cooling effectiveness comparison of different channel spacing

Figure 5.18 demonstrates the spanwise averaged heat transfer coefficient comparison with different hole sizes in the same zones of the target surface in the figures above. The ratio of heat transfer coefficient with coolant injection, h_f , to the values without coolant injection, h_0 , were presented in these figures. The first conclusion that can be made from the three figures is that the HTC values increase with a higher blowing ratio M . As the coolant momentum increases, more intensive turbulence mixing, vortex interaction, and more significant film detachment are built up near the target surface, hence augmenting the heat transfer rate. It can also be observed that the difference in HTC distributions of three different channel sizes D is insignificant. The same pitch-to-diameter ratio P with different D at the same blowing ratio M provides an identical mass flow rate of coolant injection per unit surface area, generating similar convective heat transfer at the film-covered surface. When $M = 0.125$, a slow increase of h_f/h_0 ratios starting from values near 1 to values around 1.2 is noticed. This trend shows that with a small amount of coolant injected, the coolant diffusion into the mainstream hardly intensifies the turbulence mixing at the target surface, leading to a slight increase of convective heat transfer rate. When the blowing ratio M increases, the h_f/h_0 ratio increase in the first few rows of channels is more pronounced. This is because the turbulence introduced by a higher

momentum of coolant jets significantly elevates the heat transfer rate during the coolant film's build-up process. Moving further downstream, the h_f/h_0 ratio gets stable at values around 2 after the film getting fully developed.

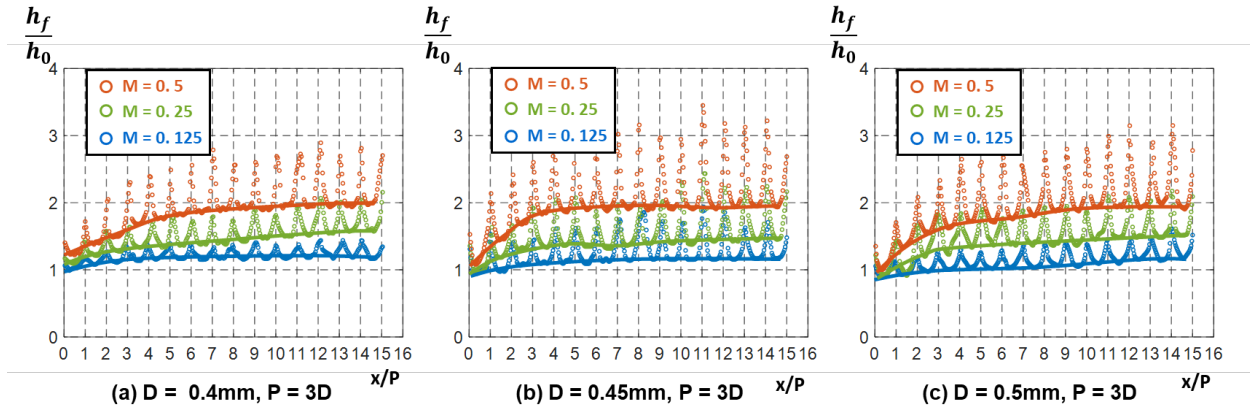


Figure 5.18 Spanwise averaged heat transfer coefficient of different channel size

Figure 5.19 exhibits the spanwise averaged HTC distributions of different hole spacings. The results revealed in the three figures suggest that the h_f/h_0 ratios increase with a smaller pitch-to-diameter ratio P . At a low blowing ratio, $M = 0.125$, the HTC ratio increases from 1.2 to 1.8 in the zone with fully developed film when lowering the P from 3 to 2. The HTC ratio increases from 1.9 to 3 when the P changes the same way (from 3 to 2) for a higher blowing ratio $M = 0.5$. One possible reason for the increase of HTC for smaller hole pitch P is that the more compact coolant jets per unit surface area escalate the interactions between adjacent jets, provoking more intensive turbulence to increase the HTC at the hot surface. In addition, the intensive turbulence generation due to more compact coolant jets prolongs the length of the developing region of the coolant film, making it longer to reach the stable value of HTC, especially for the higher blowing ratios.

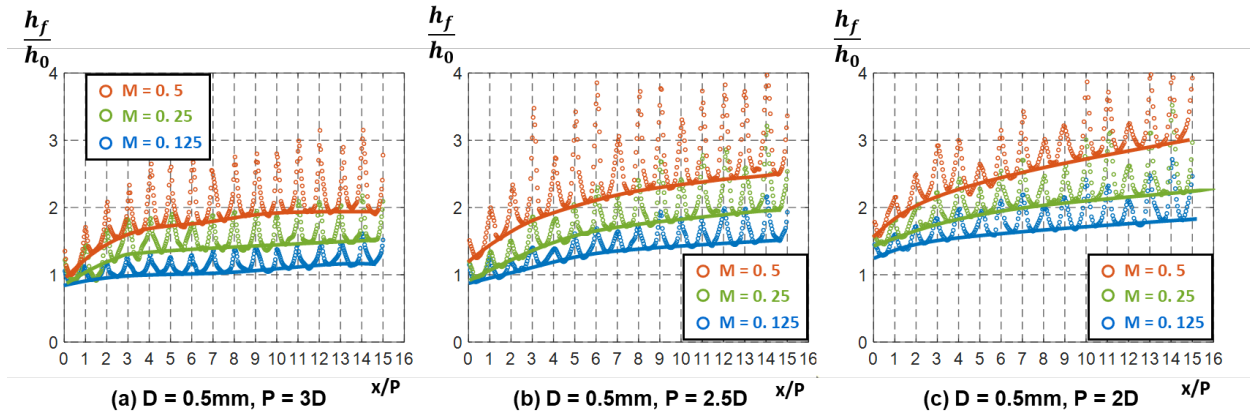


Figure 5.19 Spanwise averaged heat transfer coefficient of different channel spacing

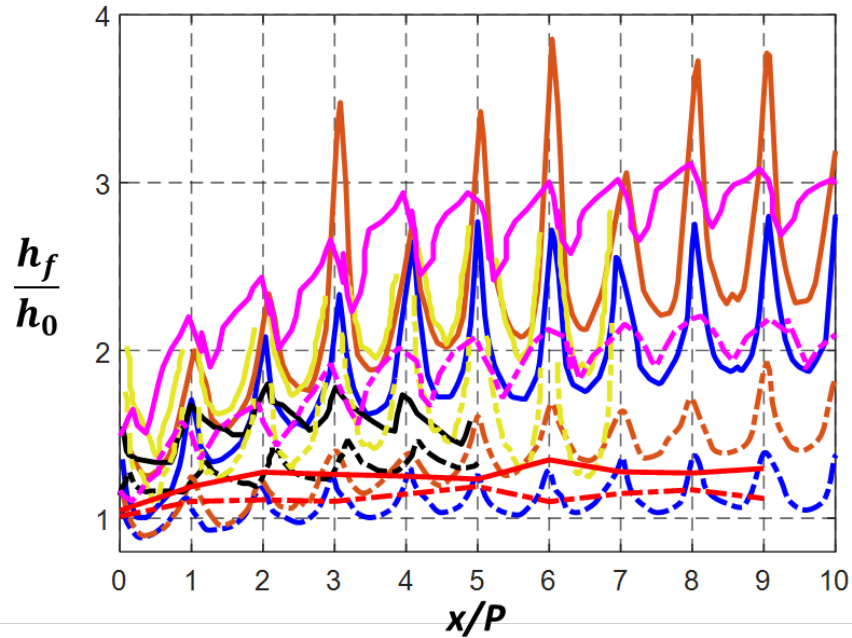
Figure 5.20 and 5.21 compare the test results to the literature data from previous publications. As mentioned earlier, few transpiration cooling studies presented the HTC and adiabatic cooling effectiveness. Thus, the published data in these figures are from multi-row film cooling studies, compared to the test data from two configurations ($D = 0.5 \text{ mm}$, $P = 3D$; $D = 0.5 \text{ mm}$, $P = 2.5D$) in this work. Metzger et al.'s work [150] provided heat transfer data at low blowing ratios from 0.1 to 0.2. Harrinton et al. [149] and Kelly and Bogard [82] investigated the HTC for blowing ratios from 0.21 to 0.65. Li et al.'s work [85] presented data for $M = 0.5$ to 2.5, while Facchini et al. [151] studied cases with blowing ratios higher than 3.

Figure 5.20 compares the h_f/h_0 ratios with the literature data in multi-row film cooling studies. For the transpiration cooling structure, the HTC ratio in the case with $D = 0.5 \text{ mm}$ and $P = 3D$ is slightly higher than 1 at the low blowing ratio $M = 0.125$, being considerably close to Metzger's data. In this case, the strong mainstream forces the low-speed coolant jets bent and diffused toward the surface, making the elevation of heat transfer rate hardly noticeable. The interactions between compact coolant ejections and crossflow of mainstream generate more turbulence near the surface in the case of $D = 0.5 \text{ mm}$ and $P = 2.5D$ with blowing ratio $M = 0.125$,

leading to a higher HTC. The HTC ratios, in this case, are close to Kelly's data at $M = 0.21$ in the first few rows and approach the data in Li's paper with $M = 0.5$. Besides, the impact of increasing the blowing ratio in transpiration cooling is more significant. The HTC ratio in the case of $P = 3D$ with a blowing ratio $M = 0.5$ is comparable to Li's data at $M = 2.5$ and Fachhini's data with $M = 3$. The HTC ratio of $P = 2.5D$ case is even higher, almost reaching the level of Fachhini's data with $M = 5$. This is because the stronger momentum of the compact cooling jets in transpiration cooling entangles with the hot gas much intensively, entraining more turbulence mixing underneath the jets to intensify the heat transfer.

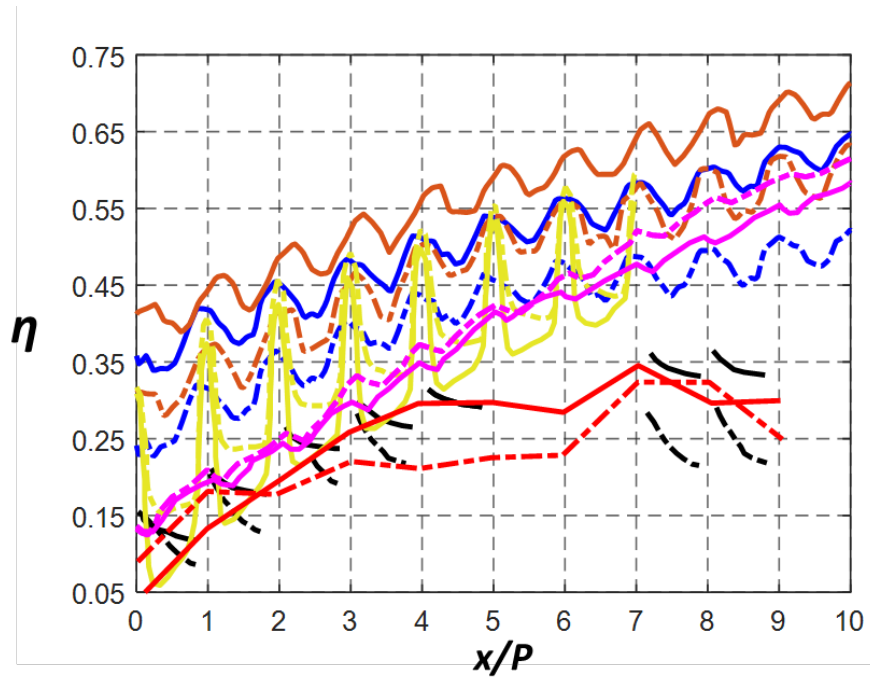
Figure 5.21 compares the η values with the literature data in multi-row film cooling studies. The adiabatic cooling effectiveness in transpiration cooling is higher than film cooling, although transpiration cooling shows higher HTC compared to film cooling. With a much smaller hole size D and hole spacing P , the transpiration cooling structure is able to provide a more uniform coolant film for better substrate protection. Also, the enhancement of η values is more significant than multi-row film cooling with growing blowing ratios M . The η values increased with higher blowing ratios, but not significantly, in the studies of the multi-row film cooling with low blowing ratios $M \leq 0.65$ (Metzger et al. [150] and Harrinton et al [149]). An additional increase in the blowing ratio from $M = 0.5$ has a negative influence on cooling efficiency in both works of Li et al. [85] and Fachhini et al. [151]. All these studies concluded that with a higher momentum of the discrete coolant jets at a high blowing ratio, the hot gas entrainment and lift-off lead to a minor improvement or even worse cooling performance. However, the packed numerous jets covering all over the wall "push" the hot gas away from the surface in transpiration cooling, even though the ratio of the momentum of each jet to that of the mainstream is similar to the film cooling case,

leaving a cooler skin area. Therefore, the impact of injecting more coolant is more pronounced for transpiration cooling structures.



Present study: - - - D=0.5mm, P=3D, M=0.125 — D=0.5mm, P=3D, M=0.5 - - - D=0.5mm, P=2.5D, M=0.125 — D=0.5mm, P=2.5D, M=0.5	Kelly and Bogard(2003): - - - D=6mm, P=7.14D, M=0.21 — D=6mm, P=7.14D, M=0.5
Metzger et al. (1973): - - - D=1.6mm, P=4.8D, M=0.1 — D=1.6mm, P=4.8D, M=0.2	Facchini et al. (2010): - - - D=1.65mm, P=7.6D, M=3.0 — D=1.65mm, P=7.6D, M=5.0
	Li et al. (2019): - - - D=2mm, P=10D, M=0.5 — D=2mm, P=10D, M=2.5

Figure 5.20 Heat transfer coefficient comparison with literature data



Present study: - - - D=0.5mm, P=3D, M=0.125 — D=0.5mm, P=3D, M=0.5 - - - D=0.5mm, P=2.5D, M=0.125 — D=0.5mm, P=2.5D, M=0.5	Harrington et al.(2001): - - - D=6mm, P=7.14D, M=0.25 — D=6mm, P=7.14D, M=0.65
Metzger et al. (1973): - - - D=1.6mm, P=4.8D, M=0.1 — D=1.6mm, P=4.8D, M=0.2	Facchini et al. (2010): - - - D=1.65mm, P=7.6D, M=3.0 — D=1.65mm, P=7.6D, M=5.0
	Li et al. (2019): - - - D=2mm, P=10D, M=0.5 — D=2mm, P=10D, M=2.5

Figure 5.21 Adiabatic cooling effectiveness comparison with literature data

6.0 Machine Learning Modeling for Cooling Effectiveness Prediction

The heat transfer test results in Chapter 4 and Chapter 5 demonstrate the high cooling potential of AM-made transpiration cooling structures. However, the dimensional characterizations in Chapter 2 show that the microchannels made by AM hardly preserve identical channel sizes the same as the target value in CAD designs. Such geometrical variations would impact the cooling performance significantly to generate various temperature distributions at the target surface. Moreover, the inhomogeneity of pore size accompanied by surface roughness would cause the smallest microchannels to clog by the dust depositions during operation. As a consequence, it is challenging to analyze the effect of the geometrical characteristics from AM theoretically. The large number of channels and the nonuniform channel size restrict the superposition model in Section 1.2.5 to predict the transpiration cooling performance. In this chapter, a three-layer neural network was developed to predict the distributions of the overall cooling effectiveness based on high-fidelity computational fluid dynamics (CFD) simulations with various channel sizes and possible blockages.

6.1 Modeling Development

6.1.1 Geometry Design

This work aims to train a neural network model to predict cooling performance based on the geometrical dimensions of the straight-hole transpiration cooling structures. In this model, the input is a hole dimension matrix representing the size of each coolant injection hole or channel, and the output is the distribution of the overall cooling effectiveness on the target surface. The channel configuration studied in this chapter simulates the AM-made structure with a designed channel diameter of 0.3mm and a hole pitch value of 3D. Thirty three rows of channels along the mainstream direction and 11 columns distributed laterally on a plate with a dimension of 32mm × 12mm × 3.2mm were investigated.

DMLS additive manufacturing generates microchannels smaller than the designed channel size with dimensional variations, as demonstrated in Chapter 2. Such offset from the designed values can be presented in a plot combining all the as-printed hole profiles from the SEM photos of the four sliced surfaces throughout the sample, as shown in Fig. 6.1(a). Each hole profile or perimeter, represented by a black line trace, was taken by a scanning electronic microscope. Here the average channel sizes (green circle) of the printed holes are significantly smaller than the designed values (red dashed circle). Also, the bandwidth of the black ring indicates the extent of variation in hole sizes. A bar chart presented in Fig. 6.1(b) represents the hole size distribution obtained based on the same SEM in Fig. 6.1(a). With a longer left tail and more values concentrated on the right side of the distribution curve, this hole size distribution is negatively skewed. A

Weibull distribution curve is used to fit this type of probability density function. All the 363 channel sizes in one input case can be calculated using this probability density curve for training.

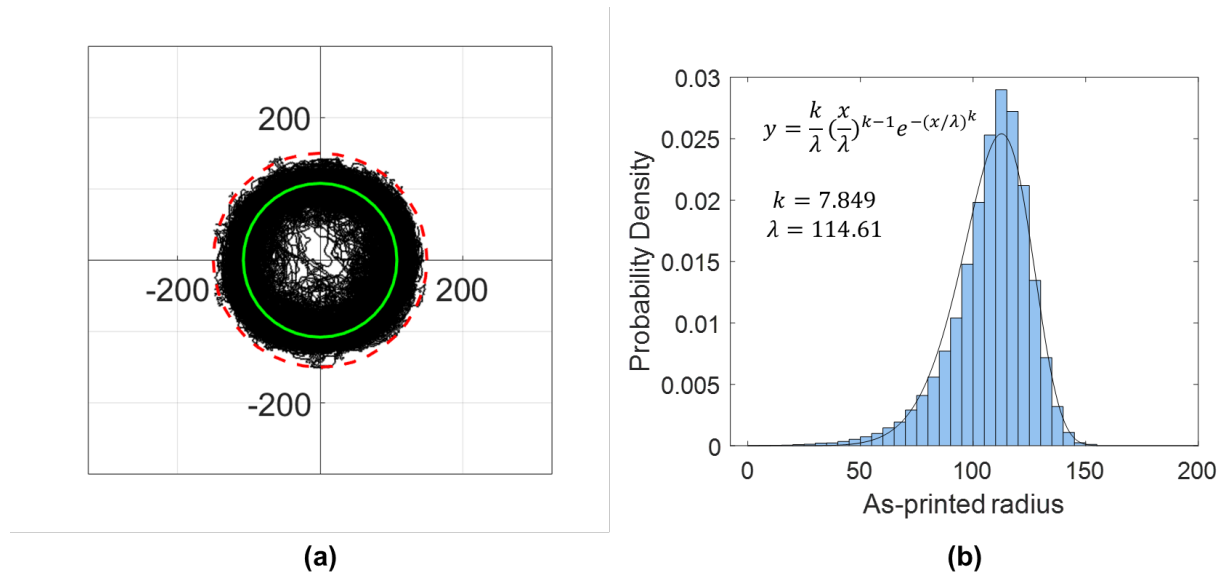


Figure 6.1 The overlapped hole profiles and corresponding radius distribution: (a) the combined hole profiles with a designed channel diameter of 0.3mm and a pitch-to-diameter value of 3; (b) the Weibull distribution curve fitting of the channel size

Sixty CFD geometries were generated with different hole size distributions to compare the cooling performance, each of which had 363 hole size values conforming to the Weibull distribution obtained in Fig. 6.1(b). Fig. 6.2 shows various hole size distribution designs at the target surface for CFD simulations. Since smaller channel sizes may cause the microchannels to be blocked during operation, 7 sub-cases with different blockage ratios from each case were designed. Fig. 6.3 shows the geometric designs for different blockage ratios of one case (case 1). Sub-case 1a indicates a 0% blockage ratio, i.e., no microchannel was clogged; sub-case 1b has microchannels with the smallest 5% channel sizes being blocked; sub-case 1c indicates the smallest 10% of microchannels got blocked, etc. The generated CFD simulation data were used to

train a fully connected neural network to predict the cooling performance. Therefore, a total of 420 CFD sub-cases completed the whole training process.

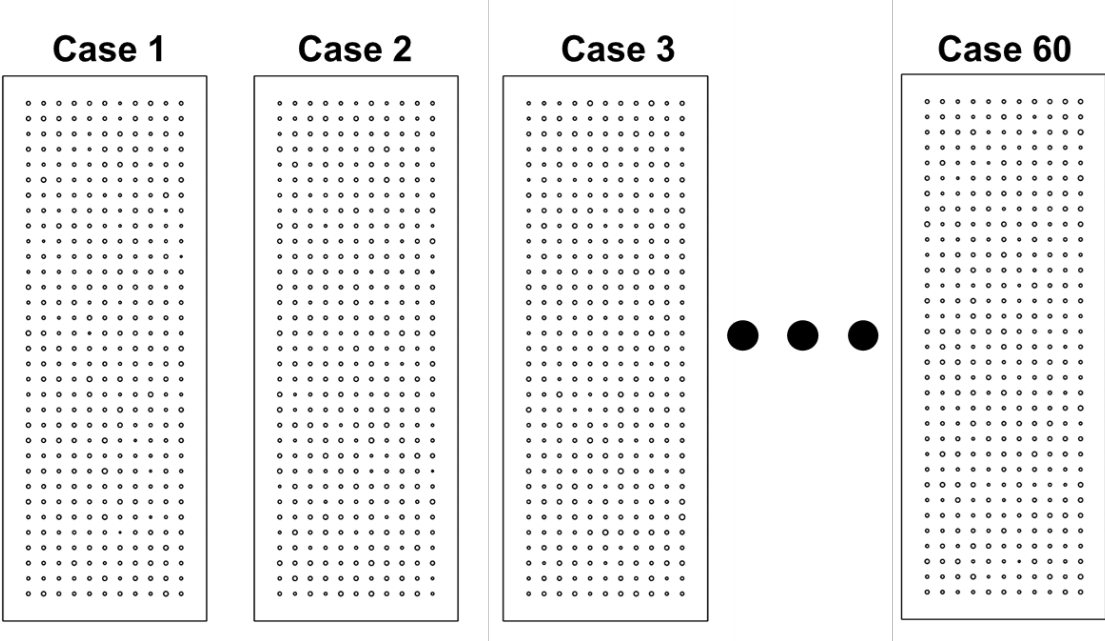


Figure 6.2 Geometric design for different hole size distributions (cases)

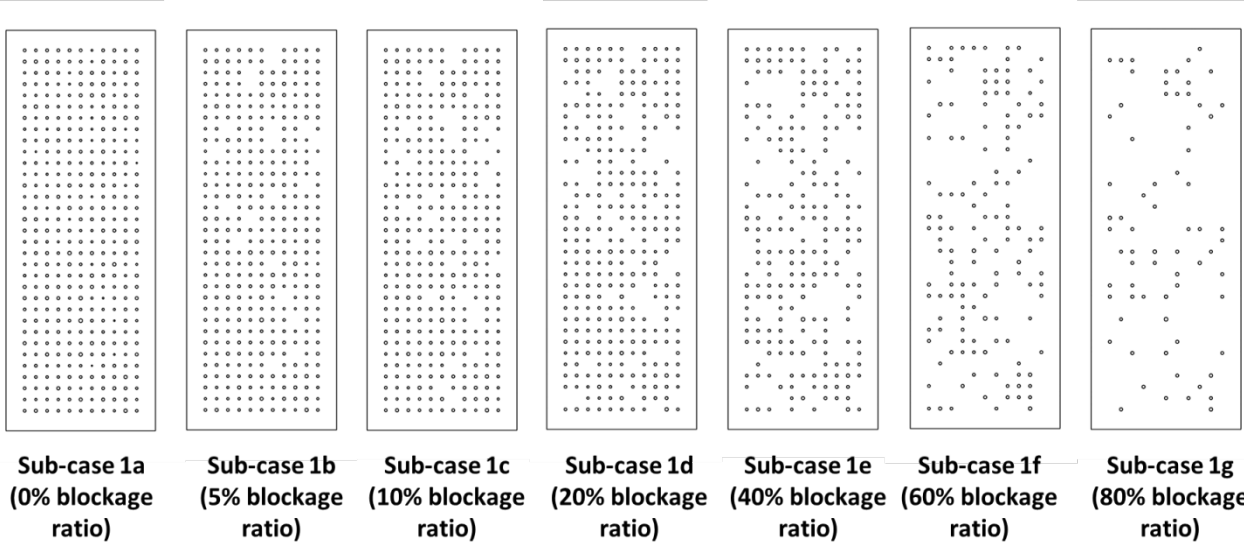


Figure 6.3 Geometric design for different blockage ratios in one case

6.1.2 CFD Simulation Setup

In this study, the training data was generated by the CFD simulations of the 420 sub-cases in total. These CFD simulations are steady-state conjugate numerical tests with both fluid domain (air) and solid domain (Inconel 718). An ANSYS Fluent solver with Reynolds Averaged Navier-Stokes (RANS) model was used in the study to capture the flow and temperature fields for all the transpiration cooling test cases. A Shear Stress Transportation (SST) $k-\omega$ model was selected as the turbulence model in this study. For each CFD test, the boundary conditions were set the same as the experimental settings in Chapter 4 as shown in Fig. 6.4. The mainstream flow was set at 323K with a constant velocity of 11m/s ($Re=98000$) and a turbulence intensity of 2%. The secondary flow was the airflow at 293K, with an injection ratio of 2.4% and a turbulence intensity of 5%.

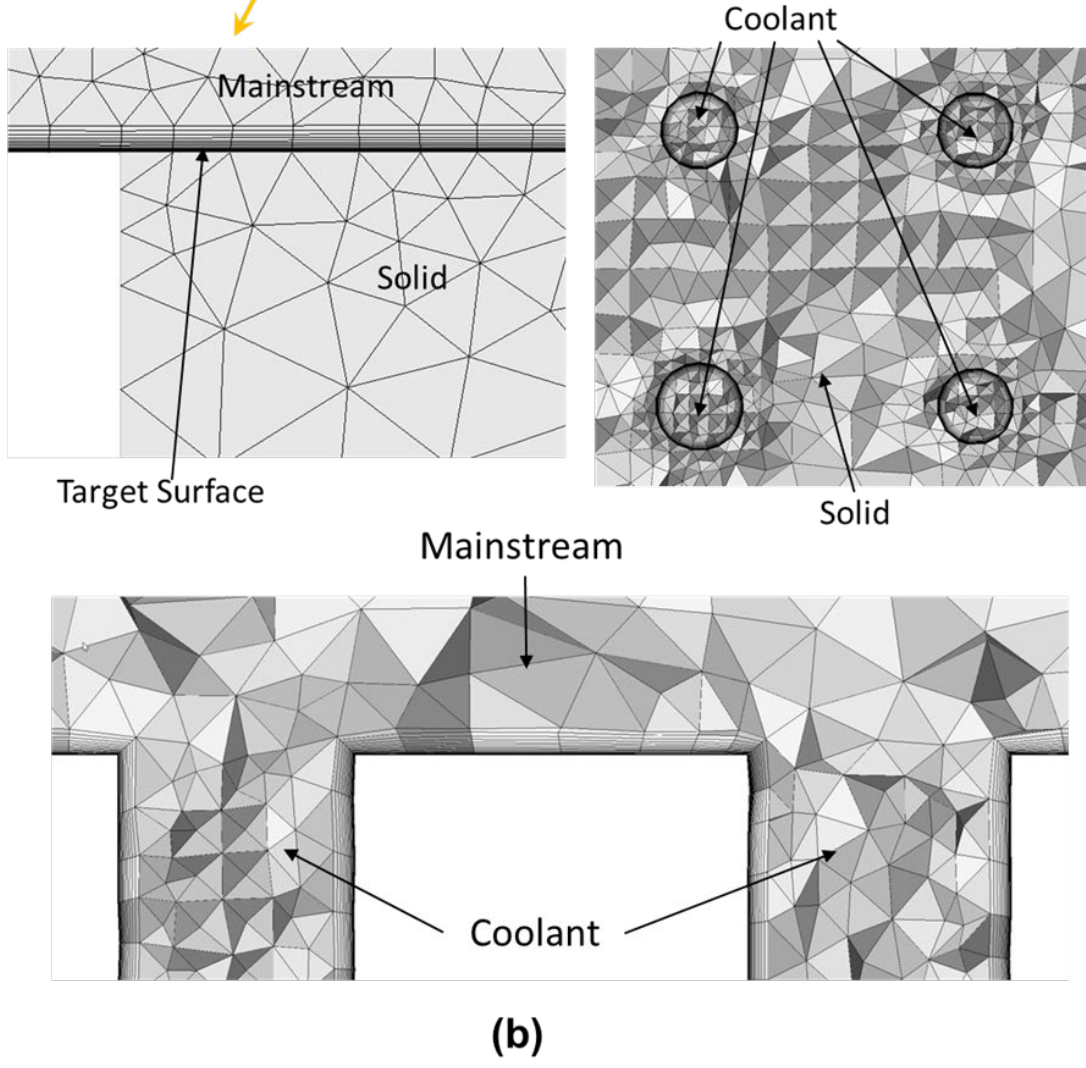
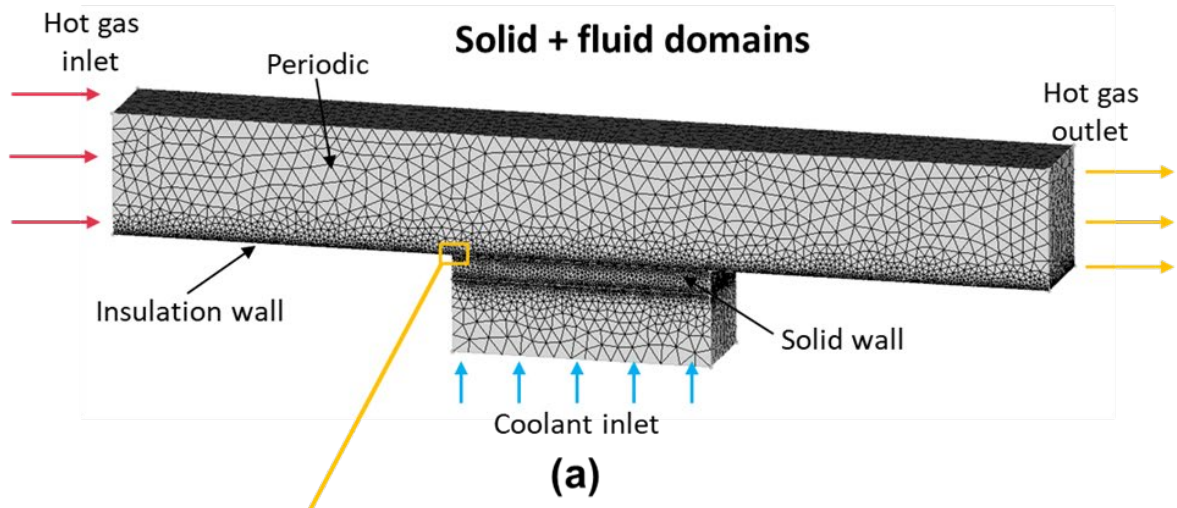


Figure 6.4 Mesh and boundary conditions: (a) Mesh overview; (b) Local views of mesh

The mesh in the two domains was generated by ANSYS ICEM CFD. The maximum size of mesh elements was 2 mm for the bulk domain, and the deviation was limited to 0.05 mm for curvatures. The prism layers were generated in the fluid domain, the first layer of which started with a thickness of 0.00125 mm for the flat walls and 0.00012 mm for the coolant-injection channel walls. Fifteen prism layers were generated from the wall surface with a growing height ratio of 1.2. The non-dimensional distance y^+ values at the target surface were all designed smaller than 1 and verified smaller than 0.8 from the simulation results, ensuring the wall functions in the turbulence model work correctly at the nodes in the first prism layer. The mesh independence tests were conducted with mesh densities at 7.5M, 9.8M, 11.5M, 13.2M, and 15.1M. The relative averaged error on pixel-wised surface temperature compared to the 15.1M case decreased from 9.2% to 1.3%. Since no significant improvement was observed from the mesh size from 13.2M to 15.1M, the present study used the mesh size ranging from 12 to 14M for the cases with 0% blockage ratios. Identical meshing settings were used for cases with larger blockage ratios.

Figure 6.5 compares the wind tunnel test results of the overall cooling effectiveness to the CFD simulation results with the same channel size distribution, which was obtained from the geometrical characterization on the top surface. The root-mean-square error (RMSE) of the pixel-wised overall cooling effectiveness of the CFD results compared to experimental data is 7.3%. Considering the errors may come from the surface roughness and irregular coolant-injection channel shape in a real-world test, the CFD result captured the main features of the temperature field at the target surface. Therefore, the CFD simulation accuracy is considered reliable to predict the cooling performance at the target surface. In the present study, the CFD simulations were used to numerically investigated 63 cases (60 for training, 3 for validation) of different hole size

distributions. As suggested before, each case comprises 7 sub-cases of different blockage ratios and the CFD simulated results of adiabatic cooling effectiveness are shown in Fig. 6.6.

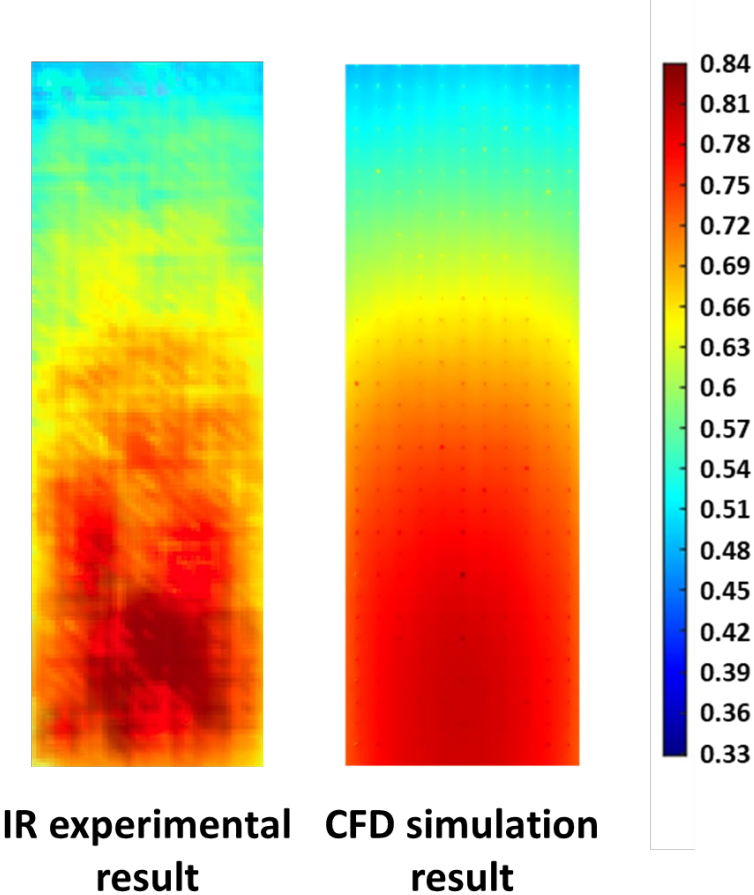


Figure 6.5 Overall cooling effectiveness comparison between experimental result and CFD simulation

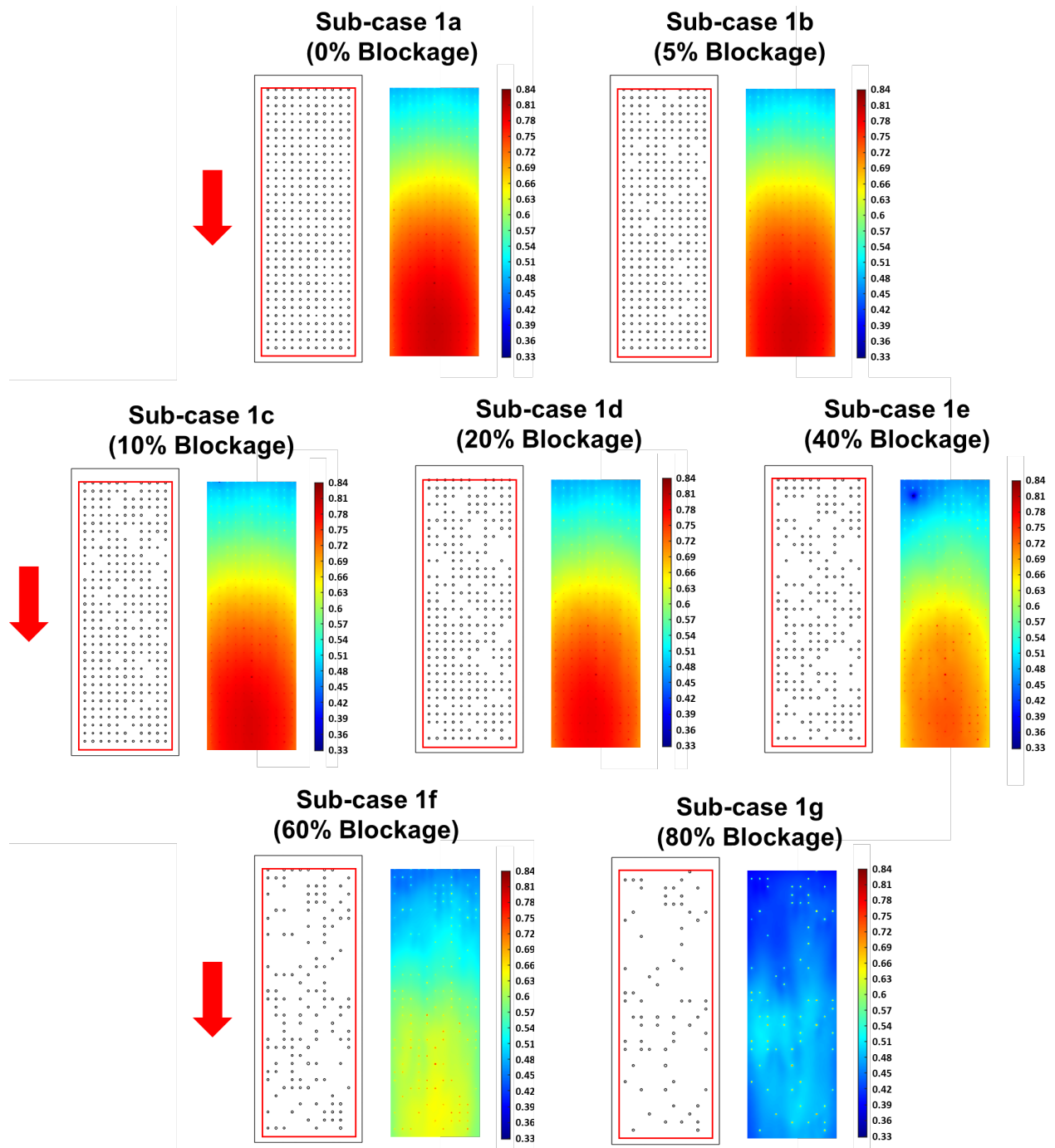


Figure 6.6 Seven sub-cases with different blockage ratios in one case

6.1.3 Modeling Architecture Design

The local temperature on the target surface is decided by many factors, such as the local film thickness, local coolant injection rate, and thermal conductivity of the porous plate, etc. These contributing factors are determined by the geometric parameters, i.e., the cooling channel locations and channel sizes in the straight-hole transpiration cooling configurations. Therefore, the present study seeks to establish a quantitative model to correlate the geometric parameters to the overall cooling effectiveness distribution. The key assumption based here is that the local temperature is governed by the weighted average of all the hole sizes distributed on the target surface. This concept is similar to Yang et al.'s work [152], which utilized a convolutional kernel to slide over the whole target surface, integrating all the impact to the target position from the neighboring area within the kernel size. Two logic states, “0” and “1”, were used in his work to represent the opened hole or clogged hole, respectively. Therefore, the model only works for the case with uniform hole size. In addition, Yang's model is restricted by the limited area of the receptive field used, i.e., the convolutional kernel size, which represents the specific neighboring area of the target location. However, the influence on the temperature at the target point comes from this neighboring area as well as holes outside. For instance, changing the hole size or the clogging condition of a hole at the end of the target surface influences the flow rate of a hole in the first row, leading to temperature change far away from the downstream. Thus, a model to cover the impact of all holes on the target surface was needed to accurately predict the cooling performance.

In this study, a three-layer model including an input layer, a fully connected intermediate layer, and a non-linear output layer, as shown in Fig. 6.7, was developed to predict the cooling performance. The input layer was the hole size distribution layer, which was a 33×11 matrix, representing the 363 channel areas, obtained by the element-wise product of the area ratio matrix

and the logic matrix given in Eq. (6.1) - Eq. (6.3). The logic function was used to introduce the clogging condition of a hole into the model. A weight matrix presented the impact of all the holes on the temperature at a specific location (pixel) with the same size as the input matrix. Therefore, for each location (pixel) in the output image, a unique weight matrix needed to be trained for the effectiveness prediction, leading to the total number of the weight matrixes, k , equal to the output image pixel number (594×198). The intermediate layer was then generated by the dot product of the vectorizations of the input matrix and the weight matrix given in Eq. (6.4). The nonlinearity was introduced into the model by a quadratic function to generate the output layer, as shown in Eq. (6.5).

$$X(i, j) = \frac{1}{A_d} (A \odot \delta)_{ij} \quad (6.1)$$

$$\delta_{ij} = \begin{cases} 0, & \text{if the hole in the } i\text{th row and } j\text{th column is clogged} \\ 1, & \text{if the hold in the } i\text{th row and } j\text{th column is open} \end{cases} \quad (6.2)$$

$$A_d = \frac{\pi}{4} D_{design}^2 \quad (6.3)$$

$$M(m, n) = \text{vec}(X)^T \cdot \text{vec}(W_k), \quad k = 1, 2, 3, \dots, 594 \times 198 \quad (6.4)$$

$$Y(m, n) = c_1(M(m, n))^2 + c_2M(m, n) + c_3 \quad (6.5)$$

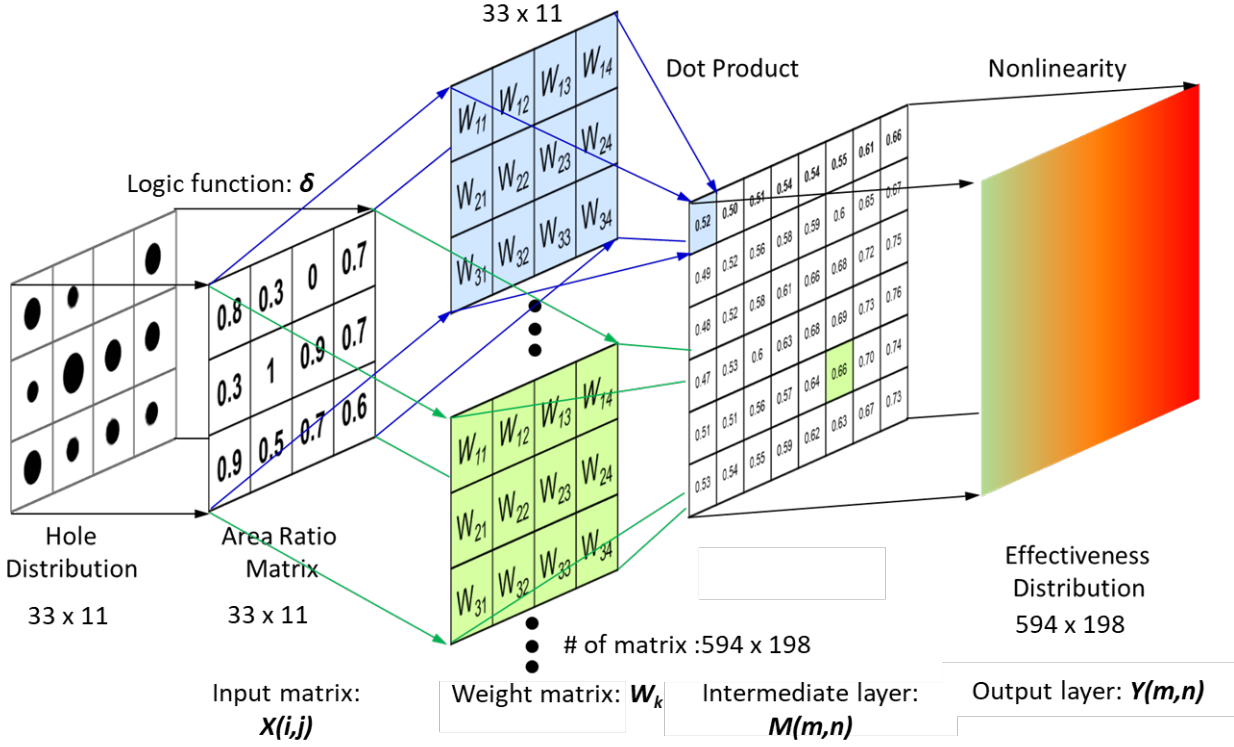


Figure 6.7 The architecture of the overall cooling effectiveness prediction model

6.1.4 Model Training

The model training is an optimization process to minimize the loss function that measures the difference between predicted cooling effectiveness Y and CFD simulation results. The loss function for each output pixel consists of two parts, the data loss and the regularization loss, as defined in Eq. (6.6). The regularization penalty term $R(W)$ is introduced into the loss function to reduce the overfitting level due to a large number of training cases by shrinking the less important weight (impact factor) of some of the holes to zero.

$$L_{m,n}(W, c_1, c_2, c_3) = \underbrace{\frac{1}{N} \sum_1^N [\varphi(m, n) - Y(m, n)]^2}_{\text{Data loss}} + \underbrace{\lambda R(W_{m,n})}_{\text{Regularization loss}} \quad (6.6)$$

$$\text{L1 regularization: } R(\mathbf{W}_{m,n}) = \sum_{i=1}^{33} \sum_{j=1}^{11} |\mathbf{W}_{m,n}(i,j)| \quad (6.7)$$

where N is the total number of CFD cases, $\boldsymbol{\varphi}(m,n)$ is the overall cooling effectiveness value of the CFD result at the pixel at the m th row and n th column, and $\mathbf{Y}(m,n)$ is the corresponding value obtained from the prediction model.

Next is the optimization process to find the set of parameters in the weight matrix \mathbf{W} and coefficients (c_1, c_2, c_3) that minimize the loss function. A Nesterov momentum technique [153] was employed for the backpropagation process. Compared to the most commonly used stochastic gradient descent (SGD) method, the Nesterov momentum algorithm introduced the momentum update into each step towards the minimum as shown in Eq. (6.8) - Eq. (6.10), making the converging process faster. Instead of directly stepping toward the gradient direction in the SGD method, each update in the iterative process moves along the direction of the previous “velocity.” With speed carried as it rolling down from the “hill,” it is more likely to update the gradient to get over some local minima or saddle points, continuing down to the global minimum.

$$\nabla_{\mathbf{W}} L_{m,n}(\mathbf{W}, c_1, c_2, c_3) = \frac{1}{N} \sum_1^N \nabla_{\mathbf{W}} [\boldsymbol{\varphi}(m,n) - \mathbf{Y}(m,n)]^2 + \lambda \nabla_{\mathbf{W}} R(\mathbf{W}_{m,n}) \quad (6.8)$$

$$\mathbf{v}_{t+1}(\mathbf{W}) = \rho \mathbf{v}_t(\mathbf{W}) - \alpha \nabla_{\mathbf{W}} L_{m,n}(\mathbf{W}, c_1, c_2, c_3) \quad (6.9)$$

$$\mathbf{W}_{t+1} = \mathbf{W}_t - \rho \mathbf{v}_t(\mathbf{W}) + (1 + \rho) \mathbf{v}_{t+1}(\mathbf{W}) \quad (6.10)$$

The training process using data from 420 CFD test results was completed by an in-house developed MATLAB program. The total computational time on a four-core (4.5GHz) CPU was around 98 hours. The average relative error in the training group converged to about 1.8% after the Nesterov momentum optimization. The trained weight matrixes and coefficients were used to predict the overall cooling effectiveness for the validation group consisted of 3 different hole

distribution cases (21 sub-cases of different blockage ratios). All the sub-cases in the validation group were unseen by the model during the training process.

6.2 Modeling Validation and Discussion

In order to evaluate the performance of the trained model, the prediction accuracy in both the training group and the validation group were analyzed. Fig. 6.8 shows the comparison of the CFD cooling effectiveness distributions and the model prediction of one case with different blockage ratios in the training group. Since the weight matrix was trained from the training group data, the predicted result for the training case was significantly accurate with an average relative error of less than 2%. The generated distribution of the overall cooling effectiveness matched the CFD results without significant difference. This demonstrates the capability of the model for generating high-accuracy data on the training set.

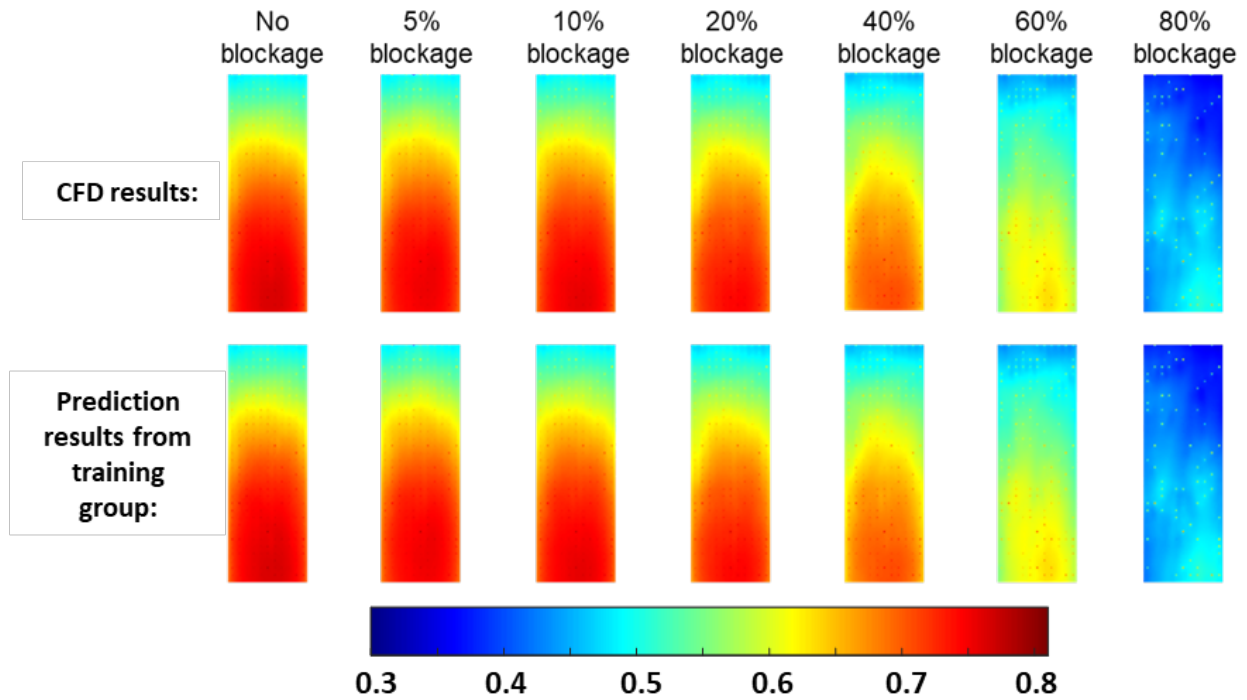


Figure 6.8 Model performance in the training set

While the model accuracy in the training set is desirable, the prediction accuracy for the unknown data in the testing/validation set is more critical. Fig. 6.9 demonstrates the prediction results in the validation group when using different cases to train the model. The first row of images presents the overall cooling effectiveness distributions of the CFD simulation results as the ground truth. For comparison, the remaining rows are the prediction results from models trained by different numbers of CFD cases. Clearly shown here is that the prediction results are getting closer to the CFD simulated values or “ground truth” as the size of the training cases increases. Although the model is not capable of capturing the precise positions of the cooling holes, the overall distributions at the target surface are quite close to the ground truth. A notable feature exhibited in Fig 6.9 is that an increase in the blockage ratio renders lower prediction accuracy. As the number of clogged holes increases, the cooling performance is getting more sensitive to the condition

change of the likely reduced number of individual holes. A hole that is open or clogged would impose more influence on the characteristics of cooling effectiveness, in both magnitude and distribution, over the entirety of the target surface.

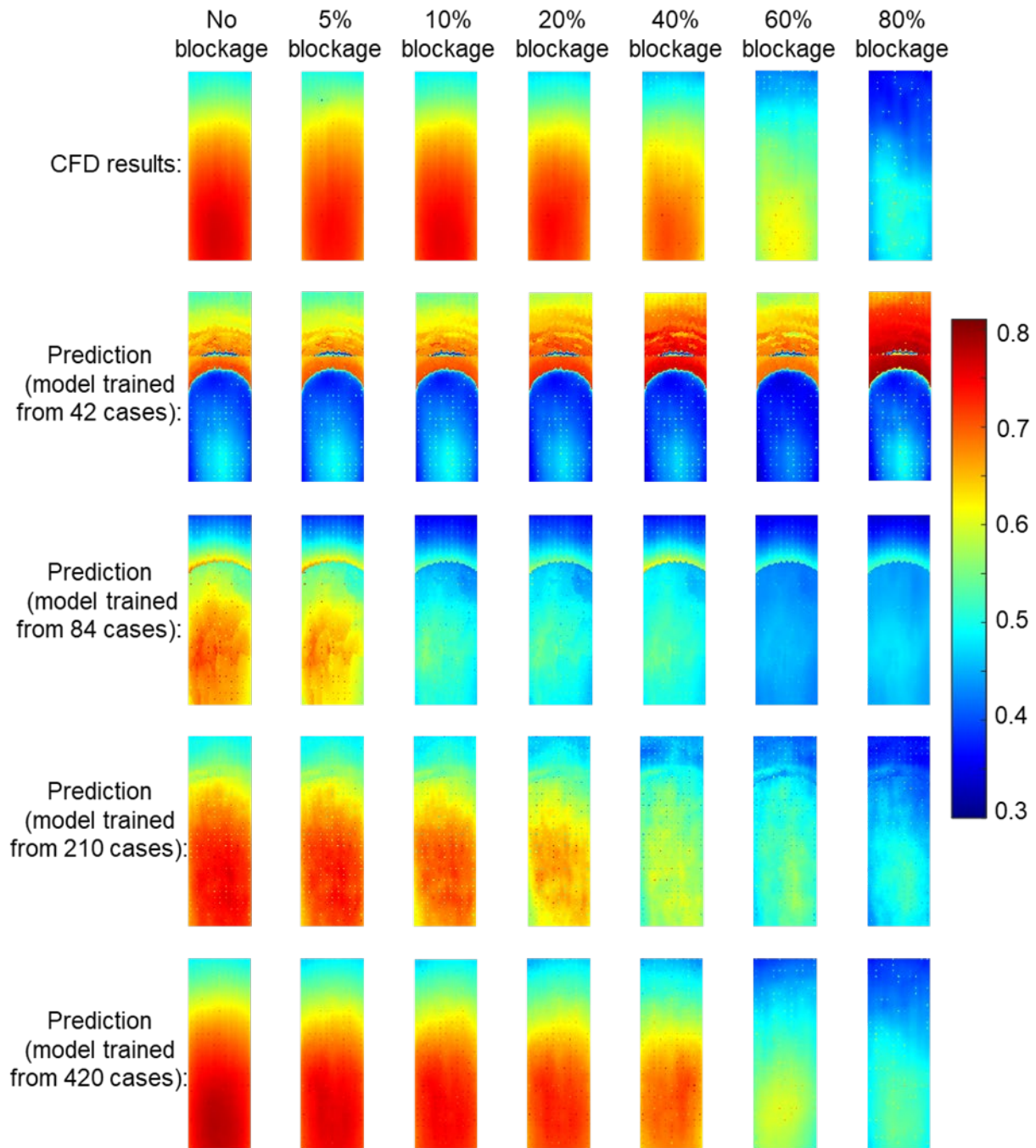


Figure 6.9 Model predictions trained from different quantities of the training cases

Figure 6.10 demonstrates the spanwise-averaged cooling effectiveness distributions of the seven subcases in the validation group with different clogging ratios. The solid blue lines show the data calculated from CFD simulations, and the asterisks in orange are the predicted data. It is evident that the trained model is capable of capturing the trend of the overall cooling effectiveness along the mainstream direction for all the subcases. In most cases, the prediction accuracy at the downstream is lower than the upstream due to the errors from the upstream holes being accumulated. The model works better for the subcases with lower blockage ratios as mentioned above, because the effectiveness distribution is rather sensitive to the hole condition change at a high blockage ratio. In addition, the increased errors for the high blockage ratio subcases are possibly caused by the training data imbalance. The CFD results in Fig. 6.9 for subcases with relatively low clogging ratios, say 0-40% blockage, present similar φ characteristics in overall magnitude and local distribution. This likely makes the prediction model more familiar with the subcases with more opening holes, resulting in more agreeable predictions toward the low blockage ratio subcases.

Figure 6.11 shows a comparison of the averaged prediction accuracy among different subcases in the validation group when using different amounts of CFD cases to train the model. The definition of the averaged prediction accuracy is given by Eq. (6.11). The prediction accuracy for all subcases increases as more CFD test results were used for training. It reaches higher than 93% for the subcases with a low blockage ratio ($\leq 40\%$) based on 420 CFD simulations. For the subcases with a higher clogging ratio ($\geq 60\%$), the prediction accuracy drops to less than 90%. For the subcases with higher blockage ratios, the trend for better prediction continues to increase even the size of the training set reaches 420, hence the model accuracy can be further improved by using more training data.

$$PA = \left[1 - \frac{1}{594 \times 198} \sum_{m=1}^{594} \sum_{n=1}^{198} \left(\frac{|\varphi(m, n) - Y(m, n)|}{Y(m, n)} \right) \right] \times 100\% \quad (6.11)$$

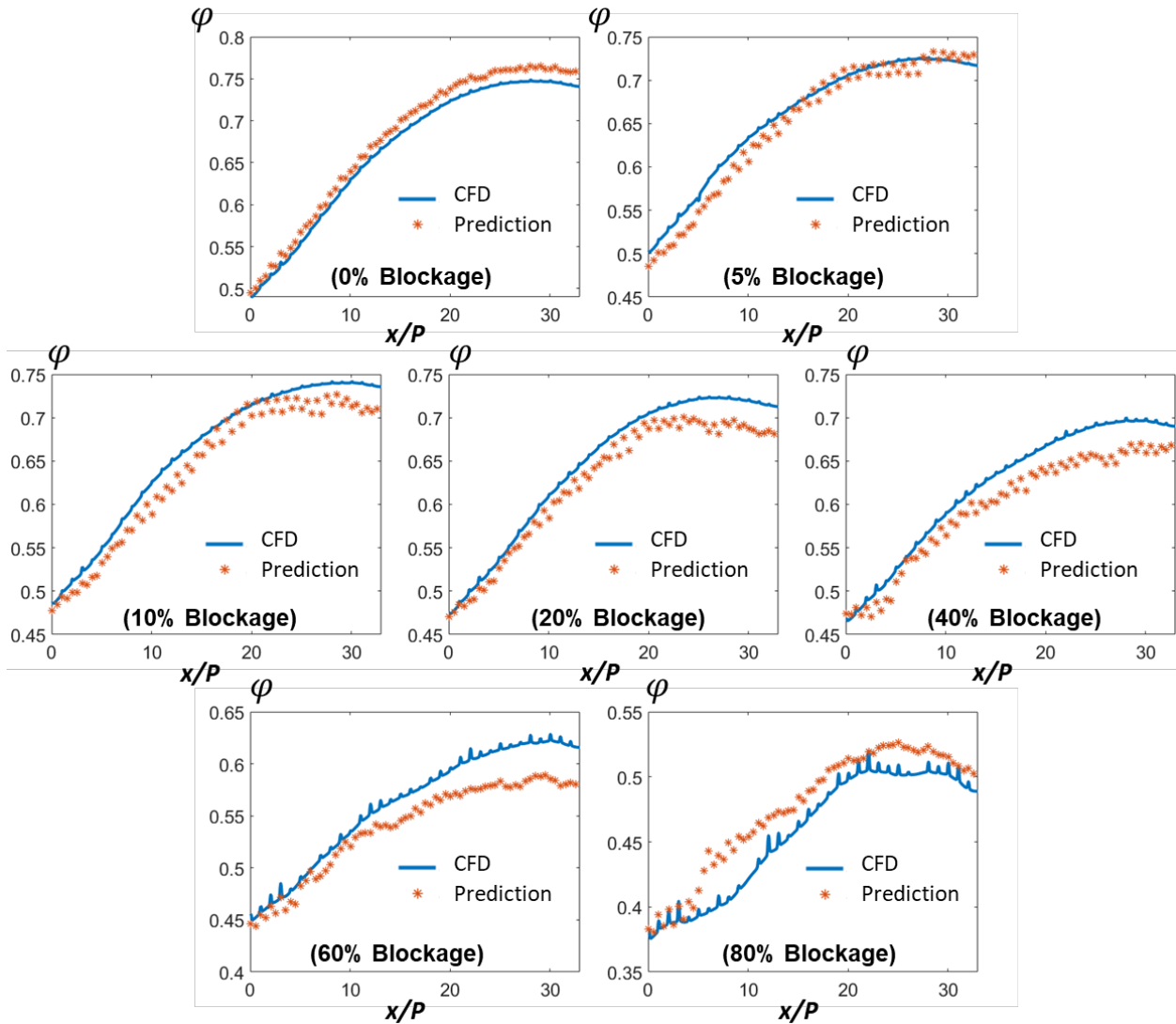


Figure 6.10 Lateral averaged cooling effectiveness comparison

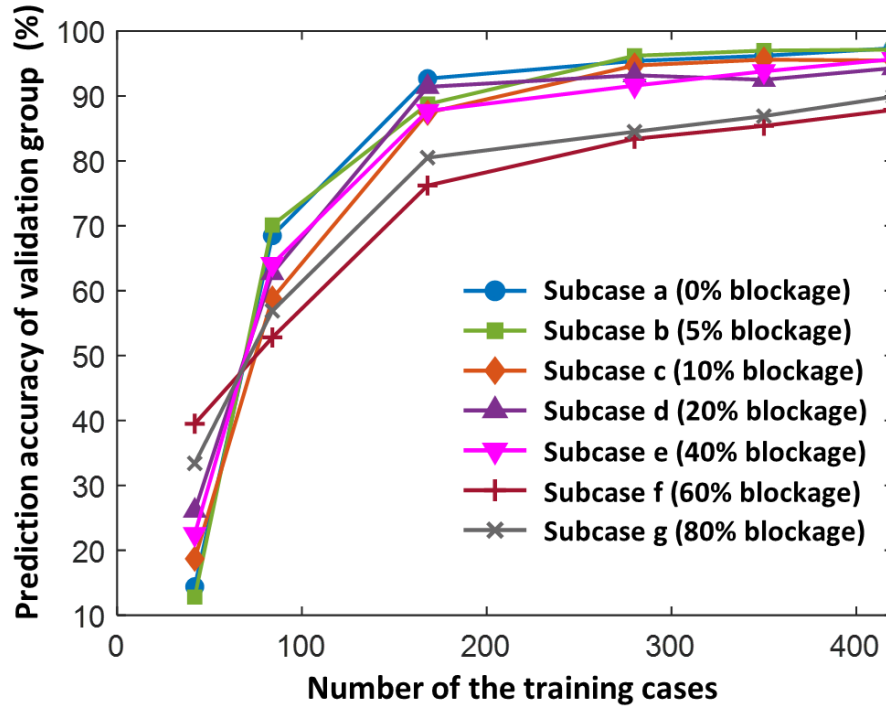


Figure 6.11 Averaged prediction accuracy for subcases with different blockage ratios

Figure 6.12 shows a comparison between the CFD results and the model prediction values for all the pixels in the validation group. Fig. 6.12 (a) exhibits the performance of Yang et al.'s convolution model for predicting uniform-hole-size distributions and Fig. 6.12 (b) shows the present results. A comparison between Fig. 6.12 (a) and (b) suggests that the present model gives a lower error margin by 15% to 20%. In the present work, most of the data points with a larger error ($>15\%$) locate in the r with small overall cooling effectiveness values (< 0.5), which are mostly associated with the subcases of high blockage ratios. Generating more CFD cases with high blockage ratios for training may rebalance the training set for further improving the prediction results, as suggested earlier.

In summary, the three-layer neural network model developed in this study is capable of predicting the cooling effectiveness, in both magnitude and local distribution, over a target surface

equipped with a large number of transpiration cooling holes of various hole sizes and blockage ratios. This effort could lead to a better understanding toward the impacts of geometric variations on the transpiration cooling performance and design optimization for cooling components made by AM. There are two factors that compromise the efficacy of the present prediction model: (1) uncertainty in capturing the locations of the opening holes, and (2) lack of sensitivity in mitigating the highly clogged cases. Potential remedies may include the utilization of improved training quality by balancing the training data set and developing a more advanced neural network, machine learning algorithms.

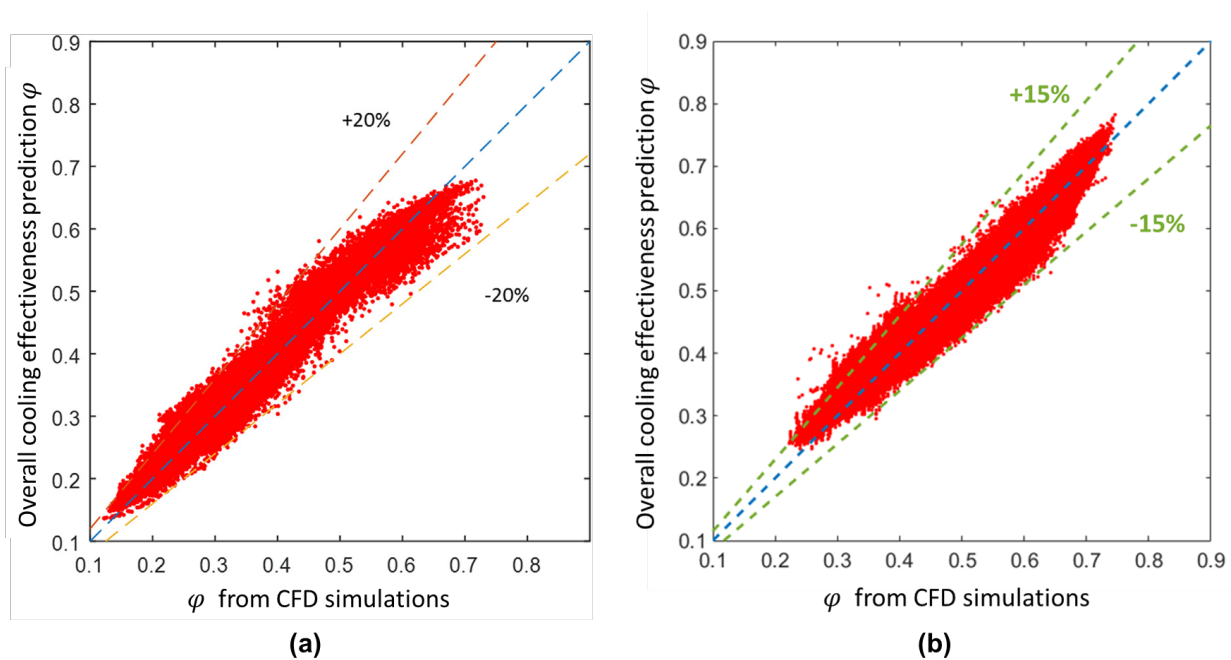


Figure 6.12 Pixel-wised predictions in the validation group of the two machine learning models: (a) Yang's model; (b) The model developed in this study

7.0 Conclusions and Future Work

This dissertation presents studies to address the challenges in dimensional metrology, surface improvement, thermo-fluid investigation, and prediction modeling for AM transpiration cooling structures. Geometric design and sample fabrication, geometric characterization, surface quality improvement, experimental heat transfer methodology and procedures, micro-lithography for surface heater fabrication, and machine learning model development were established and documented via this work. The major achievements are presented in the following section.

7.1 Major Accomplishments

1. SEM geometric characterization and followed-up surface quality improvement:

This work proposed an SEM characterization combined with the image segmentation technique for dimensional metrology and analysis of microchannels made by AM. This method addressed the limitations (low detection resolution, sample size limitations, and noises generated by x-ray diffractions) of the state-of-art micro-CT scan for geometric characterizations, making it possible to characterize multi-row transpiration cooling structures accurately. Nine straight-hole transpiration cooling configurations were characterized and analyzed statistically. The results showed that the channel sizes of the printed specimens were smaller than the designed values. The ratios of the as-printed channel size to the objective value varied from 0.65 to 0.85. Based on the relationship between the as-printed channel size and the designed value, samples could be redesigned to a larger channel size to compensate for the “shrinkage” during the printing process.

This CAD-based compensation method could produce samples with R_p/R_o ratio close to 1, making it possible to study the impact of the geometric dimension on the cooling performance in Chapter 4. This study also employed the ECP process to improve the surface qualities. The Ra and C values of the ECP polished sample decreased more than 50% from the originally designed sample, which means a significant surface quality improvement was achieved by redesigning the channel size and the ECP process.

2. Transpiration cooling effectiveness investigation: Five AM transpiration cooling structures, i.e., two straight round microchannel structures, one compact sphere packing porous media, one woven wire matrix structure, and one blood-vessel microchannel structure, were tested in the wind tunnel heat transfer experiments. The transpiration cooling effectiveness of these structures was compared to that of the state-of-art film cooling structure made by the same DMLS technique. The test results showed a significantly higher cooling potential of transpiration cooling than film cooling, benefiting from AM fabrication's complex internal structures. The study of the impact from the geometric parameters indicated that the porosity was not the only parameter influencing the thermo-fluid performance. With the capability to fabricate channel sizes close to the desired values using CAD compensation, nine straight-hole configurations were designed and manufactured to investigate the impact of porosity and internal surface area on transpiration cooling effectiveness. The quantitative analysis showed that the compactness value defined as the ratio of the inner solid-fluid interface area to the volume was a more decisive geometrical factor than porosity to evaluate the overall cooling performance. A significant increasing trend of the cooling efficiency was observed with a growing compactness value of the transpiration cooling structures.

3. Heat transfer coefficient investigation: Few studies experimentally investigated the heat transfer coefficient at the target surface of the transpiration cooling structures due to the massive number of ejection holes within a small area. This study employed a micro-lithography technique to deposit the surface heater directly on top of the transpiration cooling target surface without blocking the outlets, providing a stable and uniform heat flux during the heat transfer test. A steady-state infrared thermography method was used to capture both HTC and adiabatic cooling effectiveness. The test results showed that the HTC distributions were similar for the structures with varying channel sizes but the same channel pitch. A smaller channel pitch led to a higher HTC due to higher turbulence intensity generated by more interactions between adjacent jets. The HTC distribution at the transpiration cooling surface was close to that without coolant injection at a low blowing ratio at 0.125, which meant the small amount of the coolant injection hardly intensified the turbulence mixing at the target surface. A smaller hole pitch resulted in higher adiabatic cooling effectiveness, demonstrating that more compact coolant jets could considerably lower the film temperature.

4. Machine learning model to predict the cooling performance: A three-layer neural network model in this study was developed from Yang et al.'s convolutional model. A fully connected layer instead of the convolutional layer in Yang's model was used to cover the impact of all the holes at the target surface. A hole area ratio matrix representing the hole size variation combined with a logic function indicating clogging conditions was utilized as the input layer for the model. The model trained from 420 CFD cases could capture the non-uniformity of the hole sizes, generating overall cooling effectiveness distributions with an average error within 7% for the low blockage ratio ($\leq 40\%$) and 12% for the high blockage ratio ($> 40\%$) subcases in the

validation group. The model developed in this work outperformed Yang's model with higher accuracy.

7.2 Future Work

The present work studied two major aspects, the geometric metrology and the thermo-fluid performance of the AM transpiration cooling structures. Further investigations may be directed towards a thorough study of the effect of the geometric characteristics on the cooling performance and the development of more advanced machine learning models for better geometric design to enhance the cooling capabilities.

Impact of the surface roughness on cooling performance: As discussed in Chapter 2 and Chapter 3, DMLS additive manufacturing generates microchannels with size variations and surface roughness. This work focused only on the study of the effect of the channel size variations on cooling efficiency. The surface roughness's influence is more complicated, as the rough surface enhances the convective heat transfer inside the channel and generates various vortexes escalating the turbulence intensity in the coolant ejections. Therefore, further studies on the impact of surface roughness are desirable to evaluate the transpiration cooling accurately. The equivalent sand grain roughness model is possibly used in future numerical studies on surface roughness. The ECP technique discussed in Chapter 3 can be applied to the AM transpiration cooling structures on different surface roughness levels for the experimental studies.

Geometric design for better cooling performance: This work investigated straight hole configurations of transpiration cooling. The compactness of the cooling structures impacted

cooling efficiency substantially as discussed in Chapter 4. Therefore, more compact geometries can be designed with different channel shapes, injection directions, channel turnings, and channel distributions, etc. The net heat flux reduction for various geometrical designs could be evaluated experimentally to select the most efficient cooling structures using the IR thermography technique and the surface heater fabrication method introduced in Chapter 5.

More advanced machine learning model for cooling predictions: The model developed in this study showed some difficulties in precisely capturing all the cooling features, especially for the highly clogged cases. Introducing more training cases with high blockage ratios may improve prediction accuracy. Also, a deeper neural network such as ConvNets, U-net, and fully convolutional network in the computer vision field may be beneficial to the “translation” task to convert the geometric characteristics into cooling performance results. Moreover, a machine learning model working reversely than the one in this study that identifies 2-D geometric characteristics based on the cooling performance at the target surface would be a useful extension to this work, helping engineers diagnose possible blockage locations during the operation.

Bibliography

- [1] Chyu, M.K. and S.C. Siw, *Recent advances of internal cooling techniques for gas turbine airfoils*. Journal of Thermal Science and Engineering Applications, 2013. **5**(2).
- [2] Yang, L., Z. Min, P.N. Sarwesh, and M.K. Chyu, *Numerical optimizations of hybrid-linked jet impingement heat transfer based on the genetic algorithm*. Numerical Heat Transfer, Part A: Applications, 2016. **70**(11): p. 1179-1194.
- [3] Yang, L., S.N. Parbat, Z. Min, and M.K. Chyu, *Effect of topology on hybrid-linked jet impingement*. International Journal of Heat and Mass Transfer, 2017. **108**: p. 671-679.
- [4] Siw, S.C., M.K. Chyu, V.G. Karaivanov, W.S. Slaughter, and M.A. Alvin. *Influence of internal cooling configuration on metal temperature distributions of future coal-fuel based turbine airfoils*. in *Turbo Expo: Power for Land, Sea, and Air*. 2009.
- [5] Bunker, R.S. *Gas turbine cooling: moving from macro to micro cooling*. in *Turbo Expo: Power for Land, Sea, and Air*. 2013. American Society of Mechanical Engineers.
- [6] Goldstein, R.J., *Film cooling*, in *Advances in heat transfer*. 1971, Elsevier. p. 321-379.
- [7] Bunker, R.S. *Film cooling: breaking the limits of diffusion shaped holes*. in *TURBINE-09. Proceedings of International Symposium on Heat Transfer in Gas Turbine Systems*. 2009. Begel House Inc.
- [8] Bunker, R.S., *A review of shaped hole turbine film-cooling technology*. J. Heat Transfer, 2005. **127**(4): p. 441-453.
- [9] Han, J.-C. and A. Rallabandi, *Turbine blade film cooling using PSP technique*. Frontiers in Heat and Mass Transfer (FHMT), 2010. **1**(1).
- [10] Goldstein, J.I., D.E. Newbury, J.R. Michael, N.W. Ritchie, J.H.J. Scott, and D.C. Joy, *Scanning electron microscopy and X-ray microanalysis*. 2017: Springer.
- [11] Reed, S.J.B., *Electron microprobe analysis and scanning electron microscopy in geology*. 2005: Cambridge University Press.
- [12] Vedula, R. and D. Metzger, *A method for the simultaneous determination of local effectiveness and heat transfer distributions in three-temperature convection situations*. gatu, 1991.
- [13] Sellers Jr, J.P., *Gaseous film cooling with multiple injection stations*. AIAA Journal, 1963. **1**(9): p. 2154-2156.

- [14] Lefebvre, L.P., J. Banhart, and D.C. Dunand, *Porous metals and metallic foams: current status and recent developments*. *Advanced engineering materials*, 2008. **10**(9): p. 775-787.
- [15] Banhart, J., *Manufacturing routes for metallic foams*. *Jom*, 2000. **52**(12): p. 22-27.
- [16] Qin, J., Q. Chen, C. Yang, and Y. Huang, *Research process on property and application of metal porous materials*. *Journal of Alloys and Compounds*, 2016. **654**: p. 39-44.
- [17] Oh, I.-H., N. Nomura, N. Masahashi, and S. Hanada, *Mechanical properties of porous titanium compacts prepared by powder sintering*. *Scripta Materialia*, 2003. **49**(12): p. 1197-1202.
- [18] Liu, P., G. He, and L. Wu, *Fabrication of sintered steel wire mesh and its compressive properties*. *Materials Science and Engineering: A*, 2008. **489**(1-2): p. 21-28.
- [19] Xu, G., Y. Liu, X. Luo, J. Ma, and H. Li, *Experimental investigation of transpiration cooling for sintered woven wire mesh structures*. *International journal of heat and mass transfer*, 2015. **91**: p. 898-907.
- [20] Gu, D. and Y. Shen, *Processing conditions and microstructural features of porous 316L stainless steel components by DMLS*. *Applied Surface Science*, 2008. **255**(5): p. 1880-1887.
- [21] Balla, V.K., J. Soderlind, S. Bose, and A. Bandyopadhyay, *Microstructure, mechanical and wear properties of laser surface melted Ti6Al4V alloy*. *Journal of the mechanical behavior of biomedical materials*, 2014. **32**: p. 335-344.
- [22] Sufiiarov, V.S., E.V. Borisov, and I.A. Polozov. *Selective laser melting of the Inconel 718 nickel superalloy*. in *Applied Mechanics and Materials*. 2015. Trans Tech Publ.
- [23] Zhao, X., J. Chen, X. Lin, and W. Huang, *Study on microstructure and mechanical properties of laser rapid forming Inconel 718*. *Materials Science and Engineering: A*, 2008. **478**(1-2): p. 119-124.
- [24] Amato, K., S. Gaytan, L. Murr, E. Martinez, P. Shindo, J. Hernandez, S. Collins, and F. Medina, *Microstructures and mechanical behavior of Inconel 718 fabricated by selective laser melting*. *Acta Materialia*, 2012. **60**(5): p. 2229-2239.
- [25] Lu, Y., S. Wu, Y. Gan, T. Huang, C. Yang, L. Junjie, and J. Lin, *Study on the microstructure, mechanical property and residual stress of SLM Inconel-718 alloy manufactured by differing island scanning strategy*. *Optics & Laser Technology*, 2015. **75**: p. 197-206.
- [26] Rickenbacher, L., T. Etter, S. Hövel, and K. Wegener, *High temperature material properties of IN738LC processed by selective laser melting (SLM) technology*. *Rapid Prototyping Journal*, 2013. **19**(4): p. 282-290.

- [27] Scott - Emuakpor, O., J. Schwartz, T. George, C. Holycross, C. Cross, and J. Slater, *Bending fatigue life characterisation of direct metal laser sintering nickel alloy 718*. *Fatigue & Fracture of Engineering Materials & Structures*, 2015. **38**(9): p. 1105-1117.
- [28] Zhang, X., R. Tiwari, A.H. Shooshtari, and M.M. Ohadi, *An additively manufactured metallic manifold-microchannel heat exchanger for high temperature applications*. *Applied Thermal Engineering*, 2018. **143**: p. 899-908.
- [29] Kirsch, K.L. and K.A. Thole, *Experimental investigation of numerically optimized wavy microchannels created through additive manufacturing*. *Journal of Turbomachinery*, 2018. **140**(2): p. 021002.
- [30] Parbat, S.N., L. Yang, Z. Min, and M.K. Chyu, *Experimental and Numerical Analysis of Additively Manufactured Coupons With Parallel Channels and Inline Wall Jets*. *Journal of Turbomachinery*, 2019. **141**(6).
- [31] Yan, C., L. Hao, A. Hussein, P. Young, J. Huang, and W. Zhu, *Microstructure and mechanical properties of aluminium alloy cellular lattice structures manufactured by direct metal laser sintering*. *Materials Science and Engineering: A*, 2015. **628**: p. 238-246.
- [32] Crupi, V., E. Kara, G. Epasto, E. Guglielmino, and H. Aykul, *Static behavior of lattice structures produced via direct metal laser sintering technology*. *Materials & Design*, 2017. **135**: p. 246-256.
- [33] Parbat, S., Z. Min, L. Yang, and M. Chyu. *Experimental and Numerical Analysis of Additively Manufactured Inconel 718 Coupons With Lattice Structure*. in *Turbo Expo: Power for Land, Sea, and Air*. 2019. American Society of Mechanical Engineers.
- [34] Ghosh, S.K. and P. Saha, *Crack and wear behavior of SiC particulate reinforced aluminium based metal matrix composite fabricated by direct metal laser sintering process*. *Materials & Design*, 2011. **32**(1): p. 139-145.
- [35] Manfredi, D., F. Calignano, M. Krishnan, R. Canali, E.P. Ambrosio, S. Biamino, D. Ugues, M. Pavese, and P. Fino, *Additive manufacturing of Al alloys and aluminium matrix composites (AMCs)*, in *Light Metal Alloys Applications*. 2014, IntechOpen.
- [36] Van Bael, S., G. Kerckhofs, M. Moesen, G. Pyka, J. Schrooten, and J.-P. Kruth, *Micro-CT-based improvement of geometrical and mechanical controllability of selective laser melted Ti6Al4V porous structures*. *Materials Science and Engineering: A*, 2011. **528**(24): p. 7423-7431.
- [37] Kerckhofs, G., G. Pyka, M. Moesen, S. Van Bael, J. Schrooten, and M. Wevers, *High - resolution microfocus X - ray computed tomography for 3D surface roughness measurements of additive manufactured porous materials*. *Advanced Engineering Materials*, 2013. **15**(3): p. 153-158.

- [38] Kim, T.B., S. Yue, Z. Zhang, E. Jones, J.R. Jones, and P.D. Lee, *Additive manufactured porous titanium structures: Through-process quantification of pore and strut networks*. Journal of Materials Processing Technology, 2014. **214**(11): p. 2706-2715.
- [39] Karne, A., A. Kallonen, V.-P. Matilainen, H. Piili, and A. Salminen, *Possibilities of CT scanning as analysis method in laser additive manufacturing*. Physics Procedia, 2015. **78**: p. 347-356.
- [40] Snyder, J.C., C.K. Stimpson, K.A. Thole, and D.J. Mongillo, *Build direction effects on microchannel tolerance and surface roughness*. Journal of Mechanical Design, 2015. **137**(11): p. 111411.
- [41] Berger, R.T., *The X-or gamma-ray energy absorption or transfer coefficient: Tabulations and discussion*. Radiation Research, 1961. **15**(1): p. 1-29.
- [42] Kruth, J.P., M. Bartscher, S. Carmignato, R. Schmitt, L. De Chiffre, and A. Weckenmann, *Computed tomography for dimensional metrology*. CIRP annals, 2011. **60**(2): p. 821-842.
- [43] Deslattes, R.D., *Estimates of X-ray attenuation coefficients for the elements and their compounds*. Acta Crystallographica Section A: Crystal Physics, Diffraction, Theoretical and General Crystallography, 1969. **25**(1): p. 89-93.
- [44] Schmitt, R. and C. Niggemann, *Uncertainty in measurement for x-ray-computed tomography using calibrated work pieces*. Measurement Science and Technology, 2010. **21**(5): p. 054008.
- [45] Carmignato, S., V. Aloisi, F. Medeossi, F. Zanini, and E. Savio, *Influence of surface roughness on computed tomography dimensional measurements*. CIRP Annals, 2017. **66**(1): p. 499-502.
- [46] Pal, N.R. and S.K. Pal, *A review on image segmentation techniques*. Pattern recognition, 1993. **26**(9): p. 1277-1294.
- [47] Min, Z., S.N. Parbat, L. Yang, B. Kang, and M.K. Chyu, *Fabrication and Characterization of Additive Manufactured Nickel-Based Oxide Dispersion Strengthened Coating Layer for High-Temperature Application*. Journal of Engineering for Gas Turbines and Power, 2018. **140**(6).
- [48] Deshpande, S., A. Kulkarni, S. Sampath, and H. Herman, *Application of image analysis for characterization of porosity in thermal spray coatings and correlation with small angle neutron scattering*. Surface and coatings technology, 2004. **187**(1): p. 6-16.
- [49] Ghasemi - Mobarakeh, L., D. Semnani, and M. Morshed, *A novel method for porosity measurement of various surface layers of nanofibers mat using image analysis for tissue engineering applications*. Journal of applied polymer science, 2007. **106**(4): p. 2536-2542.

- [50] Desbois, G., J. Urai, and P. Kukla, *Morphology of the pore space in claystones—evidence from BIB/FIB ion beam sectioning and cryo-SEM observations*. eEarth Discussions, 2009. **4**(1): p. 1-19.
- [51] Patsis, G., V. Constantoudis, A. Tserepi, E. Gogolides, and G. Grozev, *Quantification of line-edge roughness of photoresists. I. A comparison between off-line and on-line analysis of top-down scanning electron microscopy images*. Journal of Vacuum Science & Technology B: Microelectronics and Nanometer Structures Processing, Measurement, and Phenomena, 2003. **21**(3): p. 1008-1018.
- [52] Verduin, T., P. Kruit, and C.W. Hagen, *Determination of line edge roughness in low-dose top-down scanning electron microscopy images*. Journal of Micro/Nanolithography, MEMS, and MOEMS, 2014. **13**(3): p. 033009.
- [53] Malpica, N., C.O. De Solórzano, J.J. Vaquero, A. Santos, I. Vallcorba, J.M. García - Sagredo, and F. Del Pozo, *Applying watershed algorithms to the segmentation of clustered nuclei*. Cytometry: The Journal of the International Society for Analytical Cytology, 1997. **28**(4): p. 289-297.
- [54] Vromen, J. and B. McCane. *Red blood cell segmentation from SEM images*. in *2009 24th International Conference Image and Vision Computing New Zealand*. 2009. IEEE.
- [55] Rannie, W., L.G. Dunn, and C.B. Millikan, *A simplified theory of porous wall cooling*. 1947, Pasadena, CA: Jet Propulsion Laboratory, National Aeronautics and Space
- [56] Eckert, E.R.G. and J.N. Livingood, *Comparison of effectiveness of convection-, transpiration-, and film-cooling methods with air as coolant*. Vol. 1182. 1954: National Advisory Committee for Aeronautics.
- [57] Moffat, R.J. and W.M. Kays, *The turbulent boundary layer on a porous plate: experimental heat transfer with uniform blowing and suction*. International Journal of Heat and Mass Transfer, 1968. **11**(10): p. 1547-1566.
- [58] Simpson, R.L., R. Moffat, and W. Kays, *The turbulent boundary layer on a porous plate: experimental skin friction with variable injection and suction*. International Journal of Heat and Mass Transfer, 1969. **12**(7): p. 771-789.
- [59] Laganelli, A. *A comparison between film cooling and transpiration cooling systems in high speed flow*. in *8th Aerospace Sciences Meeting*. 1970.
- [60] Le Brocq, P., B. Launder, and C. Priddin, *Experiments on transpiration cooling: First paper: Discrete hole injection as a means of transpiration cooling; an experimental study*. Proceedings of the Institution of Mechanical Engineers, 1973. **187**(1): p. 149-157.
- [61] Liu, Y.-Q., P.-X. Jiang, S.-S. Jin, and J.-G. Sun, *Transpiration cooling of a nose cone by various foreign gases*. International journal of heat and mass transfer, 2010. **53**(23-24): p. 5364-5372.

- [62] Langener, T., J. Von Wolfersdorf, and J. Steelant, *Experimental investigations on transpiration cooling for scramjet applications using different coolants*. AIAA journal, 2011. **49**(7): p. 1409-1419.
- [63] Huang, Z., Y.-h. Zhu, Y.-b. Xiong, and P.-x. Jiang, *Investigation of transpiration cooling for sintered metal porous struts in supersonic flow*. Applied thermal engineering, 2014. **70**(1): p. 240-249.
- [64] Zhao, L., J. Wang, J. Ma, J. Lin, J. Peng, D. Qu, and L. Chen, *An experimental investigation on transpiration cooling under supersonic condition using a nose cone model*. International journal of thermal sciences, 2014. **84**: p. 207-213.
- [65] Huang, G., Y. Zhu, Z. Liao, X.-L. Ouyang, and P.-X. Jiang, *Experimental investigation of transpiration cooling with phase change for sintered porous plates*. International Journal of Heat and Mass Transfer, 2017. **114**: p. 1201-1213.
- [66] Langener, T., J. von Wolfersdorf, T. Laux, and J. Steelant. *Experimental investigation of transpiration cooling with subsonic and supersonic flows at moderate temperature levels*. in *44th AIAA/ASME/SAE/ASEE Joint Propulsion Conference & Exhibit*. 2008.
- [67] Langener, T., J. Von Wolfersdorf, M. Selzer, and H. Hald, *Experimental investigations of transpiration cooling applied to C/C material*. International Journal of Thermal Sciences, 2012. **54**: p. 70-81.
- [68] Wang, J., L. Zhao, X. Wang, J. Ma, and J. Lin, *An experimental investigation on transpiration cooling of wedge shaped nose cone with liquid coolant*. International Journal of Heat and Mass Transfer, 2014. **75**: p. 442-449.
- [69] Jiang, P.-X., G. Huang, Y. Zhu, Z. Liao, and Z. Huang, *Experimental investigation of combined transpiration and film cooling for sintered metal porous struts*. International Journal of Heat and Mass Transfer, 2017. **108**: p. 232-243.
- [70] Wu, N., J. Wang, F. He, G. Dong, and L. Tang, *An experimental investigation on transpiration cooling of a nose cone model with a gradient porosity layout*. Experimental Thermal and Fluid Science, 2019. **106**: p. 194-201.
- [71] Ma, J., X. Luo, H. Li, and Y. Liu, *An experimental investigation on transpiration cooling based on the multilaminated sintered woven wire mesh structures*. Journal of Thermal Science and Engineering Applications, 2016. **8**(3).
- [72] Eriksen, V. and R. Goldstein, *Heat transfer and film cooling following injection through inclined circular tubes*. 1974.
- [73] Eriksen, V. and R. Goldstein, *Heat transfer and film cooling following normal injection through a round hole*. 1974.
- [74] Jabbari, M. and R. Goldstein, *Adiabatic wall temperature and heat transfer downstream of injection through two rows of holes*. 1978.

- [75] Goldstein, R., P. Jin, and R. Olson, *Film cooling effectiveness and mass/heat transfer coefficient downstream of one row of discrete holes*. 1999.
- [76] Goldstein, R. and P. Jin, *Film cooling downstream of a row of discrete holes with compound angle*. *J. Turbomach.*, 2001. **123**(2): p. 222-230.
- [77] Goldstein, R.J., E.R.G. Eckert, and J.W. Ramsey, *Film cooling with injection through holes: adiabatic wall temperatures downstream of a circular hole*. 1968.
- [78] Mick, W. and R. Mayle, *Stagnation film cooling and heat transfer, including its effect within the hole pattern*. 1988.
- [79] Takeishi, K., M. Matsuura, S. Aoki, and T. Sato, *An experimental study of heat transfer and film cooling on low aspect ratio turbine nozzles*. 1990.
- [80] Mehendale, A. and J. Han, *Influence of high mainstream turbulence on leading edge film cooling heat transfer*. 1992.
- [81] Ou, S., J.-C. Han, A.B. Mehendale, and C.P. Lee, *Unsteady wake over a linear turbine blade cascade with air and CO₂ film injection: Part I—Effect on heat transfer coefficients*. 1994.
- [82] Kelly, G.B. and D.G. Bogard. *An investigation of the heat transfer for full coverage film cooling*. in *Turbo Expo: Power for Land, Sea, and Air*. 2003.
- [83] Yang, C.-f. and J.-z. Zhang, *Experimental investigation on film cooling characteristics from a row of holes with ridge-shaped tabs*. *Experimental Thermal and Fluid Science*, 2012. **37**: p. 113-120.
- [84] Yang, W., X. Shi, and J. Zhang, *Experimental investigation on film cooling characteristics of ellipse-shaped tab*. *Experimental Thermal and Fluid Science*, 2017. **81**: p. 277-290.
- [85] Li, W., X. Lu, X. Li, J. Ren, and H. Jiang, *Wall thickness and injection direction effects on flat plate full-coverage film cooling arrays: Adiabatic film effectiveness and heat transfer coefficient*. *International Journal of Thermal Sciences*, 2019. **136**: p. 172-181.
- [86] Chyu, M. and Y. Hsing. *Use of a thermographic phosphor fluorescence imaging system for simultaneous measurement of film cooling effectiveness and heat transfer coefficient*. in *Turbo Expo: Power for Land, Sea, and Air*. 1996. American Society of Mechanical Engineers.
- [87] Yu, Y. and M. Chyu, *Influence of gap leakage downstream of the injection holes on film cooling performance*. 1998.
- [88] Yu, Y., C.-H. Yen, T.-P. Shih, M. Chyu, and S. Gogineni, *Film cooling effectiveness and heat transfer coefficient distributions around diffusion shaped holes*. *J. Heat Transfer*, 2002. **124**(5): p. 820-827.

- [89] Ekkad, S.V., S. Ou, and R.B. Rivir, *A transient infrared thermography method for simultaneous film cooling effectiveness and heat transfer coefficient measurements from a single test*. J. Turbomach., 2004. **126**(4): p. 597-603.
- [90] Ekkad, S.V., D. Zapata, and J.-C. Han, *Film effectiveness over a flat surface with air and CO₂ injection through compound angle holes using a transient liquid crystal image method*. 1997.
- [91] Chen, S.P., M.K. Chyu, and T.I.-P. Shih, *Effects of upstream ramp on the performance of film cooling*. International journal of thermal sciences, 2011. **50**(6): p. 1085-1094.
- [92] Ligrani, P., M. Goodro, M. Fox, and H.-K. Moon, *Full-coverage film cooling: film effectiveness and heat transfer coefficients for dense hole arrays at different hole angles, contraction ratios, and blowing ratios*. Journal of heat transfer, 2013. **135**(3).
- [93] Rogers, N., Z. Ren, W. Buzzard, B. Sweeney, N. Tinker, P. Ligrani, K. Hollingsworth, F. Liberatore, R. Patel, and S. Ho, *Effects of double wall cooling configuration and conditions on performance of full-coverage effusion cooling*. Journal of Turbomachinery, 2017. **139**(5).
- [94] Li, G.-c., P. Yang, W. Zhang, Z. Wu, and Z.-h. Kou, *Enhanced film cooling performance of a row of cylindrical holes embedded in the saw tooth slot*. International Journal of Heat and Mass Transfer, 2019. **132**: p. 1137-1151.
- [95] Hatch, J.E. and S.S. Papell, *Use of a theoretical flow model to correlate data for film cooling or heating an adiabatic wall by tangential injection of gases of different fluid properties*. 1959: National Aeronautics and Space Administration.
- [96] Hartnett, J., R.C. Birkebak, and E. Eckert, *Velocity distributions, temperature distributions, effectiveness and heat transfer for air injected through a tangential slot into a turbulent boundary layer*. 1961.
- [97] Sturgess, G., *Correlation of data and prediction of effectiveness from film cooling injection geometries of a practical nature*, in *Combustion and Heat Transfer in Gas Turbine Systems*. 1971, Elsevier. p. 229-249.
- [98] Pai, B. and J. Whitelaw, *The prediction of wall temperature in the presence of film cooling*. International Journal of Heat and Mass Transfer, 1971. **14**(3): p. 409-426.
- [99] Mukherjee, D., *Film cooling with injection through slots*. 1976.
- [100] Kruse, H., *Effects of hole geometry, wall curvature and pressure gradient on film cooling downstream of a single row*. htcg, 1985.
- [101] Baldauf, S.a., M. Scheurlen, A. Schulz, and S. Wittig. *Correlation of film cooling effectiveness from thermographic measurements at engine like conditions*. in *Turbo Expo: Power for Land, Sea, and Air*. 2002.

- [102] Muska, J., R. Fish, and M. Suo, *The additive nature of film cooling from rows of holes*. 1976.
- [103] Fuqua, M. and J. Rutledge, *Film cooling superposition theory for multiple rows of cooling holes with multiple coolant temperatures*, in *ASME Turbo Expo 2020: Turbomachinery Technical Conference and Exposition*. 2020: London, England.
- [104] Takeishi, K., Y. Oda, T. Nagao, and H. Sakamoto, *Superposition method for multi rows of a film cooling hole on a turbine stationary vane surface*. *WIT Transactions on Engineering Sciences*, 2016. **106**: p. 11-24.
- [105] Meng, T., H.-r. Zhu, C.-l. Liu, and J.-s. Wei, *Investigation on the accuracy of superposition predictions of film cooling effectiveness*. *International Journal of Turbo & Jet-Engines*, 2018. **35**(2): p. 181-192.
- [106] Rohsenow, W.M., J.P. Hartnett, and Y.I. Cho, *Handbook of heat transfer*. Vol. 3. 1998: McGraw-Hill New York.
- [107] Wang, J. and H. Wang, *A discussion of transpiration cooling problems through an analytical solution of local thermal nonequilibrium model*. 2006.
- [108] Hsu, C.-T. and P. Cheng, *Thermal dispersion in a porous medium*. *International Journal of Heat and Mass Transfer*, 1990. **33**(8): p. 1587-1597.
- [109] Jiang, P.-X., B.-X. Wang, D.-A. Luo, and Z.-P. Ren, *Fluid flow and convective heat transfer in a vertical porous annulus*. *Numerical Heat Transfer, Part A Applications*, 1996. **30**(3): p. 305-320.
- [110] Ichimiya, K., *A new method for evaluation of heat transfer between solid material and fluid in a porous medium*. 1999.
- [111] Nield, D., *A note on the modeling of local thermal non-equilibrium in a structured porous medium*. *International journal of heat and mass transfer*, 2002. **45**(21): p. 4367-4368.
- [112] Kuwahara, F., C. Yang, K. Ando, and A. Nakayama, *Exact solutions for a thermal nonequilibrium model of fluid saturated porous media based on an effective porosity*. *Journal of heat transfer*, 2011. **133**(11).
- [113] Wakao, N., *Particle-to-fluid transfer coefficients and fluid diffusivities at low flow rate in packed beds*. *Chemical Engineering Science*, 1976. **31**(12): p. 1115-1122.
- [114] Dixon, A.G. and D.L. Cresswell, *Theoretical prediction of effective heat transfer parameters in packed beds*. *AIChE Journal*, 1979. **25**(4): p. 663-676.
- [115] Achenbach, E., *Heat and flow characteristics of packed beds*. *Experimental thermal and fluid science*, 1995. **10**(1): p. 17-27.

- [116] Muralidhar, K. and K. Suzuki, *Analysis of flow and heat transfer in a regenerator mesh using a non-Darcy thermally non-equilibrium model*. International journal of heat and mass transfer, 2001. **44**(13): p. 2493-2504.
- [117] Pallares, J. and F. Grau, *A modification of a Nusselt number correlation for forced convection in porous media*. International communications in heat and mass transfer, 2010. **37**(9): p. 1187-1190.
- [118] Yang, L., Z. Min, T. Yue, Y. Rao, and M.K. Chyu, *High resolution cooling effectiveness reconstruction of transpiration cooling using convolution modeling method*. International Journal of Heat and Mass Transfer, 2019. **133**: p. 1134-1144.
- [119] Yang, L., Z. Min, S.N. Parbat, and M.K. Chyu. *Effect of Pore Blockage on Transpiration Cooling With Additive Manufacturable Perforate Holes*. in *ASME Turbo Expo 2018: Turbomachinery Technical Conference and Exposition*. 2018. American Society of Mechanical Engineers Digital Collection.
- [120] Min, Z., Y. Wu, K. Yang, J. Xu, S.N. Parbat, and M.K. Chyu, *Dimensional Characterizations Using Scanning Electron Microscope and Surface Improvement With Electrochemical Polishing of Additively Manufactured Microchannels*. Journal of Engineering for Gas Turbines and Power, 2021. **143**(4): p. 041020.
- [121] Liao, P.-S., T.-S. Chen, and P.-C. Chung, *A fast algorithm for multilevel thresholding*. J. Inf. Sci. Eng., 2001. **17**(5): p. 713-727.
- [122] Min, Z., Y. Wu, K. Yang, J. Xu, S.N. Parbat, and M.K. Chyu, *Dimensional Characterizations Using SEM and Surface Improvement with Electrochemical Polishing of Additively Manufactured Microchannels*, in *ASME Turbo Expo 2020: Turbomachinery Technical Conference and Exposition*. 2020: London, England.
- [123] Hilton, P., *Rapid tooling: technologies and industrial applications*. 2000: CRC press.
- [124] Pyka, G., G. Kerckhofs, I. Papantoniou, M. Speirs, J. Schrooten, and M. Wevers, *Surface roughness and morphology customization of additive manufactured open porous Ti6Al4V structures*. Materials, 2013. **6**(10): p. 4737-4757.
- [125] Huang, Q., *An analytical foundation for optimal compensation of three-dimensional shape deformation in additive manufacturing*. Journal of Manufacturing Science and Engineering, 2016. **138**(6).
- [126] Baicheng, Z., L. Xiaohua, B. Jiaming, G. Junfeng, W. Pan, S. Chen-nan, N. Muiling, Q. Guojun, and W. Jun, *Study of selective laser melting (SLM) Inconel 718 part surface improvement by electrochemical polishing*. Materials & Design, 2017. **116**: p. 531-537.
- [127] Pyka, G., A. Burakowski, G. Kerckhofs, M. Moesen, S. Van Bael, J. Schrooten, and M. Wevers, *Surface modification of Ti6Al4V open porous structures produced by additive manufacturing*. Advanced Engineering Materials, 2012. **14**(6): p. 363-370.

- [128] Min, Z., G. Huang, S.N. Parbat, L. Yang, and M.K. Chyu, *Experimental investigation on additively manufactured transpiration and film cooling structures*. Journal of Turbomachinery, 2019. **141**(3).
- [129] Min, Z., S.N. Parbat, L. Yang, and M.K. Chyu. *Thermal-Fluid and Mechanical Investigations of Additively Manufactured Geometries for Transpiration Cooling*. in *Turbo Expo: Power for Land, Sea, and Air*. 2019. American Society of Mechanical Engineers.
- [130] Saumweber, C. and A. Schulz, *Effect of geometry variations on the cooling performance of fan-shaped cooling holes*. Journal of Turbomachinery, 2012. **134**(6).
- [131] Kline, S.J., *Describing uncertainty in single sample experiments*. Mech. Engineering, 1953. **75**: p. 3-8.
- [132] Min, Z., G. Huang, S.N. Parbat, L. Yang, and M.K. Chyu. *Experimental Investigation on Additively Manufactured Transpiration and Film Cooling Structures*. in *ASME Turbo Expo 2018: Turbomachinery Technical Conference and Exposition*. 2018. American Society of Mechanical Engineers Digital Collection.
- [133] Hesselgreaves, J.E., R. Law, and D. Reay, *Compact heat exchangers: selection, design and operation*. 2016: Butterworth-Heinemann.
- [134] Min, Z., S.N. Parbat, Q. M. Wang, and M.K. Chyu, *Surface heater fabrication using micro-lithography for transpiration cooling heat transfer coefficient measurements*, in *Turbo Expo : Turbomachinery Technical Conference and Exposition*. 2021, ASME: Virtual, Online.
- [135] Watlow. *Flexible heaters from Watlow*. <https://www.watlow.com/products/heaters>.
- [136] Kim, I.-D., A. Rothschild, D.-J. Yang, and H.L. Tuller, *Macroporous TiO₂ thin film gas sensors obtained using colloidal templates*. Sensors and Actuators B: Chemical, 2008. **130**(1): p. 9-13.
- [137] Fine, G.F., L.M. Cavanagh, A. Afonja, and R. Binions, *Metal oxide semi-conductor gas sensors in environmental monitoring*. sensors, 2010. **10**(6): p. 5469-5502.
- [138] Lee, S.-G., H.-C. Park, S.D. Pandita, and Y. Yoo, *Performance improvement of IPMC (ionic polymer metal composites) for a flapping actuator*. International Journal of Control, Automation, and Systems, 2006. **4**(6): p. 748-755.
- [139] Min, Z., M. Gudarzi, and Q.-M. Wang. *Modeling, fabrication and analysis of a flexible PZT-polymer laminated composite cantilever beam in sensing and actuation modes*. in *2017 IEEE International Ultrasonics Symposium (IUS)*. 2017. IEEE.
- [140] Adachi, H., A. Takenouchi, T. Fukada, H. Uehara, and Y. Takemura, *Method of manufacturing a thin film transistor in which the gate insulator comprises two oxide films*. 1997, Google Patents.

- [141] Lim, S., S.-j. Kwon, H. Kim, and J.-S. Park, *High performance thin film transistor with low temperature atomic layer deposition nitrogen-doped ZnO*. Applied Physics Letters, 2007. **91**(18): p. 183517.
- [142] Sen, B., D.L. Schmidt, and D.G. Bogard, *Film cooling with compound angle holes: heat transfer*. 1996.
- [143] Albert, J.E., D.G. Bogard, and F. Cunha. *Adiabatic and overall effectiveness for a film cooled blade*. in *Turbo Expo: Power for Land, Sea, and Air*. 2004.
- [144] Mouzon, B.D., E.J. Terrell, J.E. Albert, and D.G. Bogard. *Net heat flux reduction and overall effectiveness for a turbine blade leading edge*. in *Turbo Expo: Power for Land, Sea, and Air*. 2005.
- [145] Brauckmann, D. and J. von Wolfersdorf. *Application of steady state and transient ir-thermography measurements to film cooling experiments for a row of shaped holes*. in *Turbo Expo: Power for Land, Sea, and Air*. 2005.
- [146] Facchini, B., L. Tarchi, L. Toni, and A. Ceccherini, *Adiabatic and overall effectiveness measurements of an effusion cooling array for turbine endwall application*. Journal of turbomachinery, 2010. **132**(4).
- [147] Mayle, R. and F. Camarata, *Multihole cooling film effectiveness and heat transfer*. 1975.
- [148] Sasaki, M., K. Takahara, T. Kumagai, and M. Hamano, *Film cooling effectiveness for injection from multirow holes*. 1979.
- [149] Harrington, M.K., M.A. McWaters, D.G. Bogard, C.A. Lemmon, and K.A. Thole, *Full-coverage film cooling with short normal injection holes*. J. Turbomach., 2001. **123**(4): p. 798-805.
- [150] Metzger, D., D. Takeuchi, and P. Kuenstler, *Effectiveness and heat transfer with full-coverage film cooling*. 1973.
- [151] Facchini, B., F. Maiuolo, L. Tarchi, and D. Coutandin. *Combined effect of slot injection, effusion array and dilution hole on the heat transfer coefficient of a real combustor liner: Part I—Experimental analysis*. in *Turbo Expo: Power for Land, Sea, and Air*. 2010.
- [152] Yang, L., W. Chen, and M.K. Chyu, *A convolution modeling method for pore plugging impact on transpiration cooling configurations perforated by straight holes*. International Journal of Heat and Mass Transfer, 2018. **126**: p. 1057-1066.
- [153] Sutskever, I., J. Martens, G. Dahl, and G. Hinton. *On the importance of initialization and momentum in deep learning*. in *International conference on machine learning*. 2013.